Stratospheric Black Carbon Injections and Climate Variability

by

Joshua Coupe

A dissertation submitted to the

School of Graduate Studies

Rutgers, The State University of New Jersey

In partial fulfillment of the requirements

For the degree of

Doctor of Philosophy

Graduate Program in Atmospheric Science

Written under the direction of

Alan Robock

And approved by

_____

_____

_____

_____

New Brunswick, New Jersey

October 2020

ABSTRACT OF THE DISSERTATION

Stratospheric Black Carbon Injections and Climate Variability

By JOSHUA COUPE

Dissertation Director:

Alan Robock

The climate impacts of smoke from fires ignited by nuclear war would include global cooling and crop failure. Previous efforts to model the climate impact of nuclear war have used a simplified representation of the aerosols that would be generated by massive fire storms. Here, I examine six nuclear war scenario simulations using an Earth system model that includes the growth of black carbon aerosols for the first time. I show that including aerosol growth processes reduces the residence time of soot aerosols, but the magnitude of global climate impacts are not reduced and a “nuclear winter” can be expected following a nuclear war scenario where 150 Tg of soot is injected into the upper troposphere and lower stratosphere. I show an El Niño-like response is robust across all nuclear war simulations for up to seven years. I employ sensitivity tests with the same climate model to understand the mechanisms behind the response, showing that the cooling of the Maritime Continent, cooling of tropical Africa, and the equatorward shift of the Intertropical Convergence Zone can all contribute to the El Niño-like state. Finally, I investigate the response of the Northern Hemisphere wintertime circulation to soot aerosol injection through variations to the stratospheric polar vortex and surface Arctic

Oscillation response. I conduct another sensitivity experiment to isolate the role of a tropospheric and stratospheric pathway for stratospheric polar vortex strengthening. I show that surface cooling can cause an acceleration of the Northern Hemisphere wintertime stratospheric polar vortex that is statistically significant compared to the non-perturbed climatology, but which is only a fraction of what occurs in a model simulation that includes aerosol heating. The dynamics responsible for influencing the modes of climate variability examined here are applicable for the response to volcanic eruptions, asteroid impact events, and geoengineering experiments involving stratospheric aerosols.

MY CONTRIBUTION TO THE WORK

This dissertation is based on the work of one published paper [Coupe et al., 2019], one paper under review [Coupe et al., 2020], and another unwritten future paper. All figures and tables in this dissertation are my own creation, except for Figure 3.9 and Figure 3.11. The original six nuclear war simulations were conducted by Charles Bardeen. All analysis is my own work but many others consulted me and offered suggestions about my conclusions. All sensitivity experiments in Chapter 3 and 4, where I imposed a cooling perturbation by changing the albedo in CESM-WACCM4 were designed and conducted by me. Charles Bardeen assisted me in getting the model running. Analysis of biogeochemical response to nuclear war was a product of a collaboration with an interdisciplinary team and thus was not directly conducted by me. This analysis is included to supplement changes to equatorial Pacific climate.

ACKNOWLEDGMENTS

I am grateful to so many people at Rutgers and elsewhere who have helped me get to this point. First off, I would like to thank Alan Robock for giving me the opportunity to start this work and for guiding me through it over these past three years. I am extremely grateful for being able to travel to at least two conferences every year to present our research. I look forward to more collaborations through the years.

I would like to thank Chuck Bardeen for showing me the in-and-outs of running a climate model. It took Chuck's willingness to help, many Skype calls, and often hours of talking through the intricacies of radiation code, but in the end it helped me to contribute towards two highly contested areas of research. I would also like to thank the entire team of researchers who have been working on the climate impacts of nuclear war over these last three years, especially my "Nuclear Nino" work collaborators: Samantha Stevenson, Cheryl Harrison, Nicole Lovenduski, and Tyler Rohr. Without their contributions and feedback this work would not have been possible.

Finally, I want to thank my committee. Brian Toon always provided excellent feedback on my manuscripts and my first paper benefited immensely from this. I would like to thank Lili Xia, a member of our research group at Rutgers since I attended my first meeting. She is always a source of insight and is always thinking of new questions to ask, which has always propelled my research further. I thank Ben Lintner, who, since I was an undergraduate Meteorology major, has taught me more

derivations than I can count from Atmospheric Thermodynamics to Geophysical Fluid Dynamics.

I also want to thank my family and friends for supporting me through the years. Finally, I thank my girlfriend Valerie, who has always been by my side as we simultaneously navigate the challenges of graduate school and medical school together.

This work was supported by a grant from the Open Philanthropy Project.

TABLE OF CONTENTS

CHAPTER 1: INTRODUCTION

This dissertation will answer three main scientific questions utilizing a state-of-the-art Earth system model.

1. What are the effects of model resolution and model representation of aerosol processes on climate change following nuclear war?

2. Why do El Niño events tend to follow aerosol-driven cooling periods?

3. Why does the Northern Hemisphere wintertime circulation tend towards a positive northern annular mode following the injection of aerosols into the stratosphere?

In Chapter 1, I provide a summary of the current state of the peer-reviewed literature surrounding these questions and provide motivation for addressing these questions through the lens of nuclear war simulations. In addition, I discuss volcanic eruptions as an analog and introduce the model used throughout this dissertation. Chapter 2 compares the climate impacts of a United States and Russia nuclear war in two different climate models. Chapter 3 introduces the concept of “Nuclear Niño” and uses model sensitivity tests to explore its mechanisms. Chapter 4 examines the impact of stratospheric soot aerosols on the Northern Hemisphere wintertime circulation, relating it to the impact of volcanic sulfate aerosols, and explores the mechanisms responsible.

1.1 A Review of Past Studies on Nuclear Winter

Since the proliferation of nuclear weapons in the 20th Century, considerable research has been conducted to understand the impact of a nuclear war on society and the environment. The theory of nuclear winter suggests that in the event of a nuclear war, large amounts of smoke from fires generated by nuclear blasts can enter the stratosphere,

cooling the Earth to the point where sub-freezing temperatures occur during the daytime in summer in the mid-latitudes. The idea originated from a paper by Lewis [1979] that suggested massive forest fires could be triggered by the detonation of nuclear weapons. Crutzen and Birks [1982] took this idea further, concluding that the massive amounts of smoke generated by the fires would linger in the troposphere and reduce sunlight. It was not until the TTAPS study [Turco et al. 1983] when it was realized that the absorption of solar radiation by smoke could cause lofting even higher into the stratosphere, potentially spreading the smoke throughout the world, reducing solar radiation at the surface and leading to large scale cooling.

Aleksandrov and Stenchikov [1983] conducted the first three-dimensional climate modeling for the injection scenarios of Turco et al. [1983] showing that continental temperature reductions would be large despite moderation by the oceans. Malone et al. [1985] conducted the first three-dimensional simulations including smoke transport as well as removal by precipitation, showing that solar heating could cause smoke in the troposphere to rise into the stratosphere before it could be removed by precipitation, greatly prolonging the lifetime of the smoke. The effect of this smoke entering Earth's upper atmosphere would be to block out sunlight for months to years leading to an inevitable decline in global mean surface temperatures. In 1986, The Scientific Committee on Problems of the Environment of the International Council of Scientific Unions published a report describing the immense biological, ecological, and human impacts of a nuclear war based on the literature at the time [Pittock et al., 1986]. The first simulation with a modern, comprehensive coupled atmosphere-ocean climate model by Robock et al. [2007a] showed that solar heating would loft smoke deep into the

stratosphere. Robock et al. [2007a] confirmed that a nuclear winter would result from the amount of soot that could be produced by a nuclear war between Russia and the United States with current arsenals [Toon et al., 2008]. Later agricultural modeling of a regional nuclear war showed an increased likelihood of crop failures and global famine due to the climate effects of smoke [Xia et al., 2013; Xia et al., 2015].

Updated calculations of the smoke that would be emitted from burning cities have confirmed previous estimates [Toon et al., 2008]. The result of sudden climate change has been affirmed by global coupled climate models with varying degrees of complexity, after assuming sufficient smoke reaches the upper troposphere [Robock et al., 2007a; Robock et al., 2007b; Mills et al., 2008; Mills et al., 2014; Pausata et al., 2016; Coupe et al., 2019]. Robock et al., [2007a] found that the injection of 150 Tg of black carbon into the 300 hPa to 150 hPa layer of the atmosphere over the United States and Russia would result in the reduction of global mean surface temperatures by more than 8 °C and precipitation by nearly 40% due to reduced evaporation and weakened monsoon circulations. Given the potentially immense impacts of a nuclear war on the climate, addressing uncertainties is important. One key uncertainty of nuclear winter is the evolution of the physical, chemical, and radiative properties of the smoke aerosols. Pausata et al. [2016] explored the effect of including aerosols with varying ratios of black and organic carbon, but the impact of aerosol coagulation was not simulated before Coupe et al. [2019].

1.2 Analogs for Nuclear Winter & Justification for Studying

A useful analog to nuclear winter is explosive volcanic eruptions, where sulfate aerosols released in volcanic plumes block sunlight and cool the Earth [Robock, 2000].

Research into the climate effects of volcanic eruptions has been extensive because observational data are available for comparison and ultimately validation. Additionally, the effects of past volcanic eruptions have led some to consider using stratospheric aerosols to mitigate anthropogenic global warming. Studies of observed volcanic eruptions and modeling experiments have found that surface cooling and heating in the stratosphere can also alter the atmospheric circulation in predictable ways. This can be through favoring certain atmospheric modes of variability, such as a positive Arctic Oscillation [Robock and Mao, 1992; Stenchikov et al., 2002; Zambri and Robock, 2016] or the warm phase of the El Niño-Southern Oscillation [Adams et al., 2003; Mann et al., 2005; Emile-Geay, 2007; Pausata et al., 2015; Stevenson et al., 2016]. Researching the climate impacts of volcanic eruptions is partly motivated by utilizing such information for the successful prediction of the ensuing global impacts of the next large volcanic eruption. The historical record suggests this is an inevitability. An increased interest in geoengineering experiments also motivates similar work on stratospheric aerosols in general. For similar reasons, the impact of stratospheric soot aerosols on atmospheric circulation should be studied [Kravitz et al., 2012]. The likelihood of nuclear war can be suggested to be less than that of a Pinatubo-sized volcanic eruption, based simply on the average return period for each event. However, an analog with an even greater aerosol loading of black carbon has likely occurred before according to geological records and modeling studies of such an event. The K-Pg asteroid extinction event, which took place nearly 66 million years ago, ejected thousands of Tg of smoke and dust into the atmosphere, prompting such dramatic climate change that extinction was widespread [Bardeen et al., 2017; Chiarenza et al., 2020]. Because the results of this massive black

carbon injection were so extreme, research into smaller black carbon injections, which humans can produce with existing nuclear arsenals, should not only occur but is necessary to fully characterize the threat to the climate.

1.3 Stratospheric Aerosols and the Arctic Oscillation

Following the three largest tropical volcanic eruptions of the latter half of the 20th century, a tendency for a warming pattern in the winter across large parts of the continental Northern Hemisphere was observed. A number of observational studies have reported on Eurasian warming after volcanic eruptions going back to 1850 [e.g., Groisman, 1992; Robock and Mao, 1992; Kodera, 1994; Kelly et al., 1996], while Shindell et al. [2004] has presented evidence of winter warming over Eurasia after volcanic eruptions going back to 1600. It has been suggested that this winter warming pattern after volcanic eruptions could be connected to the differential heating of sulfate aerosols in the stratosphere. The theoretical basis for the response was first demonstrated by Graf et al. [1993] using idealized numerical experiments. Several studies have linked the observed warming surface pattern to a stratospheric circulation change induced by a differential heating of stratospheric aerosols that cause an increase in the pole-to-equator temperature gradient [Graf et al., 1993; Kirchner et al., 1999; Stenchikov et al., 2002]. However, a more recent analysis of observed data and a large ensemble of a high-top climate model found the forced response from volcanic eruptions is far too weak to produce a robust winter warming signal that is statistically significant from the large natural variations inherent in the Northern Hemisphere wintertime circulation [Polvani et al., 2019]. This is still an active area of research and debate, partly because plausible mechanisms have been proposed but large natural variability obscures the signal of an

effect in many climate models. Two main mechanistic pathways have been proposed to explain the acceleration of the Northern Hemisphere stratospheric polar vortex (SPV) and tendency for winter warming after a volcanic eruption.

The first is the stratospheric pathway, first explored by Graf et al. [1993]. The stratospheric pathway mechanism was initially described as an acceleration of the Northern Hemisphere SPV during the winter due to the lack of aerosol heating over the pole compared to the mid-latitudes and tropics. To achieve thermal wind balance in response to the strong stratospheric temperature (and geopotential height) gradient, a westerly acceleration of the SPV occurs. During winter, a strong SPV will tend to propagate vertically towards the surface, eventually influencing the troposphere and favoring a positive mode of the Arctic Oscillation (AO). However, because the strongest stratospheric temperature gradient is in the subtropics during the winter, the need to achieve thermal wind balance produces a direct acceleration of the subtropical jet more so than the polar jet according to some work [Toohey et al., 2014; Bittner et al., 2016; DallaSanta et al., 2019]. To explain why the SPV is strengthened beyond what the temperature gradient implies, it has been proposed that the acceleration of the subtropical jet limits the poleward propagation of planetary waves by deflecting them towards the equator, allowing for the SPV to accelerate [Bittner et al., 2016b; DallaSanta et al., 2019]. Thus, the stratospheric pathway mechanism may require an acceleration of the stratospheric subtropical jet and the deflection of poleward propagating planetary waves to explain the enhancement of the polar vortex in model simulations of volcanic eruptions. The strengthening of the SPV is amplified by a feedback where a stronger SPV

reflects planetary waves, limiting disruptions of the vortex and allowing it to remain symmetric about the pole.

An additional tropospheric pathway has also been proposed to strengthen the SPV, which then influences the troposphere through coupling. Stenchikov et al. [2002], using the SKYHI model, found that the heating of aerosols was not necessary to force a positive Arctic Oscillation after the eruption of Mt. Pinatubo. The tropospheric pathway mechanism, similar but in the opposite direction of the proposed mechanism for producing a weaker jet stream with anthropogenic global warming, is caused by surface cooling in the subtropics, which results in a decrease in the mean meridional temperature gradient in the winter troposphere between 30°N and 60°N. The reduction in this temperature gradient reduces baroclinicity, and thus also reduces the amplitude of planetary waves in the troposphere as well as the vertical wave activity flux from the troposphere into the stratosphere [Stenchikov et al., 2002; Dallasanta et al., 2019]. This reduction in wave activity limits disruptions to the SPV and is associated with a strong, resilient SPV that is resistant to deceleration or breaking down.

The potential for enhanced predictability of the Northern Hemisphere winter climate continues to motivate similar research. Most recently, Polvani et al. [2019] examined the response to the Pinatubo eruption using three sets of model ensembles, finding no statistically significant winter warming associated with the strengthening of the SPV. Despite a positive Arctic Oscillation in the troposphere during the winter of 1991-1992, there was warming observed in the polar stratosphere and the strength of the SPV was actually diminished, rendering the stratospheric pathway mechanism unable to explain the tropospheric circulation pattern and subsequent temperature pattern in Europe

following this eruption. Polvani et al. [2019], using ensembles of WACCM4, a high-top model with a well-resolved stratosphere, showed that any effect from the heating of aerosols in the stratosphere would have been so insignificantly small that it could have only contributed to an acceleration of the Northern Hemisphere SPV by 3-4 m/s at best, consistent with Bittner et al. [2016b]. For this amount of acceleration in the SPV, Bittner [2015] found no statistically significant wintertime warming over northern Europe using 100 model ensemble members. Additionally, the potential for the tropospheric pathway mechanism to explain the positive AO after the Pinatubo eruption is contradicted by the observed increase in planetary wave activity during that winter [Graf et al., 2007]. While earlier work argued that winter warming following many volcanic eruptions in the historical record is not a coincidence, the internal variability of the Northern Hemisphere winter circulation and associated temperature patterns are greater than the forced signal from Pinatubo alone in many climate models.

It is difficult to confirm a cause and effect relationship for smaller aerosol loadings, but nuclear war simulations amplify the forced signal and provide clarity for the mechanisms at play. The changes to the stratosphere are amplified such that heating of the surrounding air by the aerosols reaches nearly 100°C due to the absorptive nature of black carbon, as much as 50 times the amount of heating after Pinatubo, which was 2 K according to reanalysis [Polvani et al., 2019]. Nuclear war simulations are an extreme case compared to tropical volcanic eruptions of the past century and provide an excellent opportunity to amplify stratospheric heating and surface cooling and enhance the forcing with fewer ensembles required.

1.4 Stratospheric Aerosols and the El Niño-Southern Oscillation

Unlike the Arctic Oscillation, historical changes in the El Niño-Southern Oscillation (ENSO) can be ascertained through more accurate proxy temperature records from the sea floor of the equatorial Pacific. Ice core records allow an approximation of the dates of large volcanic eruptions from the past thousand years based on deposits of sulfur and other components contained in the ash that travels across the globe [Robock and Free, 1995]. Combining these two proxy records has allowed research on the linkage between volcanic eruptions and ENSO to flourish, taking off after Adams et al. [2003] used proxy data to show the probability of an El Niño event after a volcanic eruption was double compared to years without an eruption. Emile-Geay [2007], using 200 ensembles of the Zebiak and Cane [1987] model found a 50% increase in the likelihood of an El Niño event following a large uniform negative radiative forcing across the Pacific, consistent with a large volcanic eruption like Pinatubo or larger. Observational evidence and modeling studies have often arrived at contradictory conclusions when it comes to the linkage between ENSO and volcanic eruptions.

Recently, several modeling studies have found an increase in the probability of El Niño events following volcanic eruptions and have proposed specific mechanisms [e.g., Maher et al., 2015; Stevenson et al., 2016; Predybaylo et al., 2017; Stevenson et al., 2016; Khodri et al., 2017]. Proposed mechanisms include the 1) the ocean dynamical thermostat mechanism [Zebiak and Cane, 1987; Clement et al., 1996; Emile-Geay et al., 2007], 2) the southward shift of the Intertropical Convergence Zone (ITCZ) [Donohoe et al., 2012; Pausata et al., 2015; Stevenson et al, 2016] 3) eastward propagating tropical Kelvin waves due to African land cooling and subsequent collapse of the West African Monsoon [Khodri et al., 2017], and 4) changes in the Asian monsoon and North Pacific

circulations [Sun et al., 2019]. No consensus exists on the relative contribution of proposed mechanisms towards the El Niño-like response; however, most mechanisms suggest externally forced westerly wind anomalies trigger the initial response. The initial westerly wind anomaly acts as the primary forcing of the ocean into an El Niño state, kickstarting the Bjerknes feedback [Bjerknes, 1969]. The zonal sea surface temperature (SST) gradient decreases while the west to east sea surface height (SSH) gradients decrease and relatively warm water is pushed eastward via a downwelling Kelvin wave excited by the weakened trade winds. Tropical convection shifts eastward, promoting the further development of westerly wind anomalies through a weakening of the Walker Circulation [Bjerknes, 1969].

The relationship between geoengineering strategies and El Niño has also been explored, although less extensively, to understand how using stratospheric aerosols to counteract global warming could affect the frequency and/or amplitude of the El Niño-Southern Oscillation. Little effect was ultimately found with geoengineering using CMIP5 models [Gabriel et al., 2015]. The relationship between ENSO and nuclear war, however, has not been explored beyond a brief mention of El Niño-like tendencies in a nuclear war simulation [Pausata et al., 2016]. The fact that only two nuclear weapons have ever been used during wartime combined with the low probability of a massive nuclear exchange are the most likely reasons for the limited interest. However, nuclear war simulations, with aerosols that are far more effective at intercepting radiation than volcanic sulfate aerosols, still can provide insight about the same mechanisms responsible for the linkage between volcanic eruptions and ENSO. By amplifying the forcing imposed on the climate system, it becomes more apparent which perturbations lead to the

development of an El Niño, because those forced changes rise above the noise of natural climate variability. By analyzing nuclear war scenarios conducted using CESM-WACCM4 I can further understand how and through what mechanisms ENSO responds to aerosol-driven cooling.

1.5 Summary of Work of the Dissertation

I use a state-of-the-art Earth system model to explore the multi-faceted response of the climate system to nuclear war. The model configuration used to study the climate impact of nuclear war throughout this dissertation is the Community Earth System Model (CESM) using the Whole Atmosphere Community Climate Model version 4 (WACCM4) as the atmospheric component. The model has a horizontal resolution of 1.9°×2.5° (lat-lon) with 66 vertical layers and a model top of 140 km [Marsh et al., 2013; Bardeen et al., 2017]. The Community Land Model 4.0 is used as the land surface model, Parallel Ocean Program v2 is the ocean model, tropospheric aerosols (other than black carbon) are prescribed, and ocean biogeochemistry is included. The transport and removal of soot from fires is handled by the Community Aerosol and Radiation Model for Atmospheres (CARMA). CARMA is a sectional aerosol model, which in this case treats soot as fractal particles [Toon et al., 1988; Turco et al., 1979; Bardeen et al., 2008, 2017]. This module allows for black carbon aerosols to coagulate together causing a change in size, which alters their radiative properties while affecting their residence time in the stratosphere. The model has a high atmospheric top to ensure that the stratospheric circulation, which becomes highly perturbed as the aerosols are heated, is well-resolved. This is important for analyzing the impact of the aerosols on the Northern Hemisphere wintertime circulation, where tropospheric weather patterns can be driven by stratospheric processes

that propagate towards the surface. Additionally, the use of CARMA helps constrain black carbon aerosols' lifetime in the stratosphere, a major uncertainty in nuclear winter simulations that has enormous consequences for the climate impact. CESM-WACCM4 can represent the frequency and periodicity of the El Niño-Southern Oscillation [Marsh et al. 2013] and has sufficiently simulated the response to volcanic eruptions of the last millennium [Bellenger et al., 2014]. This makes this coupled earth system model ideal for exploring the effect of black carbon aerosols on the Arctic Oscillation and the El Niño-Southern Oscillation.

In Chapter 2, the results of Coupe et al. [2019] are presented, where I examine the results of a climate model simulation of the 150 Tg United States and Russia nuclear war scenario in CESM-WACCM4 and compare it to the same scenario conducted in GISS ModelE [Robock et al., 2007]. I examine five climate model simulations of nuclear war scenarios between India and Pakistan to understand how sensitive the global climate response and aerosol residence time is to the initial aerosol mass. Model simulations examined in Chapter 2 were conducted by Charles Bardeen.

In Chapter 3, the results of Coupe et al. [2020] are presented. Here, I introduce "Nuclear Niño," a feature present in all the climate model simulations run in CESM-WACCM4 that are introduced in Chapter 2. I examine changes in temperature, precipitation, and equatorial Pacific wind stress. In this chapter, I conduct additional model sensitivity tests using CESM-WACCM4 to isolate the mechanisms responsible for the Nuclear Niño response by cooling different areas.

In Chapter 4, I examine changes to Northern Hemisphere wintertime atmospheric circulation via the Arctic Oscillation and the strength of the stratospheric polar vortex in

response to the six nuclear war simulations from Chapter 2. I assess the impact of aerosol heating on the stratospheric pole-to-equator temperature gradient in the stratosphere and quantify changes in vertically and poleward propagating waves to understand the impact of the spatial reorganization and reduction in tropical convection on the Northern Hemisphere wintertime atmospheric circulation. To help elucidate the contribution of two potential pathways for the response, I conduct a sensitivity test in CESM-WACCM4 where I eliminate stratospheric heating but allow surface cooling equivalent to the 150 Tg United States and Russia nuclear war scenario simulation.

CHAPTER 2: COMPARISON OF CESM-WACCM4 AND OLDER NUCLEAR WAR SIMULATIONS

2.1 Modeling the 150 Tg United States and Russia Nuclear War Scenario

Robock et al. [2007a] injected 150 Tg of black carbon aerosols into the GISS ModelE climate model to simulate an all-out nuclear war between the United States and Russia and concluded that nuclear winter would occur. The scenario assumed that between 3000 and 4000 nuclear weapons would strike primarily industrial areas and military installations and that 150 Tg of black carbon would be generated from mass fires following the explosions. Here, I report on a simulation of this scenario with CESM-WACCM4, a state-of-the-art coupled climate model using a more advanced aerosol scheme and a higher model top. Nuclear war is simulated as a one-week long injection of black carbon aerosols into a layer of the atmosphere between 300 hPa and 150 hPa over the United States and Russia starting on 15 May, to be consistent with the methods of Robock et al. [2007a].

GISS ModelE was a 4 degree by 5 degree (latitude by longitude) coupled climate model that treated soot as spherical black carbon aerosols at a fixed effective radius of 0.1 μm [Schmidt et al. 2006]. The model top was 80 km and there were 23 vertical layers, allowing for an adequately resolved stratosphere for its era. The results, in terms of human survival, were horrific as global mean surface temperatures dropped by nearly 8°C within a few years. However, the fixed size of the aerosols may have contributed to a longer than reasonable aerosol lifetime. A key uncertainty in the current understanding of nuclear winter is the lifetime and radiative properties of the aerosols. To assess this uncertainty, I use simulations of CESM-WACCM4 with CARMA that represent the

aerosols as fractals which can change size. This will help to quantify the impact of fractal aerosol growth on the climate impacts of a global nuclear war. A more realistic representation of the black carbon aerosols will alter surface radiation, affecting temperature, precipitation, and circulation patterns. The differences between CESM-WACCM4 and GISS ModelE are assessed to understand what variables are sensitive to different model configurations.

Since the simulations by Robock et al. [2007a] were published, the smoke calculations have since been refined (see Toon et al. [2007]) to confirm that up to 180 Tg of black carbon would be injected into the upper troposphere and lower stratosphere in a nuclear war between the United States and Russia. Following Robock et al. [2007a], this is rounded down, increasing the assumed initial removal of aerosols due to precipitation by 20%. The timing, geographical location, and altitude of the soot injection here are identical to Robock et al. [2007a], but the black carbon aerosol properties differ, as depicted by Figure 2.1, which shows the mass extinction coefficient (m^2/g) for near-visible wavelengths and for all black carbon particle sizes in CESM-WACCM4. For particles in CESM-WACCM4 with an effective radius of 0.1 μm, comparable to the fixed-sized particles in GISS ModelE, absorption is almost 20% larger because Robock et al. [2007a] artificially lowered the total extinction of their aerosols to 5.5 m^2/g to account for dust and organic carbon. However, following most nuclear war climate simulations that have been conducted to date, pure black carbon is used in CESM-WACCM4 under the assumption that neither dust nor organic carbon would reduce the soot's ability to absorb radiation [Bond and Bergstrom, 2006; Toon et al., 2007]. Organic carbon may lead to enhanced absorption of solar radiation but reduced lifetime due to larger particle

sizes, while Toon et al. [2007]'s smoke emission estimates assumed that organics would be oxidized rapidly in the stratosphere. Research into the organic contribution of soot aerosols generated by nuclear war has been limited (e.g., Pausata et al., 2016) and more research is necessary to further constrain the lifetime of aerosols with different compositions. This is beyond the scope of my dissertation.

2.1.1 Changes in Temperature

Replicating the 150 Tg black carbon injection over the United States and Russia using CESM-WACCM4 with CARMA results in a very similar evolution of global mean surface temperature anomalies as in GISS ModelE for about a year, before CESM-WACCM4 tends towards a colder long term mean state (Figure 2.2a). Surface shortwave radiation anomalies are greater in CESM-WACCM4 for the first eight years post-injection due to rapid fractal aerosol growth and the use of pure black carbon (Figure 2.2b). Despite this, CESM-WACCM4 global mean surface temperature anomalies are warmer than GISS ModelE during the first boreal summer after the injection, indicating that the newer, higher-resolution model is less sensitive to a large negative radiative forcing. One-year post-injection, CESM-WACCM4's temperature departure from the climatological mean is greater in magnitude than GISS ModelE. This remains the case until six years post-injection. Contradictorily, surface radiation anomalies are more negative in the CESM-WACCM4 simulation for more than eight years post-injection compared to GISS ModelE. This implies that compared to GISS ModelE, CESM-WACCM4 is both more sensitive to an increase in insolation in a relatively cold state and less sensitive to a decrease in insolation in a relatively warm state. Peak surface

temperature anomalies occur in years 2-3, with a maximum monthly mean temperature departure of 9.8°C in CESM-WACCM4 and 8.7°C in GISS ModelE.

Surface shortwave radiation returns to near normal levels in CESM-WACCM4 10 years post-injection when 99% of the aerosols have fallen out. After 10 years, CESM-WACCM4 global mean surface temperatures recover more quickly and are 2°C warmer than GISS ModelE (which was not run out any further). Temperatures in the CESM-WACCM4 simulation appear to find a new steady-state near 1°C below the control mean one decade post-injection. This can be explained by the expansion of land and sea ice, which reflects additional sunlight, and the slow rebound of ocean temperatures. The oceans take significantly longer to respond to a large forcing and act as a heat sink, preventing the climate state from returning to its pre-injection state. A similar result was found by Mills et al. [2014] in a 5 Tg India-Pakistan nuclear war simulation. It can be presumed that GISS ModelE would have simulated a similar long-term state, considering its slow recovery in temperatures at the 10-year mark. Coincidentally, a 1°C decrease in global mean surface temperatures alleviates much of the observed surface warming since pre-industrial times. Needless to say, nuclear war is not an adequate solution to resolve the crisis of climate change [Robock, 2015].

Temperature changes are not homogeneous in space. The magnitude of cooling across continental areas is extreme; below freezing temperatures encompass large areas of the Northern Hemisphere during the first June-July-August (JJA) post-injection in both models (see Figure 2.3). Extreme similarities are observed between both models, which largely agree on the spatial pattern and magnitude of cooling over largely populated areas of North America, Europe, and Asia for the first two years. The 0°C isotherm averaged

over the second JJA post-injection crosses Eastern Europe and agriculturally productive areas of the midwestern United States, although in GISS ModelE it is further east across Europe. Vast areas experience a “nuclear winter” in both models, where summer temperatures are below freezing. CESM-WACCM4 exhibits a longer duration of the most extreme temperatures, although its global mean temperatures do recover more quickly. Ultimately, in both simulations, the rate of change of global mean surface temperatures is beyond what modern human civilization has encountered to date.

To help contextualize the severity of these conditions for agriculture, I calculate the growing season length (GSL, number of consecutive days with minimum nighttime temperatures above 0°C) globally for CESM-WACCM4 (Figure 2.4) and highlight the daily temperature evolution for two locations in the first year post-injection (Figure 2.5). The GSL is calculated from January of Year 1 to December of Year 1 in the Northern Hemisphere and from July of Year 1 to June of Year 2 in the Southern Hemisphere (SH). Figure 2.4 shows large areas of the interior United States with a GSL below 50 days and most areas below 100 days. Eastern Europe’s GSL is reduced below 50 days and all parts of Russia have a GSL below 25 days. Hard freezes, where temperatures drop below −4°C, occur through Years 2 and 3 in the summer, making it nearly impossible to grow crops in the United States and Russia. Ukraine, Poland, and Germany suffer similar fates, while in China, only the southeast part of the country remains above freezing during the summer. Initially, the growing season across the Southern Hemisphere is not significantly impacted, but begins to experience greater reductions in GSL by Year 3. While CESM-WACCM4 produces slightly colder temperatures compared to GISS ModelE, surface temperatures in both simulations would be perilous for agriculture.

Robock et al. [2007a] examined the impacts of a nuclear winter at a more local level through an analysis of minimum temperatures in Iowa (42°N, 95°W) and Ukraine (50°N, 30°E) using GISS ModelE, showing that a 150 Tg soot injection would produce below freezing temperatures in Iowa consistently throughout the two years post-injection, except for a few days barely above freezing in midsummer. In Ukraine, GISS ModelE found below freezing temperatures for two full years, with temperatures barely above freezing in the summer of the second year. The same analysis is performed here and is shown in Figure 2.5 for WACCM4. Temperatures drop below freezing in Iowa one-week post-injection, which is in late May. Daily minimum temperatures rise above freezing only once in a span of 730 days. Minimum temperatures only consistently rise above freezing during the third summer after the initial injection of soot. In Ukraine, the first summer after the war is not as cold as Iowa, but minimum daily temperatures frequently drop below freezing. During the next summer, Ukraine minimum daily temperatures remain close to freezing but consecutive days with below freezing temperatures continues to occur. This behavior continues through the third summer after the war, when minimum daily temperatures rise to the 5°C range in both Ukraine and Iowa. Consistent freezes during summer are not conducive to a productive growing season, demonstrating that a nuclear war producing 150 Tg of black carbon would threaten food security in the United States, Russia, and across the globe. An analysis of the climate impacts of a smaller regional nuclear war found likely reductions to Chinese maize and rice production by 15% for 5 years in an agriculture model [Xia et al., 2015]. Climate change in the simulations here would surpass this.

The oceans respond more slowly to reduced sunlight and some differences in oceanic temperature patterns likely reflect shifts in ocean circulation. The major differences in spatial temperature patterns between both models include El Niño-like warming and warmer coastal Antarctic SSTs in CESM-WACCM4. Warming in the Southern Ocean has been discussed as a potential unintended consequence of stratospheric aerosol geoengineering experiments [McCusker et al., 2015] and our simulations exhibit this same tendency. The North Atlantic is also warmer in CESM-WACCM4 during both December-January-February (DJF) and JJA, which is likely related to an aggressive acceleration of the Atlantic Meridional Overturning Circulation. Winter warming is observed over the Arctic Ocean, but also along the Arctic coast of Eurasia for the first two winters after the injection due to changes in the Northern Hemisphere wintertime atmospheric circulation. While trivial to human impacts, Chapter 3 examines the mechanisms responsible for this response, which has implications for a similar response observed after volcanic eruptions. Remarkably, the two simulations, conducted 10 years apart with climate models with quite different resolutions and different treatment of aerosols, yield very similar results: nuclear winter and significant hardship for humanity in the aftermath of a large-scale nuclear war between the United States and Russia.

2.1.2 Changes in Precipitation Patterns

A reduction in global mean precipitation occurs post-injection in both models in response to reduced surface heating, which reduces evaporation and convection globally. Figure 2.2 shows a 40% or greater reduction in global precipitation rate anomaly (mm/day) for both CESM-WACCM4 and GISS ModelE. The precipitation response in

both simulations is more closely related to changes in surface shortwave radiation compared to changes in temperature. Thus, recovery in precipitation rate globally occurs more quickly in both simulations, but remains below control conditions in the long-term, just as with temperature. The reduction in global convective activity disrupts the Walker and Hadley Circulations, weakening both the ascending and descending branches of each circulation cell. Precipitation is severely weakened along the ITCZ, which shifts equatorward in response to the faster cooling of the Northern Hemisphere [Broccoli et al., 2006; Donohoe et al., 2012]. The weakened descending branch of the Hadley cell in the subtropics allows for an increase in precipitation in some subtropical deserts like the Sahara in both models from an easing of subsidence (see Figure 2.6).

An increase in precipitation along the western United States is observed in both model simulations, another indication of the weakened descending Hadley cell in the subtropics. This could also be interpreted as evidence of a teleconnection from the El Niño-like increase in equatorial Pacific precipitation. CESM-WACCM4 simulates an unprecedented El Niño event in response to soot injections, which is analyzed in Chapter 3. The Asian summer monsoon is compromised in both models mostly due to the reduced temperature contrast between the continents and ocean, consistent with the simulated impact of volcanic eruptions over the last millennium [Zambri and Robock, 2016; Zambri et al., 2017]. The strong reduction in precipitation over southeast Asia during the second JJA post-injection in both models is evidence that the collapse of the Asian summer monsoon is not dependent on the development of an El Niño, as GISS ModelE struggles to develop one, because it lacks sufficient horizontal resolution. The Asian summer monsoon remains severely diminished for six monsoon seasons in CESM-

WACCM4. Generally, outside of monsoon regions, reduced precipitation is explained by the reduction in evaporation. Locally, other factors may enhance or weaken the response.

2.1.3 Aerosol Lifetime

After initial injection, black carbon aerosols loft as high as 0.01 hPa in CESM-WACCM4 (Figure 2.7a), grow rapidly (Figure 2.7b), and cause anomalous stratospheric heating of more than 100°C (Figure 2.7c,d). All these factors, in conjunction with natural removal processes such as gravitational settling and scavenging by precipitation, dictate the lifetime of black carbon aerosols. The residence time of aerosols in the troposphere is on the order of days to weeks because of precipitation, but the stratosphere acts as a refuge, and black carbon aerosols can rise deep into the stratosphere from self-lofting, enhancing their lifetime over volcanic sulfate aerosols.

An e-folding lifetime of 4.6 years was reported by Robock et al. [2007a] for their 150 Tg injection of black carbon aerosols with an effective radius of 0.1 μm. The e-m. The e-folding lifetime in CESM-WACCM4 is only 3.5 years as a result of fractal aerosol growth, which after a few years, quickens the pace of removal compared to GISS ModelE. For a smaller 5 Tg black carbon injection over India and Pakistan with fixed aerosol sizes, Mills et al. [2014] found an e-folding lifetime of 8.4 years using CESM-WACCM4 without CARMA, while Robock et al. [2007b] found it to be 6 years using GISS ModelE. The discrepancy is evidence of enhanced aerosol lifetime due to the higher vertical resolution and model top in CESM-WACCM4, which allows soot to rise even further. Additionally, the slowing of the stratospheric residual circulation can play a role in extending the lifetime of black carbon aerosols [Mills et al., 2008]. In CESM-

WACCM4 with CARMA, aerosol coagulation is expected to reduce the lifetime of the aerosols compared to Mills et al. [2014].

The evolution of the global mass of black carbon aerosols in the atmosphere, the effective radius of the aerosols, and the optical depth per unit mass of black carbon are shown for the CESM-WACCM4 simulation in Figure 2.8. Total aerosol mass was available for GISS ModelE, but the components required to calculate Figure 2.8c were not saved. The slow removal of black carbon aerosols during the first year for both simulations is apparent from Figure 2.8a. Despite the rapid growth of aerosols to an effective radius near 1 μm. The e-m in CESM-WACCM4 within the first six months (Figure 2.8b), total aerosol mass is similar between the two model simulations. The effectiveness of the aerosols' ability to absorb radiation and cause self-lofting into the upper stratosphere is significant enough to overcome its larger size. A metric for aerosol efficiency in terms of its ability to intercept shortwave radiation is quantified as the optical depth per unit mass of black carbon averaged globally, as shown for CESM-WACCM4 in Figure 2.8c. Aerosol efficiency varies through time, increasing as aerosols spread out initially but decreasing steadily as coagulation occurs. The efficiency plateaus over the first six years, then slowly rises as very few aerosols are left in the atmosphere. Aerosol growth contributes to shorter aerosol lifetime compared to GISS ModelE, but the climate impacts are not significantly different. Despite including a process that increases the rate of aerosol removal, new simulations of the 150 Tg United States and Russia nuclear war scenario confirm the prospects of a harsh nuclear winter.

2.2 Simulations of India and Pakistan Nuclear War Scenarios

While I focus on the 150 Tg United States and Russia nuclear war scenario simulation in this dissertation to explore the mechanisms behind persistent modes of climate variability, five additional India and Pakistan nuclear war scenarios are also used to explore the scaling of the response as a function of radiative forcing. I briefly present an analysis of the global impact of these five scenarios in climate model simulations, which are also discussed in Toon et al. [2019]. Table 2.1 shows the aerosol loading, countries, number of weapons, and average yield for each simulation.

Global mean surface temperatures drop precipitously across the spectrum of black carbon injections over India and Pakistan simulated here (Figure 2.9). Although the impacts are dwarfed by the 150 Tg United States and Russia simulation, even 5 Tg of soot causes a 1°C reduction in global mean surface temperatures within two years. This perturbation exceeds the impact of most modern volcanic eruptions in terms of peak temperature response and length of the response. In the largest 46.8 Tg case, the peak temperature anomaly is 6°C below the mean within 3 years of the injection. Precipitation reductions scale similarly with temperature changes and indicate the collapse of monsoonal circulations across the globe, but not for the same duration or at the same magnitude as in the 150 Tg case.

Soot aerosol removal is significantly slower in the India and Pakistan simulations for the first four years, as indicated by the time evolution of the fraction of initial aerosol mass in all nuclear war simulations shown in Figure 2.10. During the first winter after the 150 Tg soot injection, nearly 20% of the initial soot is removed and by one year post-injection, 35% of the initial soot has been removed. In all the India and Pakistan cases, 90% of the soot remains at this same point in time. This indicates the latitude of initial

injection can increase soot residence time for injections that take place during the same time of the year. An injection over a region closer to the equator will experience greater initial self-lofting due to the higher sun angle, consistent with Mills et al. [2014]. The stratospheric overturning circulation allows for soot to spread more quickly throughout the globe at lower latitudes of injection.

Although self-lofting and global aerosol spread occurs in the 150 Tg soot injection case, a larger proportion of the aerosol cloud mass is at lower altitudes and higher latitudes compared to the India and Pakistan cases in the first few years. However, aerosol removal does begin to slow down in the 150 Tg case around year 5-6, while removal begins to accelerate in the India and Pakistan cases. This time period coincides with an increase in surface temperatures and precipitation that may be favorable for enhanced rain-out of aerosols in the upper troposphere. In the 5 Tg case, enhanced removal of aerosols occurs because the aerosol concentration is far less, reducing the amount of aerosol heating and lofting 3-4 years post-injection. The e-folding time of five years in the 5 Tg simulation here is smaller than what was reported in Robock et al. [2007b] and Mills et al. [2014], 6 years and 8.4 years, respectively.

CHAPTER 3: NUCLEAR NIÑO: IMPACT AND MECHANISMS

To survive in the aftermath of a nuclear war, the nearly 7 billion people who do not perish directly from the explosions or firestorms would have to contend with severely diminished growing seasons and agricultural output [Coupe et al., 2019; Xia et al., 2015], and would likely turn to the oceans as an additional source of food. Protein from fisheries and marine aquaculture provides 17% of the world's annually consumed animal protein, with far higher proportions locally [FAO, 2018]. Evaluating the ocean response to nuclear war is thus crucial to assessing potential perturbations to overall food security.

The El Niño-Southern Oscillation (ENSO) is the largest naturally occurring perturbation to Pacific Ocean circulation and biogeochemistry, alternating between warm El Niño and cold La Niña events with a period of roughly 3 to 7 years [Trenberth, 1997], with profound impacts on marine productivity [Chavez et al., 2011; Lehodey et al., 2006]. ENSO is known to be sensitive to both natural and anthropogenic climate influences, providing a pathway to understand the physical and biological impacts of aerosol-driven cooling on the ocean; yet the response of ENSO to aerosol cooling from nuclear war has not been studied beyond a brief mention of El Niño-like tendencies in nuclear war simulations [e.g., Pausata et al., 2016]. The climatic perturbation induced by a nuclear war is like the effects of a very large tropical volcanic eruption, but it is longer lasting due to the stronger self-lofting properties of the soot released into the atmosphere [Yu et al., 2019]. Paleoclimate data [Adams et al., 2003; Li et al., 2013; McGregor et al., 2010] and modeling experiments [Mann et al., 2005; Emile-Geay et al., 2008; Ohba et al., 2013; Maher et al., 2015; Pausata et al., 2015; Stevenson et al., 2016; Khodri et al., 2017; Predybaylo et al., 2017; Eddebbar et al., 2019] have shown that volcanic eruptions

increase the probability of an El Niño event in the following years, with a La Niña to follow [McGregor et al., 2010; Sun et al., 2019]. Likewise, an analysis of geoengineering experiments using stratospheric aerosols to counteract anthropogenic global warming found a slight increase in the probability of an El Niño event in the following year [Gabriel and Robock, 2015] and an El Niño-like shift in the decadal average temperature [Trisos et al., 2018]. The response of the ENSO to a global perturbation with near-decadal persistence has not been studied; the present nuclear war simulations provide an opportunity to examine this coupled ocean-atmosphere response at its most extreme.

Using CESM-WACCM4 and six different nuclear war scenarios, I demonstrate that global cooling generated by nuclear conflict initiates a large, sustained circulation response in the tropical Pacific. This “Nuclear Niño” exhibits qualitatively similar behavior to El Niño and its response to volcanic aerosol forcing, but is of a much larger magnitude and duration. The strong, almost decadal circulation response that occurs in the largest nuclear war scenario is unprecedented in the modern or paleoclimate ENSO record, highlighting the extreme nature of climate change after a nuclear conflict. Several mechanisms have been put forth to explain the link between aerosol-driven cooling and El Niño-like conditions. One theory suggests the equatorward shift of the ITCZ from the differential cooling of the Northern and Southern Hemisphere [Broccoli et al., 2006; Donohoe et al., 2012] could weaken the trade winds along the equator and trigger El Niño initiation [Pausata et al., 2015; Stevenson et al., 2016; Stevenson et al., 2017]. Others have suggested the response could be a consequence of: cooling the Maritime Continent which reduces the zonal Pacific SST gradient [Ohba et al., 2013], eastward-propagating Kelvin waves initiated by the cooling of Africa [Khodri et al., 2017], or the

"ocean dynamical thermostat mechanism" where cooling in the eastern Pacific is moderated by changes in the vertical structure of the ocean [McGregor et al., 2010; Clement et al., 1996]. I conducted sensitivity tests to understand and quantify the contribution of different mechanisms towards the extreme tropical Pacific circulation response in our simulations.

Strong El Niño events are associated with warming SSTs and reduced upwelling along the equatorial and eastern Pacific, which has historically limited fisheries production in the Peru-Chile and California upwelling systems through nutrient limitation [Chavez et al., 2011; Lehodey et al., 2006; Fisher et al., 2015]. The large variability in primary productivity in the equatorial Pacific is often responsible for driving changes to globally averaged productivity. For example, the 1997-1998 El Niño event caused global primary productivity to drop by 3 Pg of carbon per year, mostly due to reduced productivity in the eastern Pacific, which contributed to the collapse of anchovy fisheries off the coast of Chile [Lehodey et al., 2006]. Billions of dollars of economic activity are subject to temperature variability associated with ENSO, including 60% of global commercial tuna catches, which originate in the warm waters of the western and central Pacific and may benefit from warmer conditions [Lehodey et al., 2006*;* Fisher et al., 2015]. To help characterize the impact of nuclear war on marine productivity and the associated repercussions for food security I report on changes to net primary productivity (NPP) in the Equatorial Pacific. Large reductions in NPP are simulated following nuclear conflict and the mechanisms for this response are disentangled. Despite the strong link between equatorial Pacific NPP and El Niño events, reductions in solar radiation account are most important for the biological response.

Sensitivity tests to help quantify the contribution of different mechanisms towards the Nuclear Niño response in the 150 Tg United States and Russia nuclear war simulation (hereafter, NW-150Tg for brevity) were conducted with CESM-WACCM4 by selectively cooling different regions. Following the approach of Khodri et al. [2017], cooling is simulated by increasing the surface albedo to reflect the amount of solar radiation equivalent to that intercepted by soot aerosols in NW-150Tg. Three main experiments were performed, where cooling was applied over the Maritime Continent (EXP-MC), tropical Africa (EXP-TA), and the Northern Hemisphere (EXP-NH), with exact borders defined in Table 3.1. Surface cooling in EXP-MC and EXP-TA is designed to mimic diminished convection over those regions in NW-150Tg which has been suggested to be important for triggering an El Niño response [Ohba et al., 2013; Khodri et al., 2017]. EXP-NH simulates the differential cooling of the Northern and Southern Hemisphere to mimic the equatorward shift of the ITCZ. Separately, to explore the mechanisms responsible for changes in net primary production in NW-150Tg, I present an analysis conducted by my co-authors of Coupe et al. [2020] using the Biogeochemical Element Cycle Model to isolate the impacts of light, temperature, and nutrients on net primary production in the equatorial Pacific Ocean. Although this is not my sole and original analysis, it is included for additional context of the complete response of nuclear war to the equatorial Pacific Ocean.

3.1 Results: Nuclear Niño Response

Soot aerosols spread globally after they are injected into the upper atmosphere, causing strong global cooling and reduced precipitation across the tropics. The Nuclear Niño response that follows is illustrated for all scenarios in Figure 3.1 and is

characterized by a sudden increase in westerly surface wind stress along the western and central equatorial Pacific in the month after the injection (Figure 3.1a). This westerly anomaly, favorable for El Niño development and a fundamental feature of the Nuclear Niño response, continues to increase until it peaks during July-August-September. Westerly wind stress persists for up to seven years in NW-150Tg and the direction of the trade winds is reversed intermittently for three years. In response to anomalously westerly wind forcing, SSTs in the Niño3.4 region begin warming in all simulations despite the cooling effect of the stratospheric aerosol layer (Figure 3.2). The warming of the Niño3.4 region occurs after the westerly wind stress anomaly triggers an oceanic Kelvin wave and warm equatorial waters are advected eastward, deepening the thermocline in the central and eastern equatorial Pacific (Figure 3.3). Zonal advection is an especially prominent term in the equatorial Pacific mixed-layer heat budget for the 6-12 month period post-injection. Within a year, however, aerosol-driven cooling masks equatorial Pacific warming. Regardless of the actual SSTs, the zonal SST gradient across the Pacific is highly consequential for the atmospheric response. To filter out large-scale cooling, I subtract the average SST anomalies between 20°S and 20°N from the SST anomalies in the Niño3.4 region (5°N-5°S, 170°W-120°W) to get the relative Niño3.4 SSTs [Khodri et al., 2017]. I find anomalously warm relative SSTs along the equatorial Pacific for seven years in NW-150Tg (Figure 3.1b).

The relative Niño3.4 SSTs in NW-150Tg, even when normalized to account for higher amplitude El Niño events in our model, exceed the SST response for both the peak of the 1997-1998 and 2015-2016 El Niño events. The strong physical ocean response is exemplified by the change in the zonal SSH gradient between the east and west Pacific

Ocean, which is typically negative but shifts positive for all of the simulations except the 5 Tg soot case (Figure 3.1c). The normal circulation pattern of the equatorial Pacific Ocean is completely disrupted, as upwelling is shut down and in some cases reversed completely (Figure 3.1d). The reduction in upwelling is a positive contributor to anomalously warm conditions in the eastern equatorial Pacific for many years. In NW-150Tg, the Southern Oscillation Index (SOI) drops seven standard deviations within six months. The rate of the collapse of the Pacific Walker Circulation (inferred by changes in the SOI) in all simulations with more than 16 Tg of soot is unmatched by any event in the historical record, control run or 1200 years of the CESM Large Ensemble pre-industrial run [Kay et al., 2015]. This indicates the Nuclear Niño response is well outside the bounds of what might be expected due to unforced ENSO variability in the historical record and in the model climatology, even though CESM-WACCM4 simulates stronger ENSO variability than observations. The tendency for El Niño-like conditions is consistent with similar work modeling volcanic eruptions but clearly is more extreme [Mann et al., 2005; Emile-Geay et al., 2008; Ohba et al., 2013; Maher et al., 2015; Pausata et al., 2015; Stevenson et al., 2016; Khodri et al., 2017; Predybaylo et al., 2017; Eddebbar et al., 2019].

In the control run from which the initial conditions for all nuclear scenarios were obtained, neutral to La Niña-like conditions were simulated in the first year when the Nuclear Niño is initiated in the nuclear war scenarios. To examine the influence of initial conditions, I analyzed two additional ensembles of the 5 Tg soot case, one starting with neutral conditions and one with a developing El Niño. Regardless of initial conditions, in all three ensemble members an El Niño developed that continued through December-

January-February at least. In the case with the developing El Niño, adding 5 Tg of soot enhanced the strength of the response by 25% and the duration by two months compared to the control run. I conclude that the initial ENSO state affects but does not prevent the development of an El Niño in even the smallest war scenario.

An extreme Nuclear Niño response is not simply confined to the largest forcing scenario. The 27.3 Tg soot case with only 18% of the initial soot achieves more than 60% of the wind stress response of NW-150Tg. The strength and duration of the wind response is correlated with increased aerosol mass, although a saturation point occurs after 27.3 Tg (Figure 3.4). During the peak of the event, the 27.3 Tg, 37 Tg, and 46.8 Tg soot cases all have a similar surface wind stress forcing although the larger cases have a longer duration of El Niño-like conditions. While there is no long-duration El Niño in the 5 Tg case, the ensemble mean zonal wind stress forcing remains anomalously westerly for nearly two years. Reduced equatorial upwelling contributes to the prolonged circulation response by warming the eastern equatorial Pacific and maintaining a weakened zonal SST gradient in the Pacific for nearly seven years. The extended duration El Niño is also related to western Pacific SSTs remaining below the SST threshold required to initiate deep convection, allowing anomalous sinking air over the region for many years in the larger forcing scenarios.

3.2 Results: Mechanisms Contributing to Nuclear Niño Initiation

To understand the mechanisms responsible, I focus on the initiation of El Niño conditions in NW-150Tg, which has the largest perturbation and represents what can be described as the potential upper bound of an El Niño event. A series of changes occur in this simulation that are consistent with mechanisms previously invoked to explain El

Niño-like conditions following volcanic eruptions, such as differential cooling of the Maritime Continent relative to the central Pacific, strong cooling of the African continent, and an equatorward shift in the latitude of the ITCZ (Figure 3.5, 3.6). However, before the westerly trade wind anomaly spreads across the equatorial Pacific, there is an initial La Niña-like response in the eastern equatorial Pacific characterized by strong cooling, an increase in coastal upwelling, and anomalous easterly trade winds (Figure 3.5). The faster cooling of South America in contrast to the surrounding ocean is the most likely culprit for this easterly wind anomaly, which is confined to a localized coastal area in the lower troposphere and persists for less than six months. La Niña-like features can precondition the ocean for El Niño development through ENSO recharge dynamics [Emile-Geay et al., 2008; Stevenson et al., 2017], but this short-lived feature cannot account for the multi-year persistence of the Nuclear Niño response. Rather, the dominant driver in NW-150Tg appears to be the suppression of convection over the Maritime Continent region in response to cooling. This cooling also creates a localized weakening of the zonal temperature gradient in the western Pacific, contributing to the initial relaxation of the trade winds.

To quantify the contribution of different mechanisms towards the Nuclear Niño response, I conduct a series of sensitivity experiments where the surface albedo of specified regions (see Table 2) is increased to simulate the reduction in absorbed solar radiation at the surface in the original NW-150Tg simulation. The daily shortwave radiation anomaly as a fraction is extracted from NW-150Tg and is used to calculate the increase in albedo (X) that is necessary to reduce absorbed surface shortwave radiation. I calculate this quantity, $d\alpha\alpha$, for each day and grid point:

$$dX = -cf*(SWradiation\_150Tg - SWradiation\_climatology)/SWradiation\_climatology$$

dX is the daily climatological mean of shortwave radiation using the control run. A correction factor (*cf*) to eliminate the influence of clouds is calculated by taking the ratio of the monthly net surface solar flux and net clear-sky surface flux. This output was not available at the daily level so it had to be interpolated daily. $d\alpha\alpha$ is added to the direct shortwave albedo in CESM within the radiation code.

In these experiments, cooling the Maritime Continent (EXP-MC) and tropical Africa (EXP-TA) produced the strongest El Niño-like responses (Figure 3.7). In NW-150Tg, the peak in Pacific Ocean zonal surface wind stress anomalies (130°E-120°W, 5°S-5°N) favorable for El Niño development occurs during July-August-September of the first year. Wind stress anomalies for that same period in EXP-MC, EXP-TA, and EXP-NH are 71%, 31%, and 29% of the NW-150Tg forcing, respectively (Figure 3.7a). The peak in wind stress forcing in EXP-MC and EXP-TA occurs months later, during November-December-January. During this peak, wind stress in EXP-MC is greater than the peak in NW-150Tg. Maritime Continent region cooling is thus the most effective at generating the initial wind response that triggers the peak Nuclear Niño conditions in NW-150Tg. Reduced precipitation in response to cooling over the Maritime Continent produces anomalous sinking air and disrupts the Pacific Walker Circulation (Figure 3.8). The amount of cooling over the Maritime Continent in EXP-MC and NW-150Tg are similar by design but there is a greater reduction in precipitation and greater wind stress in EXP-MC that can be explained by a slightly weaker zonal SST gradient due to the lack of aerosol-driven cooling of the central and eastern Pacific Ocean. In terms of Niño3.4 relative SST anomalies, NW-150Tg's peak in October-November-December of the first

year is 0.3°C cooler than MC-EXP's February-March-April peak in the following year. Warmer SSTs peaking later in MC-EXP are expected with a later and stronger wind stress forcing. These results show that suppression of convection in this region, which is tightly linked to variations in the Pacific Walker Circulation, can generate wind stress and SST anomalies sufficient to explain the Nuclear Niño in NW-150Tg.

In EXP-TA, a strong El Niño-like response is also simulated, supporting the findings of Khodri et al. [2017] that the cooling of the African continent contributes to the development of El Niño-like conditions following aerosol-driven cooling. The collapse of the West African monsoon (Figure 3.8c) produces a mid-tropospheric heating anomaly, initiating an eastward propagating Kelvin wave along the equator that suppresses convection in its wake. After passing through the Maritime Continent and western Pacific, the waves generate westerly zonal wind stress anomalies. Surface wind stress anomalies in EXP-TA peak at the same time as in EXP-MC, but the peak is only 44% of the magnitude of EXP-MC. Niño3.4 relative SST anomalies are also cooler in EXP-TA compared to EXP-MC, suggesting the Maritime Continent cooling is the more dominant mechanism in this model configuration. However, a unique response occurs in EXP-TA, where warm SSTs appear in the eastern Pacific and along the coast of South America as well as in the central Pacific (Figure 3.7e). The cooling of the equatorial Atlantic Ocean in EXP-TA due to advection of cold air from the African continent leads to an Atlantic Niña-like pattern, which has been linked to warming in the equatorial Pacific [Khodri et al., 2017]. Reduced convection over the equatorial Atlantic (Fig. 3.8c) disrupts the Atlantic-Pacific Walker Circulation, contributing to the additional warming in the eastern Pacific by reducing the trade winds along the coast of western South

America more so than in EXP-MC and EXP-NH. While equatorial Atlantic cooling is also present in NW-150Tg, a coastal warming effect is likely to be masked by massive cooling of the nearby South American continent. The smaller magnitude of wind stress and relative SST anomalies in the traditional Niño3.4 region in EXP-TA (Fig. 3.7) suggests that this mechanism plays a smaller role in initiating the Nuclear Niño than Maritime Continent cooling. Still, the large response in EXP-TA is evidence of an important link between tropical African convection and ENSO.

In EXP-NH, I increase the albedo of the entire Northern Hemisphere north of 10°N to simulate differential cooling of the hemispheres while avoiding equatorial regions to estimate the contribution of the equatorward shift of the ITCZ that occurs in NW-150Tg (Fig 3.6). The areas in EXP-MC and EXP-TA were excluded from albedo modifications in EXP-NH; cooling in these regions is thus due solely to advection from other locations. In EXP-NH, El Niño conditions are simulated, but were the weakest of all the simulations. Wind stress forcing in the Pacific in EXP-NH peaks during August-September-October, more in agreement with NW-150Tg, but its peak is only 30% of NW-150Tg. This peak occurs as the ITCZ remains near the equator in defiance of its seasonal progression northward. The proximity of the ITCZ to the equator in the Pacific is enough to generate El Niño-like conditions, but not enough to generate the full Nuclear Niño response.

The three mechanisms investigated here do not constitute a linear decomposition of the NW-150Tg response, as evidenced by the fact that the linear addition of the wind stress forcing in EXP-TA and EXP-MC would be larger than the response in NW-150Tg. This is unsurprising, given the degree of coupling inherent in the tropical Pacific climate

system. A saturation effect exists for higher westerly wind stress forcing, meaning that though multiple regions cool in NW-150Tg, there are diminishing returns in the overall wind stress response generated. Additionally, sensitivity tests may not perfectly isolate individual mechanisms because of the potential for exaggerated zonal temperature gradients in EXP-TA and EXP-MC, as well as the advection of cold air into other regions that may influence ENSO. NW-150Tg may also include mechanisms that weaken the El Niño-like response that are not present in the sensitivity experiments, like the cooling of South America. While imperfect, the tests allow a reasonable assessment of the relative contribution of major mechanisms to the initial response. Multiple factors likely work together to initiate the El Niño-like conditions after aerosol-driven cooling, but our results indicate that the cooling of the Maritime Continent is the dominant mechanism, with contributions from cooling of the African continent and the equatorward shift of the ITCZ. After initiation, the multi-year persistence of the Nuclear Niño is driven by sustained trade wind forcing from the aforementioned mechanisms which continue to reinforce the Nuclear Niño even after initiation, in addition to internal Bjerknes feedback processes.

Previous work on volcanic eruptions and ENSO has suggested the ocean dynamical thermostat mechanism, where upwelling in the eastern Pacific moderates aerosol-forced cooling compared to the western Pacific, could contribute to the El Niño-like response following stratospheric aerosol injection [McGregor et al., 2010; Mann et al., 2005; Clement et al., 1996]. The dynamical thermostat does not seem to initiate the Nuclear Niño, as the zonal Pacific SST gradient and the westerly zonal wind anomaly initially both increase, in contrast to what would be predicted by preferential cooling of

the warm pool in the dynamical thermostat paradigm. In fact, the eastern equatorial Pacific initially cools off more than the rest of the basin (Figure 3.5). Additionally, the vertical thermal structure of the ocean is strongly modified by the massive aerosol-induced cooling, preventing the mean vertical temperature gradient from acting as a "thermostat."

The physical response of the tropical Pacific to nuclear conflict is clearly extreme, and the long persistence of these circulation changes suggests the potential for sustained and severe impacts on marine productivity and associated food security implications. Next, I present results that diagnose the biogeochemical changes. The analysis in the following section is mostly the product of my co-authors, but including this part of our collaboration helps to tie together the full impact of nuclear war on the equatorial Pacific Ocean.

3.3 Results: Changes to Net Primary Productivity

Marine phytoplankton NPP decreases substantially in NW-150Tg (Figure 3.9), with potentially severe consequences for regional marine ecosystems. NPP is the net fixation of carbon by photosynthetic phytoplankton, typically expressed as a rate (here, g C m^{-2} yr^{-1}), and is a driver for marine ecosystem and fisheries production [Stock et al., 2017, Lotze et al., 2019]. Under normal conditions, the model used here simulates particularly high mean annual NPP in the Eastern Equatorial Pacific biome and the Peru Exclusive Economic Zone (EEZ), yielding values of ~245 and ~280 g C m^{-2} yr^{-1} (Figure 3.9a), similar to estimates from satellite observations [Lotze et al., 2019]. In the aftermath of the 150 Tg soot injection, annual averaged NPP over the 2-5 years period post-injection declines by 37% to 155 g C m^{-2} yr^{-1} and 34% to 186 g C m^{-2} yr^{-1}, respectively in

the two regions (Figure 3.9b). This reduction is even more dramatic on the seasonal scale (Figure 3.9d), particularly in the Peru EEZ where large seasonal and inter-annual variability is typically driven by the variable nature of upwelling in this near-shore region *[*Lotze et al., 2019*]*. Reductions in monthly averaged NPP in the Peru EEZ routinely exceed 50%, and reach as high as 68% in the aftermath of the war, a reduction of ~200 g C m^{-2} yr^{-1}. Compared to the control climatology, such reductions in NPP, including many of the smaller nuclear war scenarios (Figure 3.10), are without precedent. These results indicate that nuclear conflict will lead to a sustained decrease in regional marine productivity, potentially harming fish catch [Stock et al., 2017].

3.4 Results: Mechanisms Behind Changes to Net Primary Productivity

Reductions in NPP are typically observed during El Niño events, but these are much smaller in magnitude and are driven by reduced upwelling of nutrient-rich water [Krumhardt et al., 2017; Chavez et al., 2009], a different mechanism than the dominant one simulated here. In the aftermath of nuclear war, much larger regional NPP reductions in the Eastern Equatorial Pacific biome and Peru EEZ are primarily driven by a reduction in incident light reaching the ocean's surface, i.e., surface photosynthetically active radiation (PAR). In the Eastern Equatorial Pacific biome, simulated phytoplankton division rates are limited by nutrient, temperature, and light limitation, all of which are modified by deeper mixed layer depths caused by surface cooling (Figure 3.11). Despite a reduction in equatorial upwelling (Figure 3.1d) of nutrient rich water, vertical nutrient transport is compensated by dramatically deeper mixed layer depths, which reach twice as deep as the control run and do not recover for over 5 years (Figure 3.11a). While the net result is relieved nutrient stress, temperature and light limitation are both exacerbated

(Figure 3.11c). The most pronounced effect is on light limitation, which is ~50% more limiting in the year following the conflict relative to the control. Changes to light limitation are dominated by a reduction in PAR across the upper water column, rather than deep mixing causing effective light limitation. Together, the combined effect of all three modified limitation terms is a 25% reduction in population specific division rates averaged over the five years following the conflict (Figure 3.11d), driving a 15% reduction in biomass (Figure 3.11e) and 34% reduction in NPP (Figure 3.9d) over the same period.

3.5 Summary

The physical and biological perturbations to the equatorial Pacific Ocean following nuclear conflict in the simulations are unprecedented compared to natural variations. The climate response to large-scale cooling suggests a distinct, extreme mode of ENSO which was not previously anticipated. An initial El Niño-like response was expected, as existing research links volcanic eruptions and ENSO, but a sustained response due to the long residence time of soot aerosols in the stratosphere has not been previously shown. For years, temperature and precipitation anomaly patterns in the Pacific Ocean are comparable to those observed during strong, basin-wide El Niño events. The atmospheric teleconnections associated with Nuclear Niño may differ from a traditional El Niño; however, a “nuclear winter” with plummeting global mean surface temperatures occurs regardless of any influence of the tropical Pacific Ocean. The Nuclear Niño response is terminated following years of aerosol removal, when solar radiation levels rise (Figure 3.6b) and the Maritime Continent begins warming. Termination of the response also coincides with the warming of tropical Africa and the

return of the ITCZ to its typical oscillatory pattern. Efforts to precisely understand the termination of the sustained response are confounded by the deactivation of the three main mechanisms at around the same time. Afterwards, there is a rebound towards La Niña-like conditions as the western Pacific warms more quickly than the eastern Pacific. This rebound is consistent with modeling work and observations after volcanic eruptions and large El Niño events in general [McGregor et al., 2010; Sun et al., 2019], but occurs years later. Ultimately, there is no clear process to mitigate the duration or strength of the Nuclear Niño event until enough aerosols are removed from the stratosphere and large-scale cooling can no longer be maintained.

I have shown that a range of nuclear war scenarios could induce an El Niño-like pattern of unprecedented magnitude and confirmed the contribution of at least three mechanisms towards this response. I confirm that the African land-cooling mechanism brought forward by Khodri et al. [2017] likely plays a role in the El Niño-like response to aerosol-driven cooling. The results, using a different model and a larger negative radiative perturbation, disagree on its relative importance compared to other mechanisms. This suggests mechanisms may be dependent on the model and radiative forcing, which merits further investigation with additional climate models. The negative effect of reduced light and surface cooling following an all-out nuclear war on net primary productivity is troubling because it is linked to the availability of food from the ocean. The reduction in solar radiation, a direct effect of the smoke, is the primary driver of dramatic reductions in NPP across the equatorial Pacific following the war. Although these substantial reductions in NPP are not predicated on the El Niño-like circulation response, they are likely exacerbated by the reduced upwelling. The additional stress of

light driven reductions to NPP will further impact fisheries already responding to changes in SST, oxygen and salinity traditionally associated with El Niño-like climate variability. Ensuing changes in the size, location, and distribution of fish populations could devastate fisheries, particularly in the southeast Pacific Ocean. The implications of significantly reduced ocean productivity, along with previously reported reductions in agriculture [e.g., Jägermeyr et al., 2019], are grave. The fatalities from even the largest India and Pakistan nuclear war scenario used in this study are estimated to be below 300 million people [Toon et al., 2019], and even if the entire populations of the United States and Russia perished from the direct effects of nuclear war, more than 7 billion survivors would be left behind. The simulations here add to the body of work showing the potential global consequences of a nuclear war and provide a first look at the mechanisms responsible for potential changes in marine circulation and productivity. These findings illustrate the potentially catastrophic global consequences of a nuclear conflict and highlight the role of coupled climate dynamics in sustaining climate change across multiple years.

CHAPTER 4: WINTER WARMING AND STRATOSPHERIC FORCING OF THE ARCTIC OSCILLATION IN NUCLEAR WAR SIMULATIONS

4.1 Evidence of a Perturbed Northern Hemisphere Wintertime Circulation

During the first and second winter (DJF) following simulations of the 150 Tg nuclear war scenario in GISS ModelE and CESM-WACCM4, anomalously warm surface temperatures are present in far northern Eurasia and northern polar regions despite reduced shortwave surface radiation (Figure 4.1). This winter warming can be seen in some of the other nuclear war simulations as well (see Figure 4.2), but the magnitude and spatial extent is somewhat inconsistent. When the response is present, it is a striking departure from the global signal and is reminiscent of the counter-intuitive temperature patterns observed after explosive tropical volcanic eruptions, which can be characterized by warming over Canada and the northern United States as well as over most of Eurasia. Figure 4.3 shows this observed pattern of surface temperature anomalies during the first DJF following the 1963 Agung eruption, the 1982 El Chichón eruption, and the 1991 Pinatubo eruption, using GISTEMP version 4 [Lennsen et al., 2019; GISTEMP, 2020]. After volcanic eruptions, the warming is greater in magnitude and is centered at a more southerly latitude compared to the patterns after an all-out nuclear war (Figure 4.1). Climate models, including the one used extensively in this dissertation, have been inconsistent at simulating the pattern observed after the three largest volcanic eruptions of the last 70 years, which has led to suggestions that winter warming following volcanic eruptions occurs by chance [Polvani et al., 2019]. Inspired by this type of investigative work that explores the potential connection between volcanic eruptions and the Arctic Oscillation (AO) / North Atlantic Oscillation (NAO), I examine the impact of

stratospheric soot aerosols on the AO in CESM-WACCM4, then investigate the mechanisms responsible. Previous work has suggested at least two viable mechanisms to explain the response after large tropical volcanic eruptions, which can be separated into a tropospheric and a stratospheric pathway. After providing evidence for the role of both pathways in producing the simulated response, I will conduct an additional experiment to isolate the tropospheric pathway to assess its influence on changes to Northern Hemisphere DJF circulation.

The Arctic Oscillation (AO) undergoes what can best be described as a regime change in response to the black carbon injections in CESM-WACCM4, especially in the 150 Tg US and Russia nuclear war simulation, where the winters are characterized by a positive AO and the summers are characterized by a negative AO. This is clear from Figure 4.4, which shows the 3-month running mean of the AO for all nuclear war simulations for (a) all months, (b) DJF, and (c) JJA. This seasonal oscillation pattern continues for 10 years in the NW-150Tg case, and the duration of this oscillation is correlated with initial aerosol mass. The negative AO during JJA is a more consistent response across all the simulations compared to the positive AO during DJF, but the year-after-year consistency of a positive AO pattern in DJF across most of the simulations is highly unlikely to occur by chance. Figure 4.5a demonstrates this, showing the probability density function (PDF) for the AO during DJF months for the control run (n=179 months) and for ten years of all of the nuclear war simulations (16 to 150 Tg cases, n = 30 months each; 5 Tg case with three ensembles, n = 90 months). A shift towards higher probabilities of the positive mode of the AO becomes clearer with greater amounts of soot aerosol mass. Figure 4.5b also shows the PDF of the climatological DJF

AO and simulated DJF AO after volcanic eruptions (Agung, El Chichón, Pinatubo) across 42 ensembles of the CESM Large Ensemble (Kay et al., 2015). The loading pattern for the AO, the first empirical orthogonal function of monthly sea level pressure, is calculated using each model's respective climatology. The Kolmogorov-Smirnov test was used to test the significance of the shift in the PDF of the AO. The null hypothesis that the PDF of the AO in each nuclear war simulation is the same as the PDF of AO of the unperturbed control climatology was tested and rejected for all simulations ($p<0.02$) except for the 5 Tg case ($p=0.15$). It is apparent that nuclear war simulations exhibit a much greater shift towards a positive AO DJF pattern compared to model simulations of volcanic eruptions, which has historically posed a great challenge for understanding the observed response after volcanic eruptions. In 42 ensembles of the CESM Large Ensemble, no statistically significant shift in the DJF or January-February-March (JFM) AO following the simulated mean response to the 1963 Agung, 1982 El Chichón, and 1991 Pinatubo volcanic eruptions could be found ($p=0.68$ for DJF, $p=0.49$ for JFM).

4.2 Evidence of the Stratospheric Pathway

The sheer magnitude of stratospheric heating from soot aerosols suggests the stratospheric pathway could be sufficient to induce the circulation response in NW-150Tg. Stratospheric temperatures are 100°C greater than the climatological mean temperature for NW-150Tg in many parts of the tropical stratosphere, far greater than what was observed following even the Pinatubo volcanic eruption. To quantify the pole-to-equator temperature gradient in the stratosphere, Figure 4.6 shows the anomaly of the temperature difference of the mid-latitudes (30°N-60°N) minus the polar regions (60°N-90°N) as a function of pressure level and time in NW-150Tg, as well as the zonal mean

zonal wind anomaly at 60°N. The differential aerosol heating with latitude establishes a strong pole-to-equator temperature gradient in the stratosphere that coincides with enhancement of zonal winds in the stratosphere during DJF. During JJA, when sunlight returns to the pole, intense heating of the polar stratosphere occurs and an anomalous reduction in the pole-to-equator temperature gradient precedes an easterly shift in the stratospheric winds. The winds of the stratospheric polar vortex (SPV), often measured as the zonal mean zonal winds between 10 hPa and 100 hPa and averaged zonally at 60°N, respond to changes in the temperature gradient almost instantly.

A simple linear regression of SPV strength at 50 hPa using the stratospheric temperature gradient (∇T_{50hPa}), defined as the difference in temperature at 50 hPa between the polar regions (60°N-90°N) and the mid-latitude regions (30°N-60°N), as the predictor, underestimates the enhanced SPV simulated in NW-150Tg when trained with the relationship between these two variables in the CESM-WACCM4 control run. The analysis was repeated at 10 hPa with similar results. This failure is driven by the absence of any similar stratospheric temperature gradients in the control run climatology compared to the extreme soot injection simulations. If the second ensemble member of the 5 Tg India and Pakistan temperature gradient data instead is used to train the linear regression model, it can predict much of the enhanced SPV strength at 50 hPa in NW-150Tg for six years before aerosol heating is diminished (Figure 4.7). As the 5 Tg simulation has significantly less surface cooling but significant aerosol heating, this regression can be expected to mostly represent the effect of differential stratospheric heating on SPV winds. Based on this simple linear regression that ignores the explicit representation of the dynamics, the stratospheric temperature gradient should be expected

to drive almost all the variations in the SPV for the first six years. The consistency of this response with the anticipated thermal wind response to the geopotential height gradients caused by aerosol heating suggests this statistical quantification is physically realistic. DallaSanta et al. [2019] previously indicated that the latitudinal distribution of the stratospheric pole-to-equator temperature gradient following volcanic eruptions would initially cause an acceleration of the zonal mean winds at 45°N and not in the region of the polar jet, but that resulting wave feedbacks would then accelerate the polar jet. In our simulations, this cannot be ruled out, but aerosol heating generates an intense temperature gradient north of 45°N as well.

Further evidence of the stratospheric pathway can be elucidated from an analysis of a time-height cross section of the AO (see Figure 4.8), showing the positive AO signal originating in the stratosphere and propagating vertically to the surface. The AO index at levels above the surface is computed using geopotential height anomalies at each corresponding level. During the summers, there is a similar downward propagation of the negative AO signal from the stratosphere as ∇T_{50hPa} reverses direction. However, as the positive AO pattern propagates vertically towards the surface, it tends to weaken, suggesting some resistance to this response in the lowest layers of the troposphere. This may have implications for surface impacts in Europe. Additionally, the negative AO response in summer is disconnected from the response in the stratosphere. After six years, aerosol heating is diminished and the amount of SPV strengthening that can be explained by the stratospheric temperature gradient begins to decrease, also suggesting another mechanism.

Polvani et al. [2019] found no meaningful relationship between SPV strengthening associated with volcanic eruptions (3-4 m/s according to Bittner et al., [2016a]) and the subsequent surface temperature anomaly response over Eurasia in a climate model. However, in NW-150Tg the peak strength of the SPV is at least 10 times stronger compared to simulations of explosive tropical volcanic eruptions. The response of surface temperatures to stratospheric changes is highly complex and is sensitive to the degree of coupling between the troposphere and stratosphere, the latitude of peak zonal mean zonal winds, and the initial tropospheric conditions. At 10 hPa, the SPV is at least 50 m/s greater than mean DJF conditions in NW-150Tg. Assuming that stratospheric aerosols are responsible for a 50 m/s acceleration of the SPV in NW-150Tg, I perform a linear regression of this SPV strength anomaly onto DJF temperature anomalies for all latitude and longitude coordinates using the relationship between the two variables in the model climatology. Zonal mean winds at 50 hPa averaged between 50°N-70°N are used as a predictor for DJF surface temperature anomalies. The surface temperature anomaly pattern expected from this acceleration of the SPV is characterized by strong warming over most of the Eurasian coast of the Arctic Ocean as well as Scandinavia (Figure 4.9). Interior Eurasia is significantly cooler in NW-150Tg compared to the regression; this can be explained by strong aerosol-driven cooling in the region, which is especially impactful for interior regions not within proximity of a body of water. The enhancement and latitudinal displacement of the SPV seems to modulate the surface temperature anomaly response in CESM-WACCM4. Thus, while the 1991 Pinatubo volcanic eruption did not generate a sufficiently strong SPV response to produce a statistically significant temperature response in the CESM Large Ensemble or the model ensemble used by

Polvani et al. [2019], the acceleration of the SPV in our NW-150Tg simulation is well beyond internal variability and would be expected to produce a significant temperature response if not for the intense cooling from the aerosols.

Using a simple linear regression model it is possible to predict large portions of SPV variability based on the differential stratospheric heating gradient as well as the surface temperature response to the strengthened SPV. A regression cannot account completely for the acceleration of the SPV in NW-150Tg (as expected) which can be explained by the deficiency of a statistical model to characterize the non-linear dynamics of the Northern Hemisphere wintertime circulation. Alternatively, this could be indirect evidence of the tropospheric pathway for acceleration of the SPV, which I will explore in the next section.

4.3 Evidence of the Tropospheric Pathway Perturbed Northern Hemisphere Wintertime Circulation

Next, I present evidence of the contribution of a tropospheric pathway for SPV strengthening in the six nuclear war scenarios, then I isolate the tropospheric pathway in a separate experiment. The tropospheric pathway for SPV acceleration is suggested to occur through the reduction of planetary wave activity entering the stratosphere [Graf et al., 1993, 2007]. As poleward and vertically propagating planetary waves enter the polar stratosphere, they tend to cause a slowing of the westerlies through increased wave-breaking and friction. One way to measure the impact of wave activity on the polar stratosphere is through meridional heat flux, which is equivalent to the vertical component of Eliassen-Palm (E-P) flux [Edmon et al., 1980]. The strength of the 1-month lagged 10 hPa zonal mean zonal wind anomaly at 60°N and 50 hPa meridional heat flux

between 50°N and 70°N in CESM-WACCM4 is negatively correlated, consistent with observations during December-January-February-March (DJFM) (Figure 4.10). Thus, if surface cooling following stratospheric aerosol injections reduces the generation of planetary wave activity in either the mid-latitudes or the tropics, this could cause a westerly acceleration of the SPV. In the mid-latitudes, a reduction in baroclinicity would tend to decrease the amplitude of synoptic scale Rossby waves, leading to less cyclonic wave-breaking at high latitudes. In the tropics, surface cooling would tend to reduce the amount of deep convection along the equator as large portions of the equatorial oceans struggle to reach the SST threshold for deep convection. I quantify changes to mid-latitude baroclinicity and tropical convection and show how they can influence the Northern Hemisphere winter circulation across the simulations.

All six nuclear war scenario simulations exhibit a slight reduction in the meridional surface temperature gradient in the mid-latitudes (~45°N), a proxy for baroclinicity, just prior to the strengthening of the SPV during the first winter. As the winter warming pattern develops over Eurasia, this gradient weakens further, a potential positive feedback for the reduction in baroclinicity. More robust is that averaged globally, tropical convection is reduced after soot injections, as indicated by Figure 4.11. Lower incident solar radiation at the surface produces less evaporation, reducing precipitation across the tropics, especially the Maritime Continent region and equatorial Africa. These two regions are especially important for the Nuclear Niño response (see Chapter 3). However, because of the Nuclear Niño response, there is an increase in precipitation in response to warmer SSTs and enhanced surface convergence in the eastern equatorial Pacific during the first winter. Thus, while tropical convection is reduced it undergoes a

spatial reorganization focused over the eastern equatorial Pacific Ocean. The subsequent increase in tropical convection over the eastern equatorial Pacific may have implications for North Atlantic region teleconnections that tend to favor a negative NAO pattern, especially during JFM [Trenberth et al., 1998; Jimenez et al., 2018].

Observational and modeling studies have found a robust negative correlation between Niño3.4 SSTs and North Atlantic sea level pressure due to the excitation of a Rossby wave train in the troposphere [Trenberth et al., 1998; Bronnimann, 2007; Jimenez et al., 2018]. This pattern is present in a 60-year control run of CESM-WACCM4, which also finds a strong correlation between warm Niño3.4 SSTs and anomalously high sea level pressure across Greenland and Iceland, consistent with a negative AO/NAO pattern. Consistent with the expected teleconnection, in all nuclear war simulations, lower pressure spans the Atlantic Ocean from the southeast US to the Iberian Peninsula at varying degrees of latitude, as shown in Figure 4.12. In every model simulation conducted here in which an El Niño-like response develops (including EXP-MC, EXP-TA, EXP-NH, EXP-GLB, and 5-150 Tg experiments), this sea level pressure pattern in the North Atlantic can be found. However, based on prior work, this connection operates solely in the troposphere. To understand changes to the stratosphere, I quantify wave activity entering the stratosphere as a result of reduced mid-latitude baroclinicity and tropical convection by calculating the vertical component of the Eliassen-Palm (E-P) flux as a function of latitude during the first DJF after the injections of soot.

Following a similar analysis in Stenchikov et al. [2002], Figure 4.13 shows the vertical component of E-P flux at 400 hPa zonally averaged for all six nuclear war simulations during the first Northern Hemisphere winter (DJF). An increase in initial

aerosol mass is associated with a reduction in upper tropospheric vertically propagating wave activity in the mid-latitudes (all zonal wave numbers included). This result is similar throughout the upper troposphere and is consistent with the reduction in waves approaching the stratosphere in the mid-latitudes. The result is also consistent with the theoretical basis for the tropospheric pathway of SPV acceleration. An analysis of E-P flux divergence in the equatorial region yields similar results, indicating a reduction in vertical and poleward propagating waves globally. However, this analysis does not conclusively prove or disprove the tropospheric pathway's potential role because of potential feedbacks that can influence these wave diagnostics. For example, an initial strengthening of the SPV due to aerosol heating could promote a positive feedback where a stronger SPV tends to deflect waves back towards the troposphere, leading to further strengthening. The results simply show that as initial aerosol mass is increased, the E-P flux in the mid-latitudes tends towards zero in the upper troposphere of the mid-latitudes and is greatly reduced when averaged across the equatorial regions. A better quantification of the mechanisms for the initial change to the SPV is possible through additional modeling experiments and leveraging experiments already conducted in Chapter 3.

4.4 Experiment to Isolate the Tropospheric Pathway

To better quantify the role of the tropospheric pathway, I apply the surface cooling from NW-150Tg in an additional sensitivity experiment starting from the same initial conditions as NW-150Tg, hereafter EXP-GLB. The albedo of the surface is increased globally (hence, EXP-GLB) to reflect the radiation equivalent to what is intercepted by soot aerosols in NW-150Tg using the same methods as in Chapter 3.

Using an extremely large surface temperature perturbation is useful because it helps mitigate the need for extensive ensembles in order to characterize the mechanisms responsible for changes to the atmospheric circulation. The influence of the aerosol heating in the stratosphere is eliminated and the difference between NW-150Tg and EXP-GLB is roughly approximate to the contribution from the stratospheric pathway, excluding wave feedbacks. Global mean surface temperature departures in NW-150Tg and EXP-GLB are comparable by design, but in NW-150Tg, an unprecedented and statistically significant SPV change occurs. In EXP-GLB, an acceleration of the SPV at 50 hPa, 60°N is simulated during the first DJF that is less than half of what occurs in even the 5 Tg soot case (Figure 4.14). At 10 hPa, the SPV intensification in EXP-GLB is less than a third of even the 5 Tg soot case. The max stratospheric wind anomaly shifts equatorward as aerosol mass increases, but in EXP-GLB, the peak is near 75°N, a similar latitude as in the 5 Tg soot case. While cooling of the surface only explains a fraction of the SPV strengthening compared to cases including aerosol heating, the changes that do occur are significant compared to the non-perturbed model climatology. Figure 4.14 shows the strength of the SPV at 50 hPa is more than two standard deviations from the model climatological mean value north of 60°N. This strengthened SPV propagates downward to the surface, causing a positive AO surface pattern in EXP-GLB.

EXP-GLB alone cannot distinguish whether reduced tropical convection or reduced mid-latitude baroclinicity is most important for the circulation response that is simulated, as it includes both. I use the EXP-NH simulation from Chapter 3, which has an increased albedo north of 10°N, for insight into the degree to which equatorial convection affects the response. In EXP-NH, mid-latitude baroclinicity is reduced, but equatorial

eastern Pacific convection is enhanced because of warmer equatorial SSTs. During the first JFM, a negative AO/NAO response is simulated at the surface in EXP-NH (see Figure 4.15c). When equatorial regions are cooled in EXP-GLB, a positive AO surface response is simulated, implying that the reduction in convection across the global equatorial regions is a stronger control on the positive AO surface response compared to mid-latitude cooling. Changes in tropical convection can both increase the strength of the SPV through reduced planetary wave activity and produce a Rossby wave train in the troposphere that shapes the negative NAO response. In all the sensitivity experiments conducted in Chapter 3 (EXP-MC, EXP-TA, and EXP-NH), a robust negative AO/NAO with higher sea level pressure anomalies at the northern pole and lower sea level pressure anomalies across the North Atlantic is simulated for the first winter (Figure 4.15) as a result of increased eastern equatorial Pacific convection. The inability of the strong, positive AO pattern to propagate completely from the stratosphere to the lower troposphere in NW-150Tg is largely a reflection of the negative NAO pattern in the troposphere. Although these results show the tropospheric pathway can be influential, it is apparent that the heating of the aerosols is the most direct and influential factor for the strengthening of the SPV during the first few winters following nuclear war.

4.5 Discussion

The post-nuclear war shift towards a positive AO state during boreal winters is best explained by the stratospheric temperature gradient generated by the heating of soot aerosols in the simulations presented here. Surface cooling and the subsequent reduction in tropical convection can contribute toward this state, but it can explain less than 25% of the strengthening of the winds of the stratosphere that causes the surface positive AO

pattern after propagating towards the surface. Our results provide support that a large enough volcanic eruption should be able to increase the likelihood of a positive AO response in the following winter, although models struggle to simulate this response for a Pinatubo-sized eruption. The circulation response is significant in the stratosphere with three ensembles of a 5 Tg soot injection and at the surface for injections with 16 Tg soot or greater in CESM-WACCM4. However, the response at the surface is less consistent, especially in terms of surface temperature, which does not become more robust with increased injection size because surface cooling also increases and internal variability is large.

The shift in the AO after nuclear war is a decadal event in these simulations, extending well beyond the first few winters and even after most aerosols have fallen out of the stratosphere. Aerosol heating in the stratosphere cannot explain the continuation of winters characterized by a strong, positive AO response more than 10 years following the soot injection. A few plausible mechanisms are the likely culprit. First, prolonged La Niña-like conditions follow the Nuclear Niño, which typically are associated with a stronger winter stratospheric polar vortex. Just as land areas cooled more quickly than the oceans after the soot injection, the oceans are slow to warm again after the aerosols fall out. Equatorial regions experience reduced convection, favoring the stronger stratospheric polar vortex and positive AO response during winter. Second, the expansion of sea ice area and volume in the Arctic contributes to cooler polar regions at the surface more than 10 years after the initial injection. Lower tropospheric geopotential heights as a result of this cooling anomaly may also contribute to the longer-term positive AO surface pattern. Finally, as Stenchikov et al. [2002] found in a modeling study, polar ozone

destruction as a result of stratospheric heating can generate stratospheric thermal gradients during the winter that can produce the positive AO response. Although not discussed here due to a lack of representation of all relevant processes to confidently simulation changes in stratospheric ozone, extensive ozone destruction is simulated in CESM-WACCM4 as well for more than a decade and could contribute to the long-term response once the soot aerosols no longer generate heating.

CHAPTER 5: SUMMARY AND DISCUSSION

This dissertation uses numerical models to understand the climate response to stratospheric black carbon injections as a result of nuclear war, a low probability but high impact event. Chapter 2 was motivated by the availability of climate models with more sophisticated aerosol treatment. Chapter 3 and 4 were motivated initially by observations made using the climate model simulations in Chapter 2 and outstanding questions surrounding the underlying dynamics of the simulated response. The relevance of the dynamical changes discussed in Chapter 3 and Chapter 4 to ongoing debates about how volcanic eruptions can influence modes of climate variability motivated further study and sensitivity tests to understand the mechanisms responsible.

In Chapter 2, I presented evidence that the climate impacts of the 150 Tg United States and Russia nuclear war scenario are extremely similar whether conducted using a crude, low resolution model or a state-of-the-art Earth system model with explicit treatment of black carbon aerosols. I quantified the negative effect of climate change following this nuclear war scenario on growing season, which has important implications for human survival.

In Chapter 3, I examine “Nuclear Niño,” a robust response to nuclear war in six different model simulations. I quantify how anomalous the response is in terms of the Walker Circulation response as well as changes to the ocean such as upwelling. I relate this change to what models simulate after volcanic eruptions and I conduct sensitivity tests using the forcing from nuclear war scenarios to understand the mechanisms. I conclude that multiple mechanisms can initiate the response, but the mechanisms in order of importance are: cooling of the Maritime Continent, cooing of tropical Africa, and the

equatorward shift of the ITCZ. These results contribute to the ongoing debate over the mechanisms responsible for the link between volcanic eruptions and El Niño and confirms a recently proposed mechanism that had not yet been tested beyond a single climate model.

In Chapter 4, I explore the Northern Hemisphere winter circulation response to nuclear war in six model simulations. I show that a strengthening of the SPV is a robust response in this climate model to nuclear war which is most readily explained by the heating of aerosols in the stratosphere. Additionally, tropospheric cooling can generate a small, but significant response in the stratosphere. However, winter warming of the Northern Hemisphere continents is not as robust as the acceleration of the SPV. Stratospheric changes are not always linearly projected onto surface impacts because of large internal variability. Surface temperature changes are determined by changes to the regional shortwave and longwave heat budget, and while a slight positive shift in the lower tropospheric AO index would favor the advection of warm air over northern Eurasia, this clearly is not enough to guarantee that the surface temperature anomalies shown in Figure 4.9a will occur. This is unsatisfying, given the observed surface temperature pattern following the last three large volcanic eruptions in the 20th century (Figure 4.3), but is consistent with even high-top climate models showing large internal variability which prevents a consistent surface response. However, this points the way to future investigations to better understand under what conditions an acceleration in the SPV due to aerosol heating will become coupled to the lower troposphere.

References

Adams, J.B., Mann, M.E. & Ammann, C.M. (2003). Proxy evidence for an El Niño-like response to volcanic forcing. *Nature*, 426, 274-278. https://doi.org/10.1038/nature02101

Aleksandrov, V. V., & Stenchikov, G. L. (1983). On the modelling of the climatic consequences of the nuclear war. *In The Proceedαing on Appliedα Mathematics* (21 pp.). Moscow: Computing Centre, USSR Academy of Sciences.

Bardeen, C. G., Garcia, R. R., Toon, O. B., & Conley, A. J. (2017). On transient climate change at the Cretaceous Paleogene boundary due to atmospheric soot injections. *Proceedαings of the National Acadαemy of Sciences of the Unitedα States of America*, 114, E7415–E7424. https://doi.org/10.1073/pnas.1708980114

Bardeen, C. G., Toon, O. B., Jensen, E. J., Marsh, D. R., & Harvey, V. L. (2008). Numerical simulations of the three dimensional distribution of meteoric dust in the mesosphere and upper stratosphere. *Journal of Geophysical Research*, 113, D17202. https://doi.org/10.1029/2007JD009515

Bellenger, H., Guilyardi, E., Leloup, J., Lengaigne, M. & Vialard, J. (2014). ENSO representation in climate models: From CMIP3 to CMIP5. *Clim Dyn.*, 42, 1999-2018. https://doi.org/10.1007/s00382-013-1783-z

Bittner, M. (2015). On the discrepancy between observed and simulated dynamical responses of Northern Hemisphere winter climate to large tropical volcanic eruptions, Ph.D. thesis, University of Hamburg, *Reports on Earth System Science*, no. 173.

Bittner, M., Schmidt, H., Timmreck, C., & Sienz, F. (2016a). Using a large ensemble of simulations to assess the Northern Hemisphere stratospheric dynamical response to tropical volcanic eruptions and its uncertainty, *Geophys. Res. Lett*., 43, 9324–9332. https://doi.org/10.1002/2016GL070587

Bittner, M., Timmreck, C., Schmidt, H., Toohey, M., & Krüger, K. (2016b). The impact of wave–mean flow interaction on the Northern Hemisphere polar vortex after tropical volcanic eruptions. *J. Geophys. Res.*, 121, 5281–5297. https://doi.org/10.1002/2015JD024603.

Bjerknes, J. (1969). Atmospheric Teleconnections From The Equatorial Pacific. *Mon. Wea. Rev.*, 97, 163–172, https://doi.org/10.1175/1520-0493(1969)097<0163:ATFTEP>2.3.CO;2.

Bond, T. C., & Bergstrom, R. W. (2006). Light Absorption by Carbonaceous Particles: An Investigative Review. *Aerosol Science andα Technology*, 40(1), 27–67. https://doi.org/10.1080/02786820500421521

Broccoli, A. J., Dahl, K. A., and Stouffer, R. J. (2006). Response of the ITCZ to Northern Hemisphere cooling, *Geophys. Res. Lett.*, 33, L01702, http://doi.org/10.1029/2005GL024546.

Brönnimann, S. (2007). Impact of El Niño–Southern Oscillation on European climate, *Rev. Geophys*., 45, RG3003, http://doi.org/10.1029/2006RG000199.

Chavez, P. & Messié, M. (2009). A comparison of Eastern Boundary Upwelling Ecosystems. *Progress in Oceanography*, 83, 80-96 (2009). https://doi.org/10.1016/j.pocean.2009.07.032

Chavez, F., Messié, P.M., & Pennington, J.T. (2011). Marine primary production in relation to climate variability and change. *Annual Review of Marine Science*, 3, 227-260. http://doi.org/10.1146/annurev.marine.010908.163917

Chiarenza, A.A., Farnsworth, A., Mannion, P.D., Lunt, D.J., Valdes, P.J., Morgan, J.V., & Allison, P.A. (2020). Asteroid impact, not volcanism, caused the end-Creteaceous dinosaur extinction. *Proceedαings of the National Acadαemy of Sciences*, 0027-8424. http://doi.org/10.1073/pnas.2006087117

Clement, A.C., Seager, R., Cane, M.A. & Zebiak, S.E. (1996). An ocean dynamical thermostat. *J. Climate*, 9, 2190-2196. https://doi.org/10.1175/1520-0442(1996)009<2190:AODT>2.0.CO;2

Coupe, J., Bardeen, C. G., Robock, A., & Toon, O. B. (2019). Nuclear winter responses to nuclear war between the United States and Russia in the Whole Atmosphere Community Climate Model Version 4 and the Goddard Institute for Space Studies ModelE. *Journal of Geophysical Research: Atmospheres*, 124, 8522-8543. https://doi.org/ 10.1029/2019JD030509

Coupe, J., Stevenson, S., Lovenduski, N.S., Rohr, T., Harrison, C.S., Robock, A., Olivarez, H., Bardeen, C.G., Toon, O.B. (2020). Nuclear Niño: A Large, Sustained Pacific Circulation Response to Nuclear Conflict. Under Review at *Communications Earth andα Environment.*

Crutzen, P. J., & Birks, J. W. (1982). The atmosphere after a nuclear war: Twilight at noon. *Ambio*, 50, 114–125. https://doi.org/10.1007/978_3_319_27460_7_5

DallaSanta, K., E. P. Gerber, & Toohey, M. (2019). The Circulation Response to Volcanic Eruptions: The Key Roles of Stratospheric Warming and Eddy Interactions. *J. Climate*, 32, 1101–1120, https://doi.org/10.1175/JCLI-D-18-0099.1.

Donohoe, A., Marshall, J., Ferreira, D. & McGee, D. (2012). The relationship between ITCZ location and cross-equatorial atmospheric heat transport: From the seasonal cycle to the Last Glacial Maximum. *J. Climate*, 26, 3597-3618. https://doi.org/10.1175/JCLI-D-12-00467.1

Eddebbar, Y. A., K. B. Rodgers, M. C. Long, A. C. Subramanian, S. Xie, & Keeling, R.F. (2019). El Niño–Like Physical and Biogeochemical Ocean Response to Tropical Eruptions. *J. Climate*, 32, 2627–2649, https://doi.org/10.1175/JCLI-D-18-0458.1.

Edmon, H.J., B.J. Hoskins, & McIntyre, M.E. (1980). Eliassen-Palm cross sections for the troposphere. *J. Atmos. Sci.*, 37:2600-2616. http://dx.doi.org/10.1175/1520-0469(1980)037<2600:EPCSFT>2.0.CO;2

Emile-Geay, J., Seager, R., Cane, M.A., Cook, E.R. & Haug, G.H. (2008). Volcanoes and ENSO over the past millennium. *J. Climate*, 21, 3134-3148. https://doi.org/10.1175/2007JCLI1884.1

FAO. (2018). The State of World Fisheries and Aquaculture 2018 - Meeting the sustainable development goals. http://www.fao.org/3/i9540en/i9540en.pdf

Fisher, J.L., Peterson, W.T. & Rykaczewski, R.R. (2015). The impact of El Niño events on the pelagic food chain in the northern California Current. *Global Change Biology*, 21, 4401–4414. https://doi.org/10.1111/gcb.13054

Gabriel, C.J. & Robock, A. (2015). Stratospheric geoengineering impacts on El Niño/Southern Oscillation. *Atmos. Chem. Phys.*, 15, 11949-11966. https://doi.org/10.5194/acp-15-11949-2015

GISTEMP Team. (2020). GISS Surface Temperature Analysis (GISTEMP), version 4. NASA Goddard Institute for Space Studies. Dataset accessed 2020-03-15 at data.giss.nasa.gov/gistemp/.

Graf, H., Kirchner, I., Robock, A., & Schult, I. (1993). Pinatubo eruption winter climate effects: Model versus observations, *Clim. Dynam*., 9, 81–93. https://doi.org/10.1007/BF00210011

Graf, H.F., Li, Q., & Giorgetta, M. A. (2007). Volcanic effects on climate: revisiting the mechanisms. *Atmos. Chem. Phys*., 7, 4503– 4511. https://doi.org/10.5194/acp-7-4503-2007

Groisman, P. Y. (1992). Possible regional climate consequences of the Pinatubo eruption: An empirical approach. *Geophys. Res. Lett*., 19, 1603–1606. https://doi.org/10.1029/92GL01474

Jiménez-Esteve, B., & Domeisen, D. I. V. (2018). The Tropospheric Pathway of the ENSO–North Atlantic Teleconnection. *J. Climate*, 31, 4563–4584. https://doi.org/10.1175/JCLI-D-17-0716.1.

Kay, J. E., et al. (2015). The Community Earth System Model (CESM) Large Ensemble Project: A Community Resource for Studying Climate Change in the Presence of Internal Climate Variability. *Bull. Amer. Meteor. Soc*., 96, 1333–1349, https://doi.org/10.1175/BAMS-D-13-00255.1.

Kelly, P. M., Jia, P., and Jones, P. (1996). The spatial response of the climate system to explosive volcanic eruptions. *Int. J. Climatol.*, 16, 537– 550. https://doi.org/10.1002/(SICI)1097-0088(199605)16:5%3C537::AID-JOC23%3E3.0.CO;2-F

Khodri, M., Izumo, T., Vialard, J., Janicot, S., Cassou, C., Lengaigne, M., Mignot, J., Gastineau, G., Guilyardi, E., Lebas, N., Robock, A. & McPhaden, M. (2017). Tropical explosive volcanic eruptions can trigger El Niño by cooling tropical Africa. *Nature Communications*, 8, 778. https://dx.doi.org/10.1038%2Fs41467-017-00755-6

Kirchner, I., Stenchikov, G. L., Graf, H.-F., Robock, A., and Antuña, J. C. (1999). Climate model simulation of winter warming and summer cooling following the 1991 Mount Pinatubo volcanic eruption. *J. Geophys. Res. Atmos*., 104, 19039–19055. https://doi.org/10.1029/1999JD900213

Kodera, K. (1994). Influence of volcanic eruptions on the troposphere through stratospheric dynamical processes in the northern hemisphere winter. *J. Geophys. Res. Atmos.*, 99, 1273–1282. https://doi.org/10.1029/93JD02731

Kravitz, B., A. Robock, D. T. Shindell, & M. A. Miller. (2012). Sensitivity of stratospheric geoengineering with black carbon to aerosol size and altitude of injection. *J. Geophys. Res.*, 117, D09203. https://doi.org/10.1029/2011JD017341

Krumhardt, K., Lovenduski, N., Long, M. & Lindsay, K. (2017). Avoidable impacts of ocean warming on marine primary production: Insights from the CESM ensembles. *Global Biogeochem. Cycles*, 31, 114-133. https://doi.org/10.1002/2016GB005528

Lehodey, P., Alheit, J., Barange, M., Baumgartner, T., Beaugrand, G., Drinkwater, K., Fromentin, J.M., Hare, S.R., Ottersen, G., Perry, R.I., Roy, C., van der Lingen, C.D. & Werner, F. (2006). Climate Variability, Fish, and Fisheries. *J. Climate*, 19, 5009–5030. https://doi.org/10.1175/JCLI3898.1

Lenssen, N., Schmidt, G., Hansen, J., Menne, M., Persin, A., Ruedy, R., Zyss, D. (2019). Improvements in the GISTEMP uncertainty model. *J. Geophys. Res. Atmos*., 124, 12, 6307-6326. http://doi.org/10.1029/2018JD029522

Lewis, K. N. (1979). The prompt and delayed effects of nuclear war. *Scientific American*, 241(1), 35–47. https://doi.org/10.1038/scientificamerican0779_35

Lotze, H. et al. (2019). Global ensemble projections reveal trophic amplification of ocean biomass declines with climate change. *Proc. Natl. Acadα. Sci.*, 116, 12907-12912. http://doi.org/10.1073/pnas.1900194116

Li, J., Xie, S., Cook, E.R., Morales, M.S., Christie, D.A., Johnson, N.C., Chen, F., D'Arrigo, R., Fowler, A.M., Gou, X. & Fang, K. (2013). El Niño modulations over the past seven centuries. *Nature Climate Change*, 3, 822-826. https://doi.org/10.1038/nclimate1936

Maher, N., McGregor, S., England, M.H. & Sen Gupta, A. (2015). Effects of volcanism on tropical variability. *Geophys. Res. Lett.*, 42, 6024-6033. https://doi.org/10.1002/2015GL064751

Malone, R. C., Auer, L., Glatzmaier, G., Wood, M., & Toon, O. B. (1985). Influence of solar heating and precipitation scavenging on the simulated lifetime of post nuclear war smoke. *Science*, 230(4723), 317–319. https://doi.org/10.1126/science.230.4723.317

Mann, M.E., Cane, M.A., Zebiak, S.E. & Clement, A. (2005). Volcanic and solar forcing of the tropical Pacific over the past 1000 years. *J. Climate*, 18, 447-456. https://doi.org/10.1175/JCLI-3276.1

Marsh, D.R., Mills, M.J., Kinnison, D.E., Lamarque, J., Calvo, J.N. & Polvani, L.M. (2013). Climate change from 1850 to 2005 simulated in CESM1 (WACCM). *J. Climate*, 26, 7372-7391. https://doi.org/10.1175/JCLI-D-12-00558.1

McCusker, K. E., Battisti, D.S., & Bitz, C.M. (2015). Inability of stratospheric sulfate aerosol injections to preserve the West Antarctic Ice Sheet. *Geophys. Res. Lett.*, 42, 4989–4997. https://doi.org/10.1002/2015GL064314

McGregor, S. Timmermann, A. & Timm, O.E. (2010). A unified proxy for ENSO and PDO variability since 1650. *Climate of the Past*, 6, 1-17. https://doi.org/10.5194/cp-6-1-2010

Mills, M. J., Toon, O. B., Turco, R. P., Kinnison, D. E., & Garcia, R. R. (2008). Massive global ozone loss predicted following regional nuclear conflict. *Proceedαings of the National Acadαemy of Sciences*, 105(14), 5307–5312. https://doi.org/10.1073/pnas.0710058105

Mills, M. J., Toon, O. B., Lee Taylor, J., & Robock, A. (2014). Multidecadal global cooling and unprecedented ozone loss following a regional nuclear conflict. *Earth's Future*, 2, 161–176. https://doi.org/10.1002/2013EF000205

Moore, J.K., Lindsay, K., Doney, S.C., Long, M.C. & Misumi, K. (2013). Marine Ecosystem Dynamics and biogeochemical cycling in the Community Earth System Model [CESM1(BGC)]: Comparison of the 1990s with the 2090s under the RCP4.5 and RCP8.5 Scenarios. *J. Climate*, 26, 9291–9312. https://doi.org/10.1175/JCLI-D-12-00566.1

Ohba, M., Shiogama, H., Yokohata, T. & Watanabe, M. (2013). Impact of strong tropical volcanic eruptions on ENSO simulated in a coupled GCM. *J. Climate*, 26, 5169-5182. https://doi.org/10.1175/JCLI-D-12-00471.1

Pausata, F., Chafik, L., Caballero, R., & Battisti, D. (2015). Impacts of high latitude volcanic eruptions on ENSO and AMOC. *Proceedαings of the National Acadαemy of Sciences of the Unitedα States of America*, 112, 13,784–13,788. https://doi.org/10.1073/pnas.1509153112

Pausata, F.S.R., Lindvall, J., Eckman, A.M.L. & Svensson, G. (2016). Climate effects of a hypothetical regional nuclear war: Sensitivity to emission duration and particle composition. *Earth's Future*, 4, 498–511. https://doi.org/10.1002/2016EF000415

Polvani, L. M., Banerjee, A., and Schmidt, A. (2019). Northern Hemisphere continental winter warming following the 1991 Mt. Pinatubo eruption: reconciling models and observations. *Atmos. Chem. Phys*., 19, 6351–6366. https://doi.org/10.5194/acp-19-6351-2019

Pittock, A. B., Ackerman, T. P., Crutzen, P. J., MacCracken, M. C., Shapiro, C. S., & Turco, R. P. (1986). Environmental consequences of nuclear war. *SCOPE*, 28, Physical and Atmospheric Effects (Vol. I). New York: John Wiley.

Predybaylo, E., Stenchikov, G. L., Wittenberg, A. T., and Zeng, F. (2017). Impacts of a Pinatubo Size Volcanic Eruption on ENSO. *J. Geophys. Res. Atmos.*, 122, 925–947. https://doi.org/10.1002/2016JD025796

Reisner, J., D'Angelo, G., Koo, E., Even, W., Hecht, M., Hunke, E., et al. (2018). Climate impact of a regional nuclear weapons exchange: An improved assessment based on detailed source calculations. *Journal of Geophysical Research: Atmospheres*, 123, 2752– 2772. https://doi.org/10.1002/2017JD027331

Robock, A. (2015). A Modest Proposal. *Huffington Post.* https://www.huffpost.com/entry/a-modest-proposal_15_b_8059256

Robock, A. (2000). Volcanic eruptions and climate. *Reviews of Geophysics*, 38(2), 191–219. https://doi.org/10.1029/1998rg000054

Robock, A. & Free, M. (1995). Ice cores as an index of global volcanism from 1850 to the present. *J. Geophys. Res.*, 100, 11,549-11,567.

Robock, A., & Mao, J. (1992). Winter warming from large volcanic eruptions. *Geophysical Research Letters*, 19(24), 2405–2408. https://doi.org.10.1029/92gl02627

Robock, A., Oman, L., & Stenchikov, G. L. (2007a). Nuclear winter revisited with a modern climate model and current nuclear arsenals: Still catastrophic consequences. *Journal of Geophysical Research*, 112, D13107. https://doi.org/10.1029/2006JD008235

Robock, A., Oman, L., Stenchikov, G. L., Toon, O. B., Bardeen, C., & Turco, R. P. (2007b). Climatic consequences of regional nuclear conflicts. *Atmospheric Chemistry andα Physics*, 7, 2003–2012. https://doi.org/10.5194/acp_7_2003_2007

Schmidt, G. A., Ruedy, R., Hansen, J. E., Aleinov, I., Bell, N., Bauer, M., et al. (2006). Present day atmospheric simulations using ModelE: Comparison to in situ, satellite, and reanalysis data. *Journal of Climate*, 19, 153–192. https://doi.org/10.1175/JCLI3612.1

Shindell, D. T., Schmidt, G. A., Mann, M. E., and Faluvegi, G. (2004). Dynamic winter climate response to large tropical volcanic eruptions since 1600. *J. Geophys. Res. Atmos.*, 109, D05104, https://doi.org/10.1029/2003JD004151.

Stenchikov, G., Robock, A., Ramaswamy, V., Schwarzkopf, D., Hamilton, K., & Ramachandran, S. (2002). Arctic Oscillation response to the 1991 Mount Pinatubo eruption: Effects of volcanic aerosols and ozone depletion. *Journal of Geophysical Research*, 107(D24), 4803. https://doi.org/10.1029/2002JD002090

Stenke, A., Hoyle, C. R., Luo, B., Rozanov, E., Gröbner, J., Maag, L., et al. (2013). Climate and chemistry effects of a regional scale nuclear conflict. *Atmospheric Chemistry andα Physics*, 13(19), 9713–9729. https://doi.org/10.5194/acp_13_9713_2013

Stevenson, S., Fasullo, J.T., Otto-Bliesner, B.L., Tomas, R.A. & Gao, C. (2017), Role of eruption season in reconciling model and proxy responses to tropical volcanism. *Proc. Natl. Acadα. Sci*., 114, 1822-1826. https://doi.org/10.1073/pnas.1612505114

Stevenson, S., Otto-Bliesner, B., Fasullo, J. & Brady, E. (2016). El Niño-like hydroclimate responses to last millennium volcanic eruptions. *J. Climate,* 29, 2907-2921. https://doi.org/10.1175/JCLI-D-15-0239.1

Stock, C.A., John, J.G., Rykaczewski, R., Asch, R., Cheung, W., Dunne, J., Friedland, K., Lam, V., Sarmiento, J. & Watson, R. (2017). Reconciling fisheries catch and ocean productivity. *Proc. Natl. Acadα. Sci.*, 114, E1441-E1449. http://doi.org/10.1073/pnas.1610238114

Sun, W., Liu, J., Wang, B., Chen, D., Liu, F., Wang, Z., Ning, L. & Chen, M. A. (2019). "La Niña- like" state occurring in the second year after large tropical volcanic eruptions during the past 1500 years. *Climate Dynamics,* 52, 7495-7509. https://doi.org/10.1007/s00382-018-4163-x

Toohey, M., Krüger, K., Bittner, M., Timmreck, C., and Schmidt, H. (2014). The impact of volcanic aerosol on the Northern Hemisphere stratospheric polar vortex: mechanisms and sensitivity to forcing structure. *Atmos. Chem. Phys*., 14, 13063–13079, https://doi.org/10.5194/acp-14-13063-2014

Toon, O.B., Bardeen, C.G., Robock, A., Xia, L., Kristensen, H., McKinzie, M., Harrison, C.S., Lovenduski, N.S. & Turco, R.P. (2019). Rapidly expanding nuclear arsenals in Pakistan and India portend regional and global catastrophe. *Science Adαvances*, 5, eaay5478. http://doi.org/10.1126/sciadv.aay5478

Toon, O. B., Robock, A., & Turco, R. P. (2008). Environmental consequences of nuclear war. *Physics Todαay*, 61, 37–42. https://doi.org/ 10.1063/1.3047679

Toon, O. B., Robock, A., Turco, R. P., Bardeen, C., Oman, L., & Stenchikov, G. L. (2007). Consequences of regional scale nuclear conflicts. *Science,* 315, 1224–1225. https://doi.org/10.1126/science.1137747

Toon, O. B., Turco, R. P., Westphal, D., Malone, R., & Liu, M. S. (1988). A multidimensional model for aerosols—Description of computational analogs. *Journal of the Atmospheric Sciences*, 45(15), 2123–2144. https://doi.org/10.1175/15200469(1988)045<2123: AMMFAD>2.0.CO;2

Trenberth, K. (1997). The definition of El Niño. *Bull. Amer. Soc.*, 78, 2771-2778. https://doi.org/10.1175/1520-0477(1997)078%3C2771:TDOENO%3E2.0.CO;2

Trenberth, K. E., Branstator, G. W., Karoly, D., Kumar, A., Lau, N.C., & Ropelewski, C. (1998). Progress during TOGA in understanding and modeling global teleconnections associated with tropical sea surface temperatures. *J. Geophys. Res*., 103(C7), 14291– 14324. http://doi.org/10.1029/97JC01444.

Trisos, C.H., Giuseppe, A., Gurevitch, Robock, A., Xia, L. & Zambri. B. (2018). Potentially dangerous consequences for biodiversity of solar geoengineering

implementation and termination. *Nature Ecology & Evolution,* 2, 475-482. https://doi.org/10.1038/s41559-017-0431-0

Turco, R. P., Toon, O. B., Ackerman, T. P., Pollack, J. B., & Sagan, C. (1983). Nuclear winter: Global consequences of multiple nuclear explosions. *Science*, 222(4630), 1283–1292. https://doi.org/10.1126/science.222.4630.1283

Turco, R. P., Hamill, P., Toon, O. B., Whitten, R. C., & Kiang, C. S. (1979). One dimensional model describing aerosol formation and evolution in the stratosphere: 1. Physical processes and mathematical analogs. *Journal of the Atmospheric Sciences*, 36(4), 699–717. https://doi.org/10.1175/15200469(1979)036<0699:AODMDA>2.0.CO;2

Xia, L., & Robock, A. (2013). Impacts of a nuclear war in South Asia on rice production in mainland China. *Climatic Change*, 116, 357–372. https://doi.org/10.1007/s10584_012_0475_8

Xia, L., Robock, A., Mills, M., Stenke, A., & Helfand, I. (2015). Decadal reduction of Chinese agriculture after a regional nuclear war. *Earth's Future*, 3, 37–48. https://doi.org/10.1002/2014EF000283

Yu, P., Toon, O.B., Bardeen, C.G., Zhu, Y., Rosenlof, K.H., Portmann, R.W., Thornberry, T.D., Gao, R.S., Davis, S.M., Wolf, E.T., deGouw, J., Peterson, D.A., Fromm, M.D. & Robock, A. (2019). Black carbon lofts wildfire smoke high into the stratosphere to form a persistent plume. *Science*, 365, 587–590. http://doi.org/10.1126/science.aax1748

Zambri, B. and Robock, A. (2016). Winter warming and summer monsoon reduction after volcanic eruptions in Coupled Model Intercomparison Project 5 (CMIP5) simulations. *Geophys. Res. Lett.*, 43, 10920–10928, https://doi.org/10.1002/2016GL070460

Zambri, B., LeGrande, A. N., Robock, A., & Slawinska, J. (2017). Northern Hemisphere winter warming and summer monsoon reduction after volcanic eruptions over the last millennium. *J. Geophys. Res. Atmos*., 122, 7971– 7989. https://doi.org/10.1002/2017JD026728

Zebiak, S. E., & Cane, M.A. (1987). A Model El Niño–Southern Oscillation. *Mon. Wea. Rev.*, 115, 2262–2278, https://doi.org/10.1175/1520-0493(1987)115<2262:AMENO>2.0.CO;2.

Tables

Table 2.1. Nuclear war scenarios used in CESM-WACCM4, showing the injection quantity into the upper troposphere, the nations involved, the number of weapons used, and the average explosive power of the nuclear weapons in terms of kilotons of TNT. The injection date is 15 May for all the scenarios.

Black Carbon (Tg)	Countries	Number of Weapons	Average Yield (kt)
150	United States, Russia	3100-4400	100-500
46.8	India, Pakistan	500	100
37	India, Pakistan	250	100
27.3	India, Pakistan	250	50
16	India, Pakistan	250	15
5 (3 ensembles)	India, Pakistan	44	15

Table 3.1. Sensitivity experiment using NW-150Tg over select regions in CESM-WACCM4. Date of initial perturbation is 15 May for all tests.

Name	**Region**	**Mechanism Isolated**
EXP-MC	Maritime Continent: 95°E-140°E, 15°S-15°N	Suppressed convection from surface cooling of the Maritime Continent and zonal equatorial Pacific zonal temperature gradient.
EXP-TA	Tropical Africa: 15°E-50°W, 10°S-30°N	Eastward propagating Kelvin wave produced by reduced African convective activity.
EXP-NH	Northern Hemisphere: North of 10°N	Equatorward shift of the ITCZ and weakening of North Pacific subtropical high pressure.

Figures

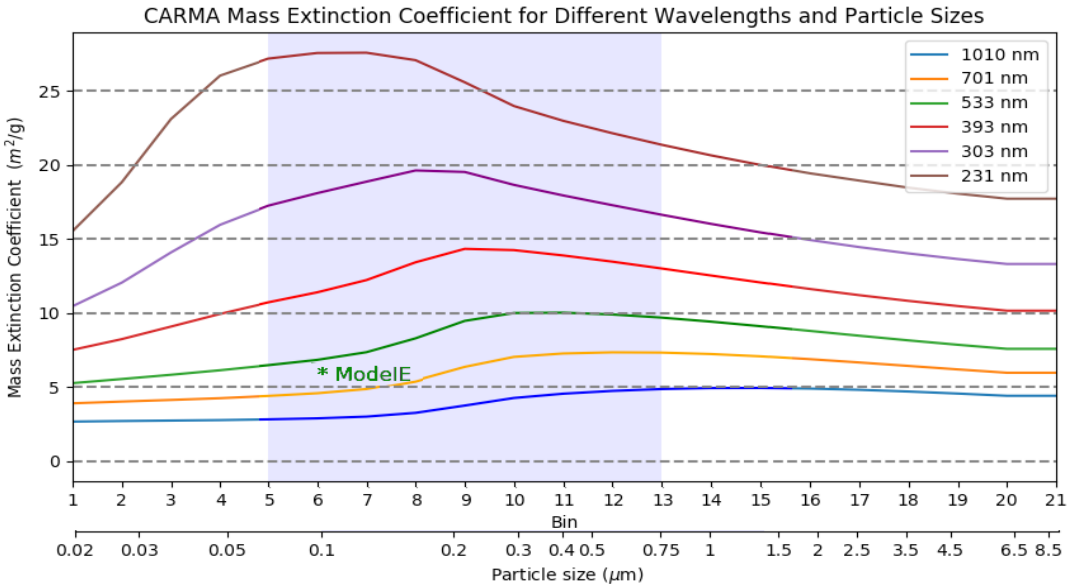

Figure 2.1. Mass extinction coefficient (m²/g) for 21 particle sizes (effective radius for fractal particles in WACCM4-CARMA, radius for spherical particles in ModelE) across five wavelengths (centered around the visible light band). ModelE assumed a mass extinction coefficient of 5.5 m²/g with particles at a constant size of 0.1 µm. The light grey shading represents the size distribution of 95% of the black carbon in WACCM4 on day 1, where the mean effective radius is initially 0.11 µm and the variance is 1.6 µm. This figure was published as Figure 5 in Coupe et al. [2019].

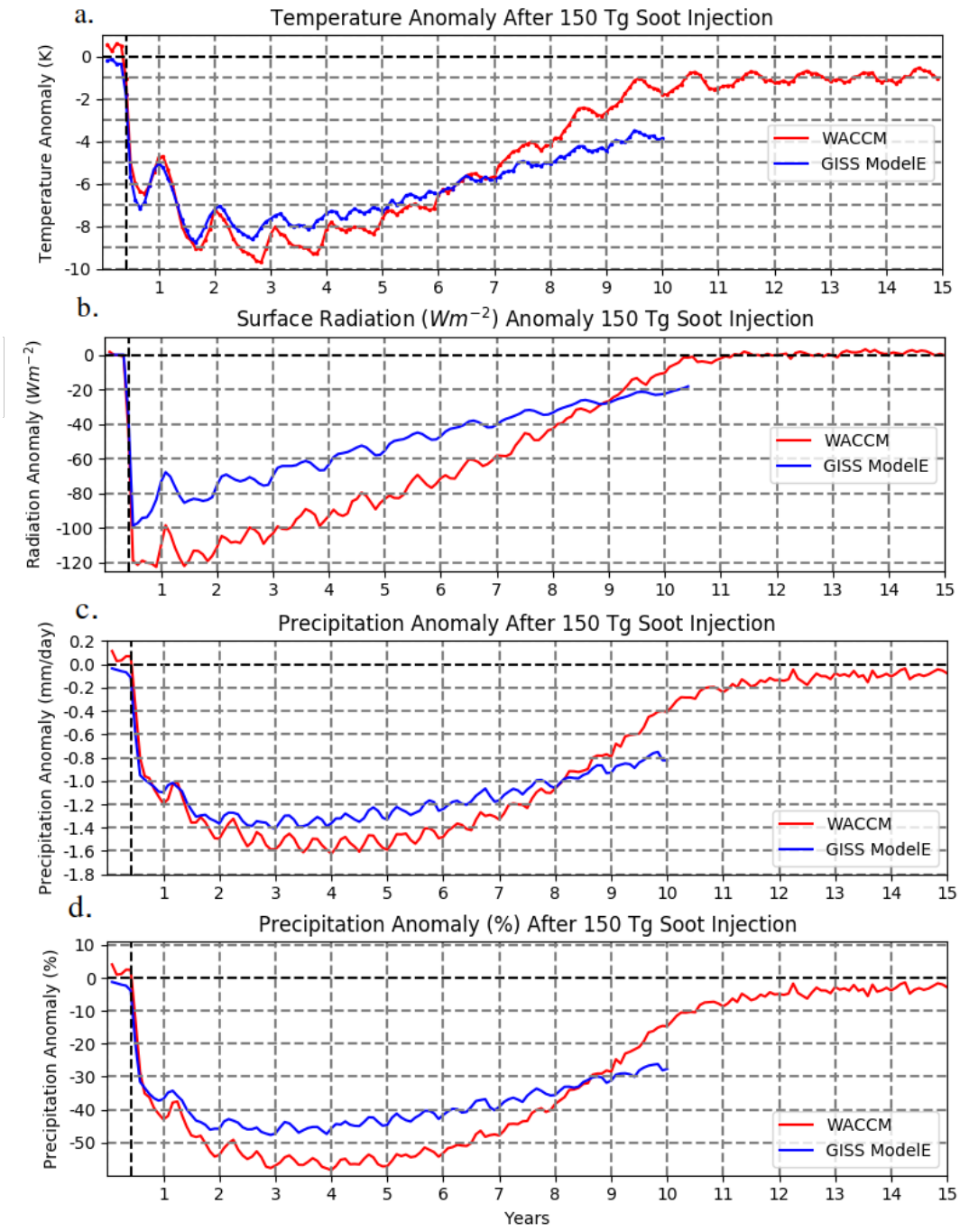

Figure 2.2. CESM-WACCM4 and ModelE monthly global mean (a) surface temperature anomaly (°C), (b) surface radiation anomaly (W m^{-2}), (c) precipitation anomaly (mm/day), and (d) precipitation anomaly as a fraction of the control following the injection of 150 Tg of black carbon into the upper troposphere and lower stratosphere. Part of this figure was published in Coupe et al. [2019] as Figure 7.

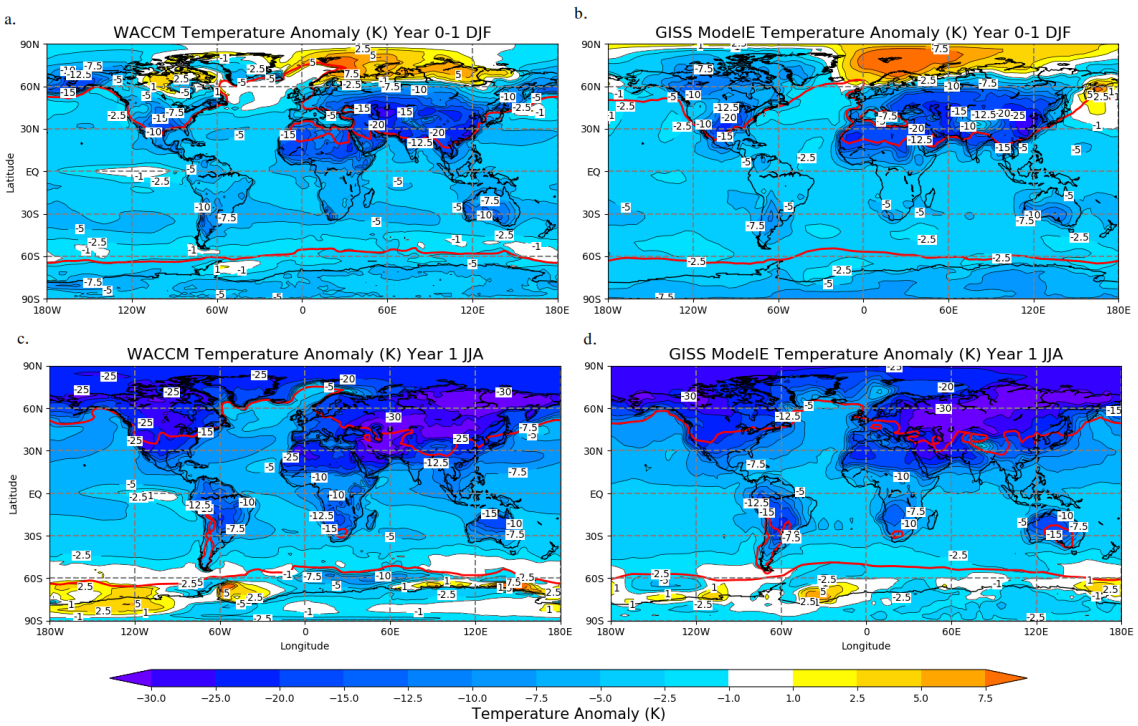

Figure 2.3. WACCM4 and ModelE temperature anomalies (°C) for DJF year 0-1 (a,b). JJA year 1 temperature anomalies for WACCM4 (c) and ModelE (d). Anomalies are calculated with respect to the control runs for each model. The red contour represents the latitude, poleward of which, the actual temperature is below 0°C. This figure was published as Figure 9 in Coupe et al. [2019].

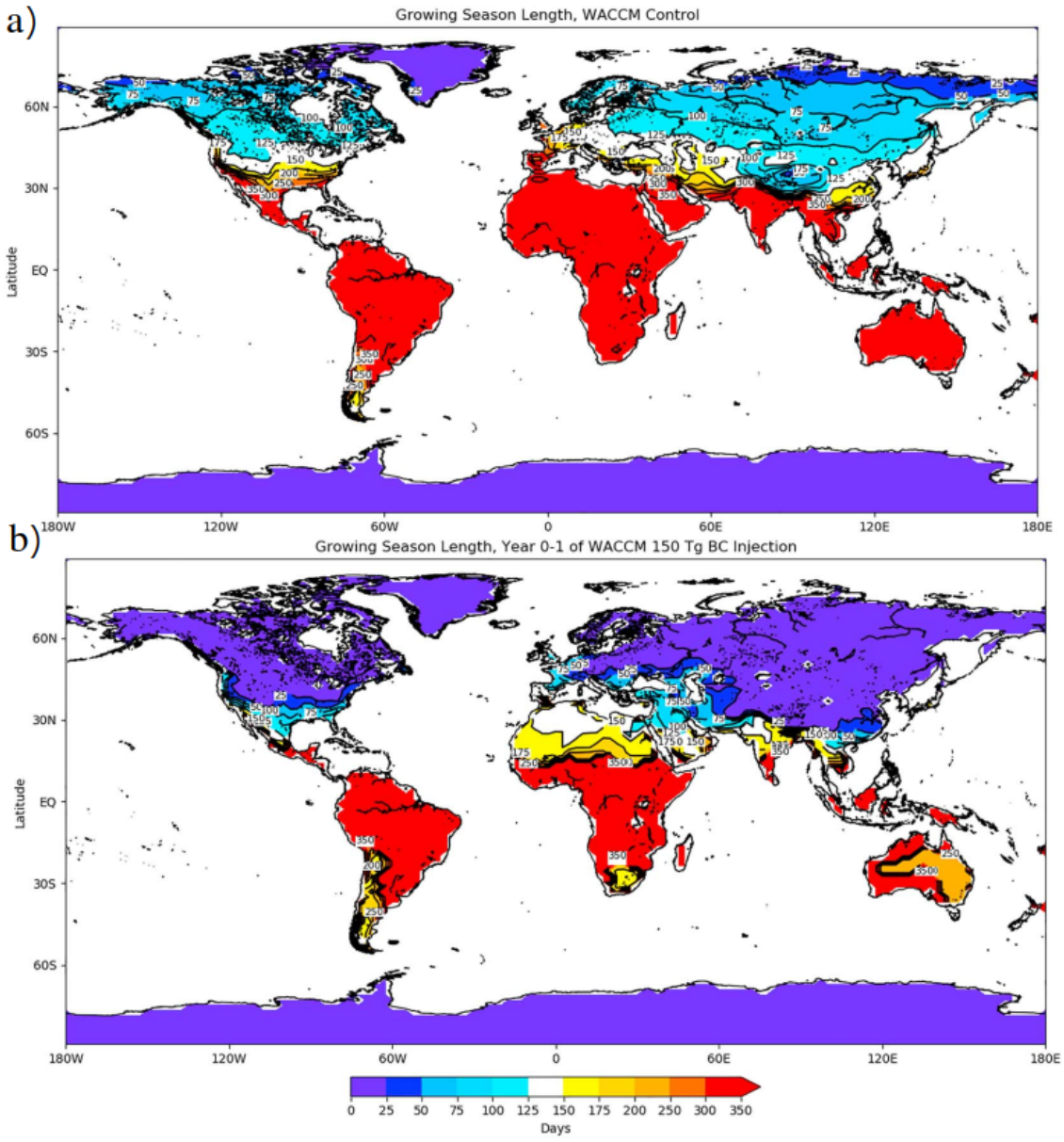

Figure 2.4. Average growing season length during the CESM-WACCM4 control run (a) and the growing season length during Year 1–2 of the CESM-WACCM4 150 Tg soot injection (b). For the Northern Hemisphere, this time period corresponds to 1 January, Year 1, to 31 December, Year 1, and in the Southern Hemisphere this corresponds to 1 July, Year 1, to 30 June, Year 2. This figure was published as Figure 10 in Coupe et al. [2019].

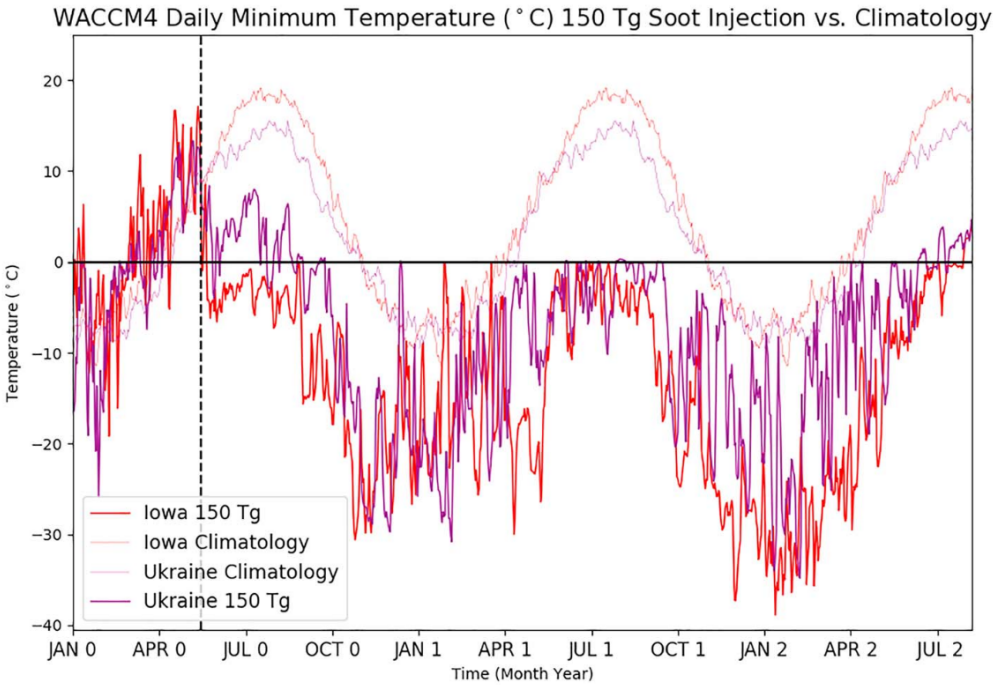

Figure 2.5. Time series of daily minimum temperature from WACCM4 with 150 Tg soot injection for Iowa (42°N, 95°W) and Ukraine (50°N, 30°E), as well as control run temperatures. The vertical dashed line is the time of soot injection. This figure was published as Figure 11 in Coupe et al. [2019].

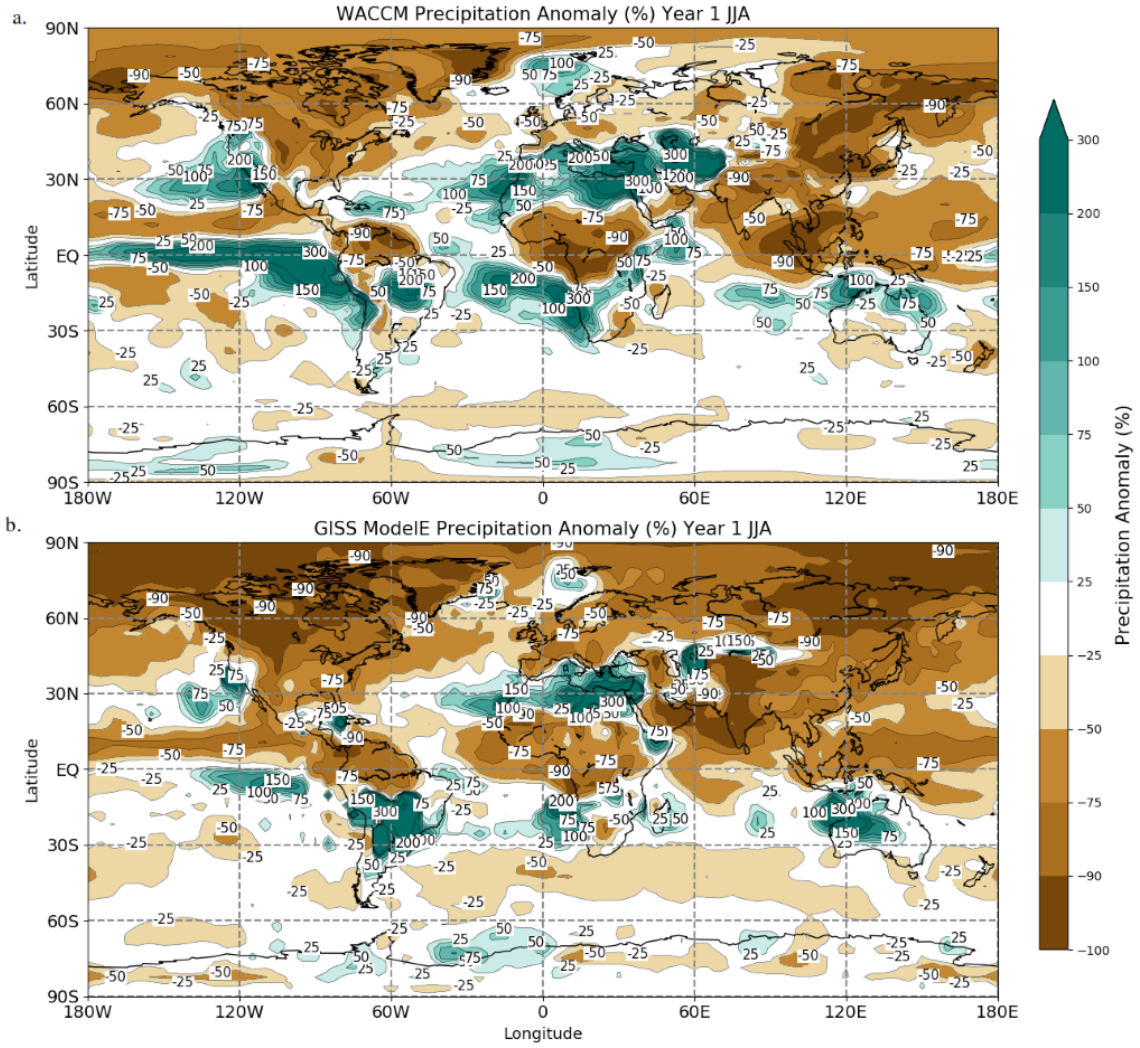

Figure 2.6. CESM-WACCM4 (top) and GISS ModelE (bottom) precipitation anomalies (% change) in JJA of year 1, starting with the second June after the May injection. This figure was published as Figure 12 in Coupe et al. [2019].

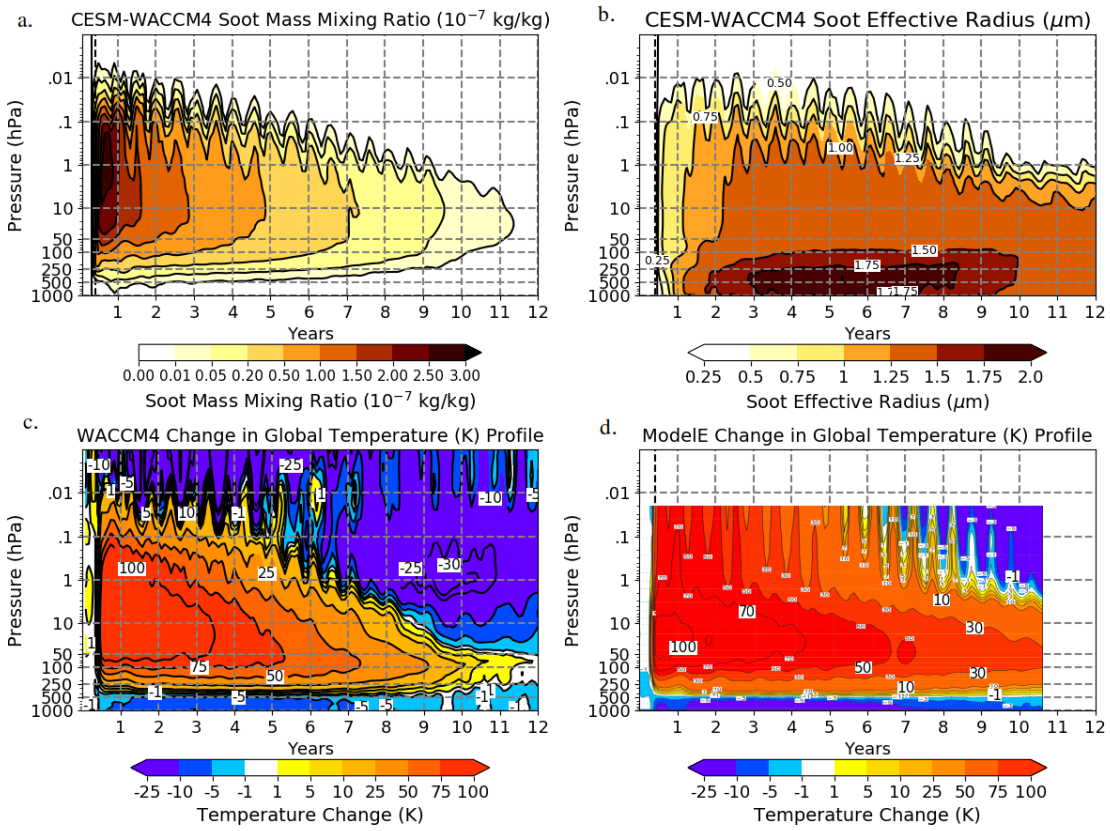

Figure 2.7. Globally averaged vertical profile of soot mass mixing ratio (10 kg/kg) after the 150 Tg soot injection on 15 May in Whole Atmosphere Community Climate Model version 4 (WACCM4; top left). Effective radius (μm. The e-m) of black carbon aerosols during the CESM WACCM4 150 Tg soot injection simulation (top right). Effective radius of black carbon in Goddard Institute for Space Studies (GISS) ModelE run was a constant 0.1 μm. The e-m. Temperature profile anomaly following the black carbon injection in WACCM4 (bottom left) and GISS ModelE (bottom right). Extreme heating is observed in the upper troposphere and stratosphere in both models. GISS ModelE figure is from Robock et al. [2007] and this figure was also published as Figure 2 in Coupe et al. [2019].

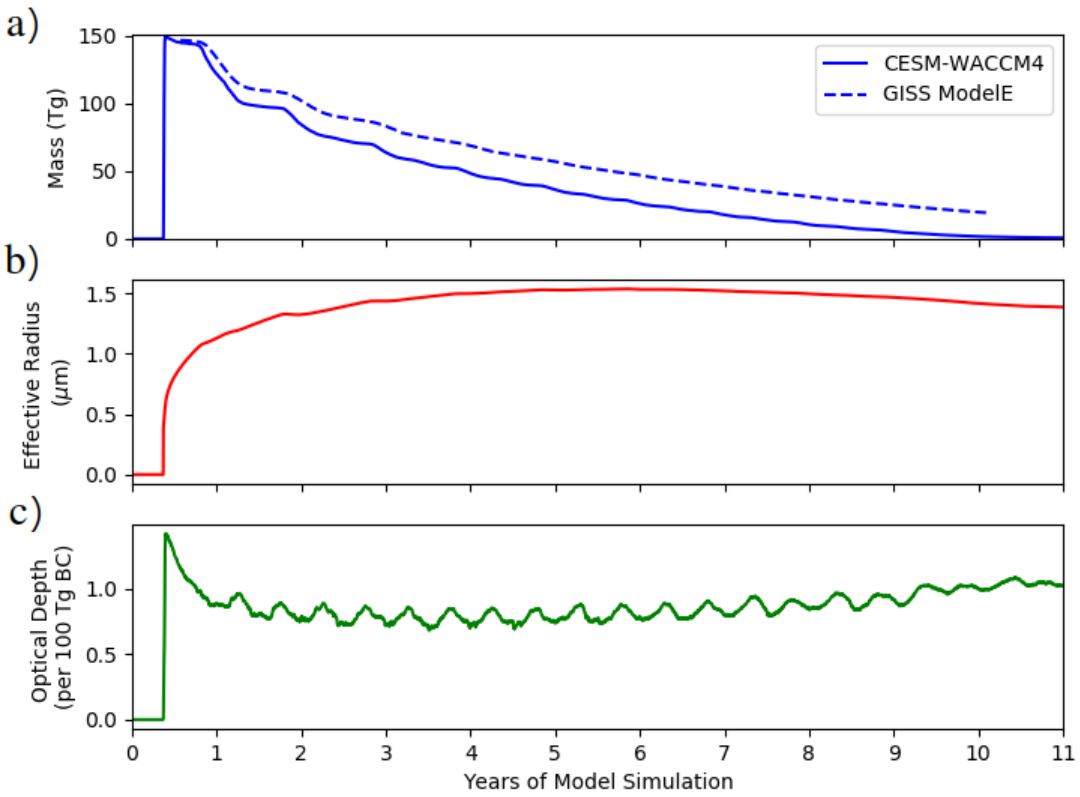

Figure 2.8. Daily timeseries of (a) total column mass of black carbon aerosols globally, (b) mass-weighted globally averaged effective radius of fractal aerosols, and (c) optical depth of black carbon aerosols per unit mass averaged globally for NW-150Tg.

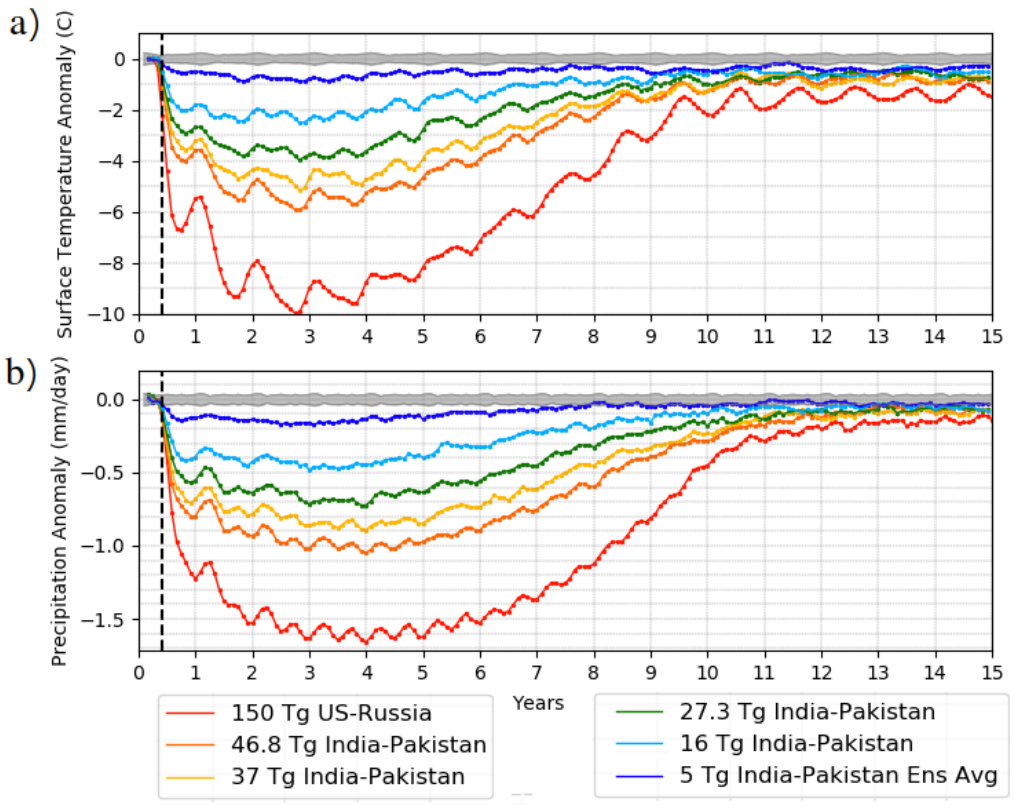

Figure 2.9. Monthly (a) surface temperature anomaly (°C) and (b) precipitation anomaly (mm/day) for all nuclear war scenario simulations in CESM-WACCM4. Grey shading represents two standard deviations above and below the mean.

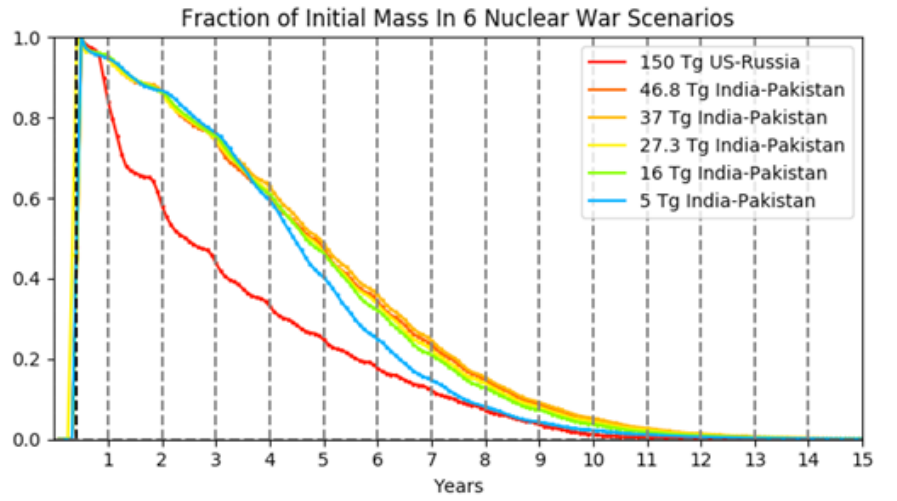

Figure 2.10. Fraction of initial mass of black carbon for six nuclear war scenarios through time.

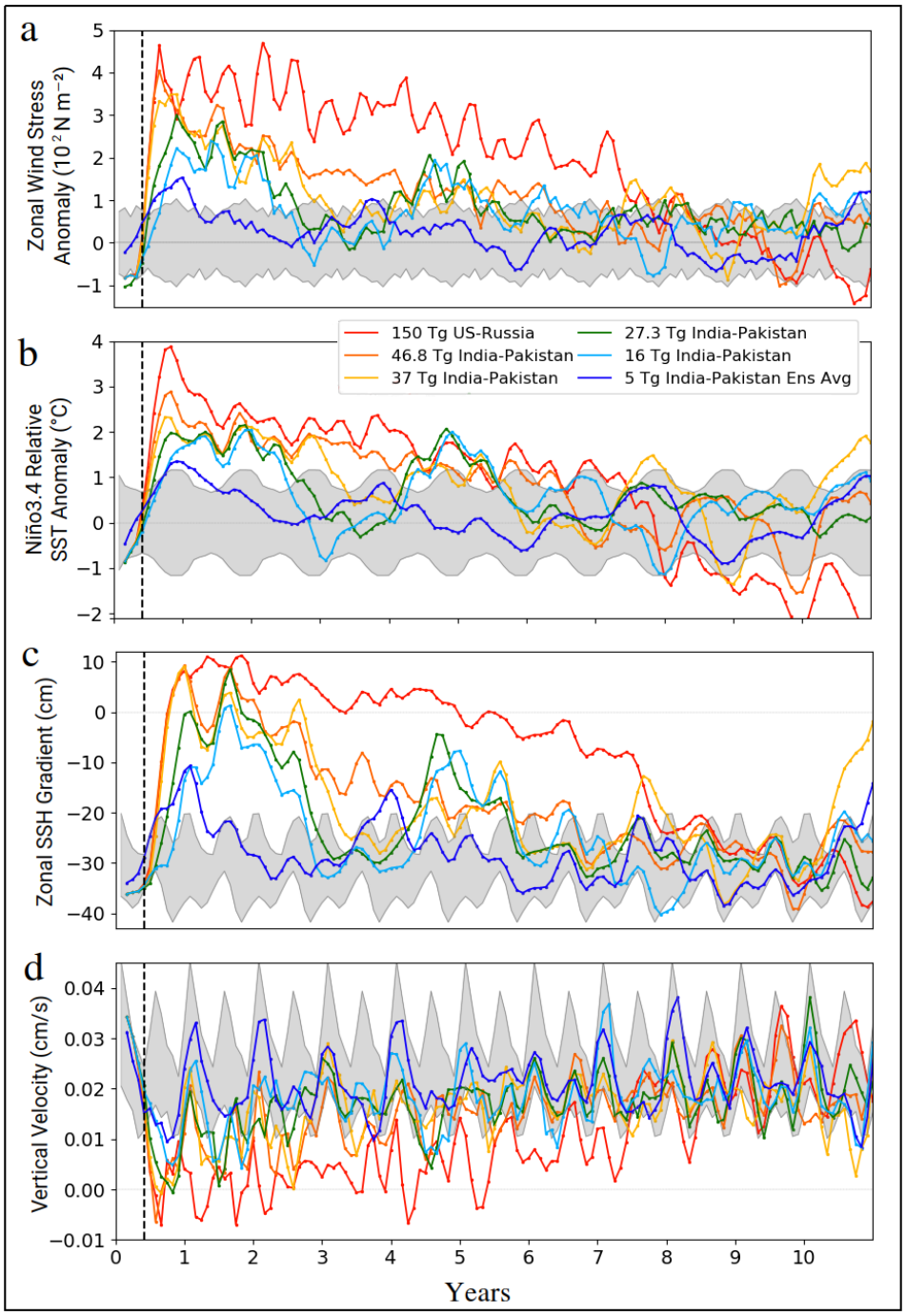

Figure 3.1. 3-month running mean of the (a) equatorial Pacific Ocean zonal wind stress anomaly (130°E-120°W, 5°S-5°N) (10^2 Nm^{-2}), (b) Niño3.4 region relative SST anomalies (5°N-5°S, 170°W-120°W), (c) zonal sea surface height difference between tropical (5°S-5°N) east (150°W-90°W) and west Pacific (140°E-170°W) (cm), (d) vertical velocity in the top 100 m layer of the equatorial Pacific (5°S-5°N, 180°W-90°W) for all nuclear war scenarios as simulated in CESM-WACCM4. Grey shading indicates ±1 standard deviation from the model climatological mean. This figure is Figure 1 in Coupe et al. [2020].

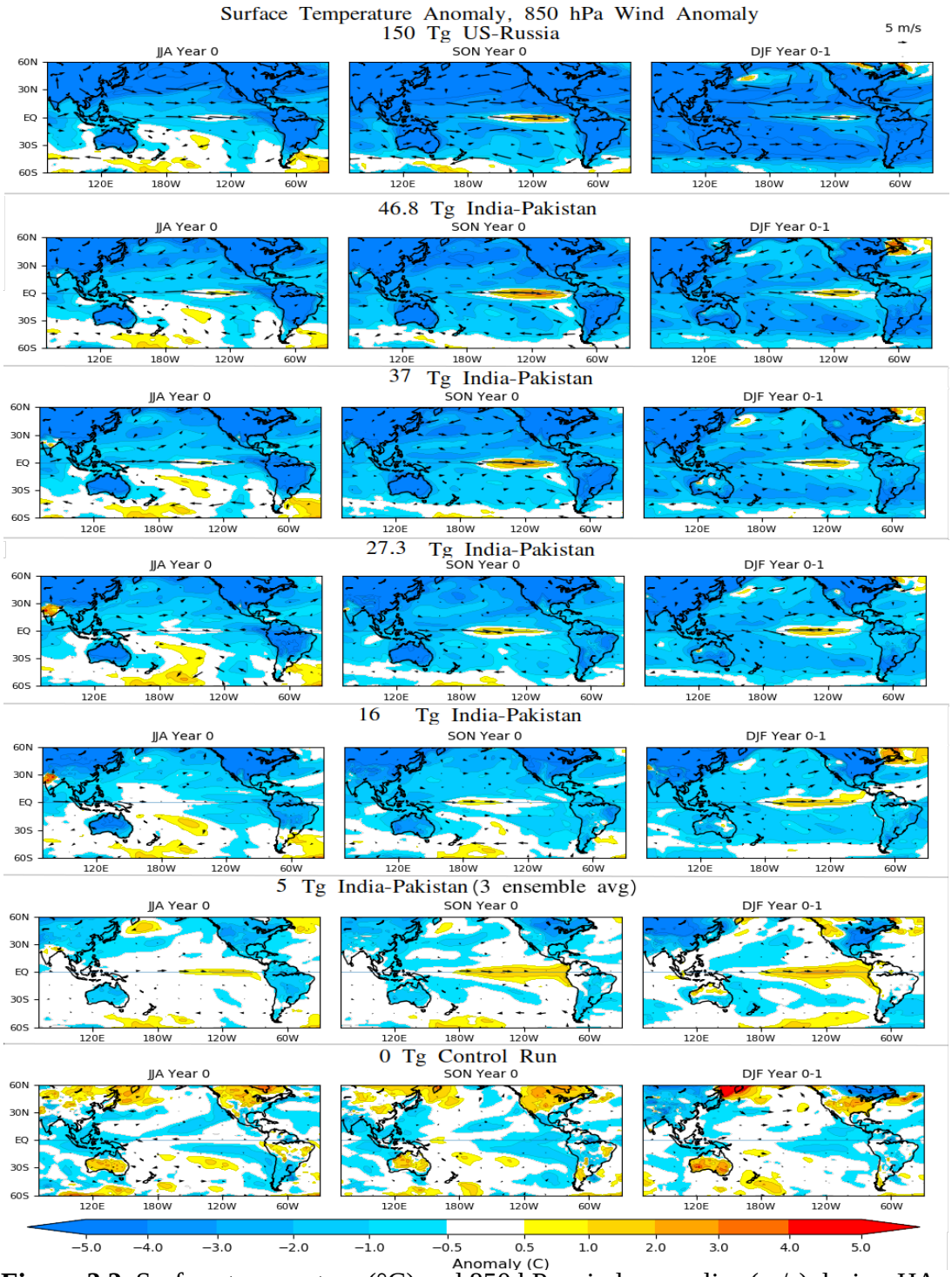

Figure 3.2. Surface temperature (°C) and 850 hPa wind anomalies (m/s) during JJA, SON, and DJF for all nuclear war scenarios.

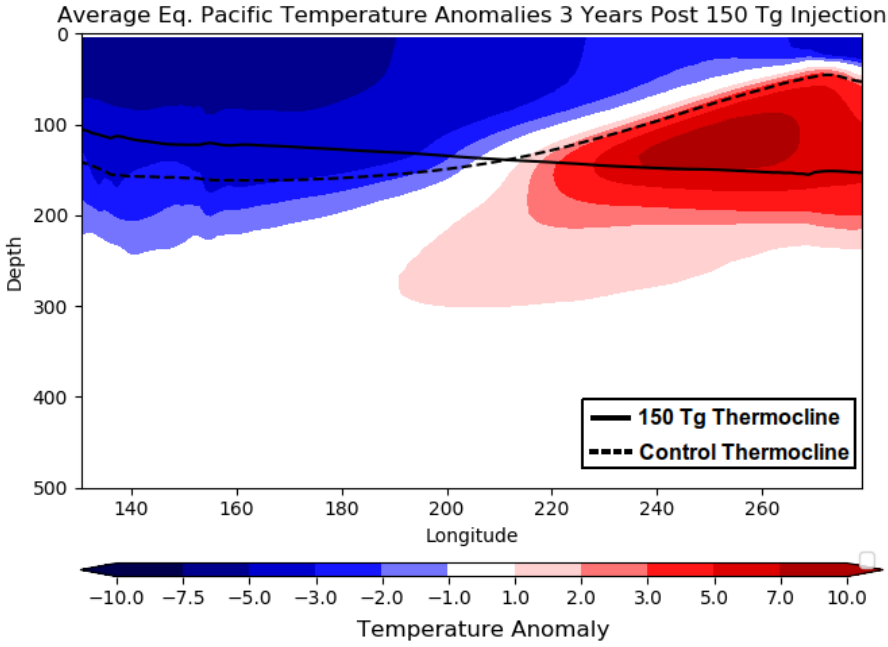

Figure 3.3. Equatorial Pacific (5°S to 5°N) temperature anomalies (°C) with depth averaged over the 3 years after the injection of 150 Tg of black carbon. Average thermocline for the control and nuclear conflict simulation is represented as the 20°C isotherm during those simulations.

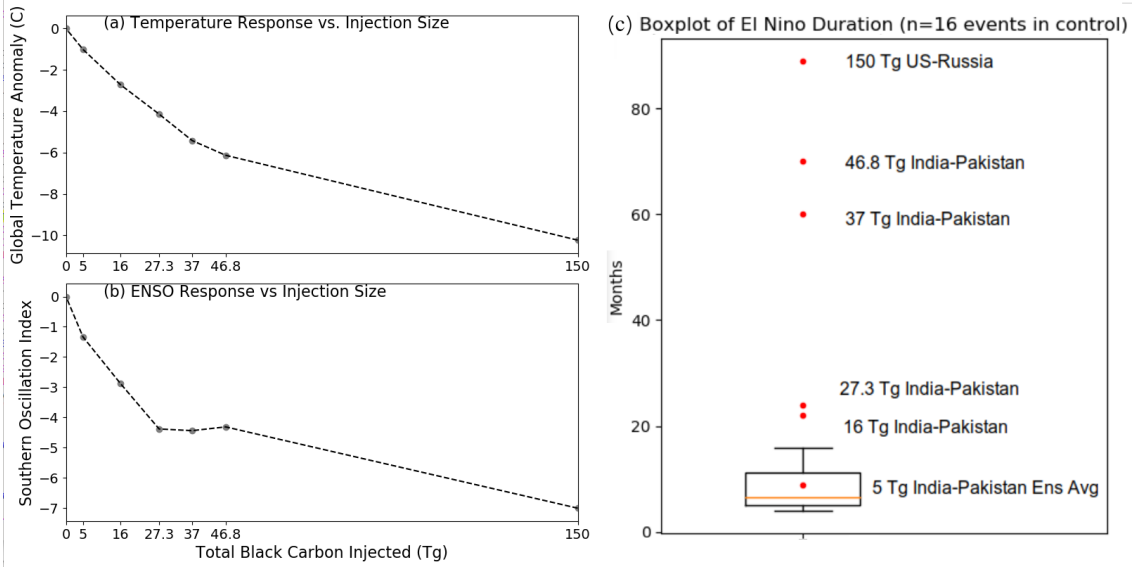

Figure 3.4. (a) Relationship between total black carbon injected and the global mean temperature response within 2 years of injection. (b) Relationship between total black carbon injected and the maximum response in the Southern Oscillation Index within 2 years of the injection. (c) Box plot of El Niño event duration in months for the control run (n = 16 events over 720 months). Each red dot represents the duration for the different nuclear war cases. The 5 Tg case is the only case where the El Niño is not statistically significant from the control.

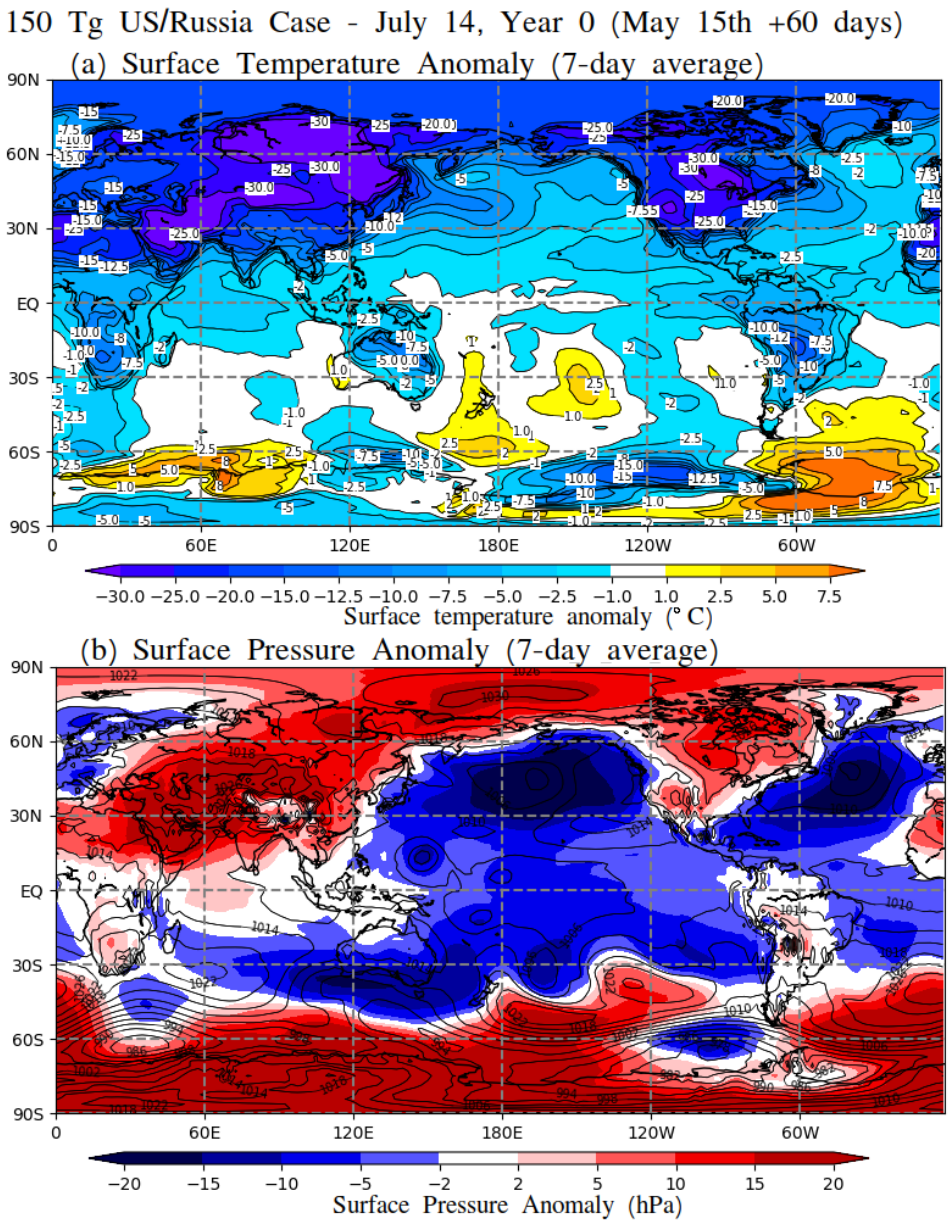

Figure 3.5. (a) Surface temperature anomaly (7-day average) centered on July 14th, 60 days after the start of the 150 Tg black carbon injection. (b) Mean sea level pressure anomaly and surface wind anomalies over the same time frame.

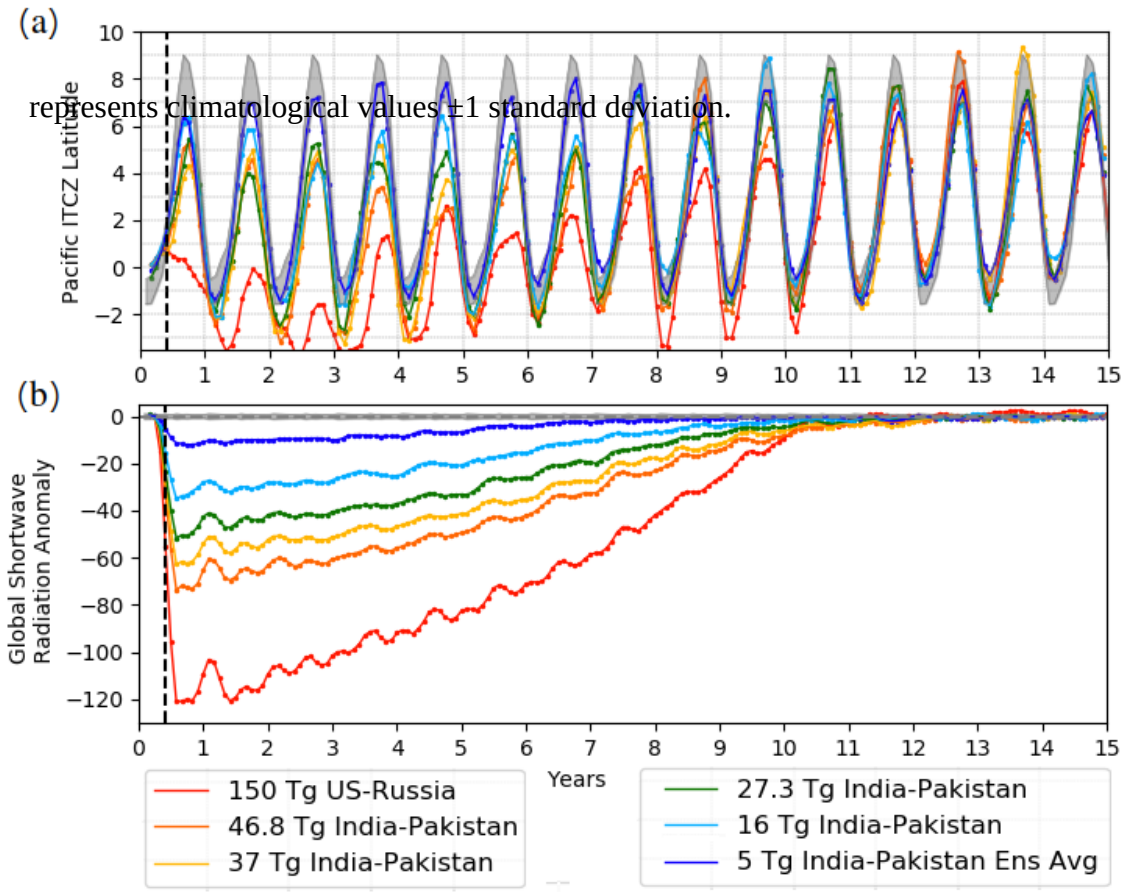

represents climatological values ±1 standard deviation.

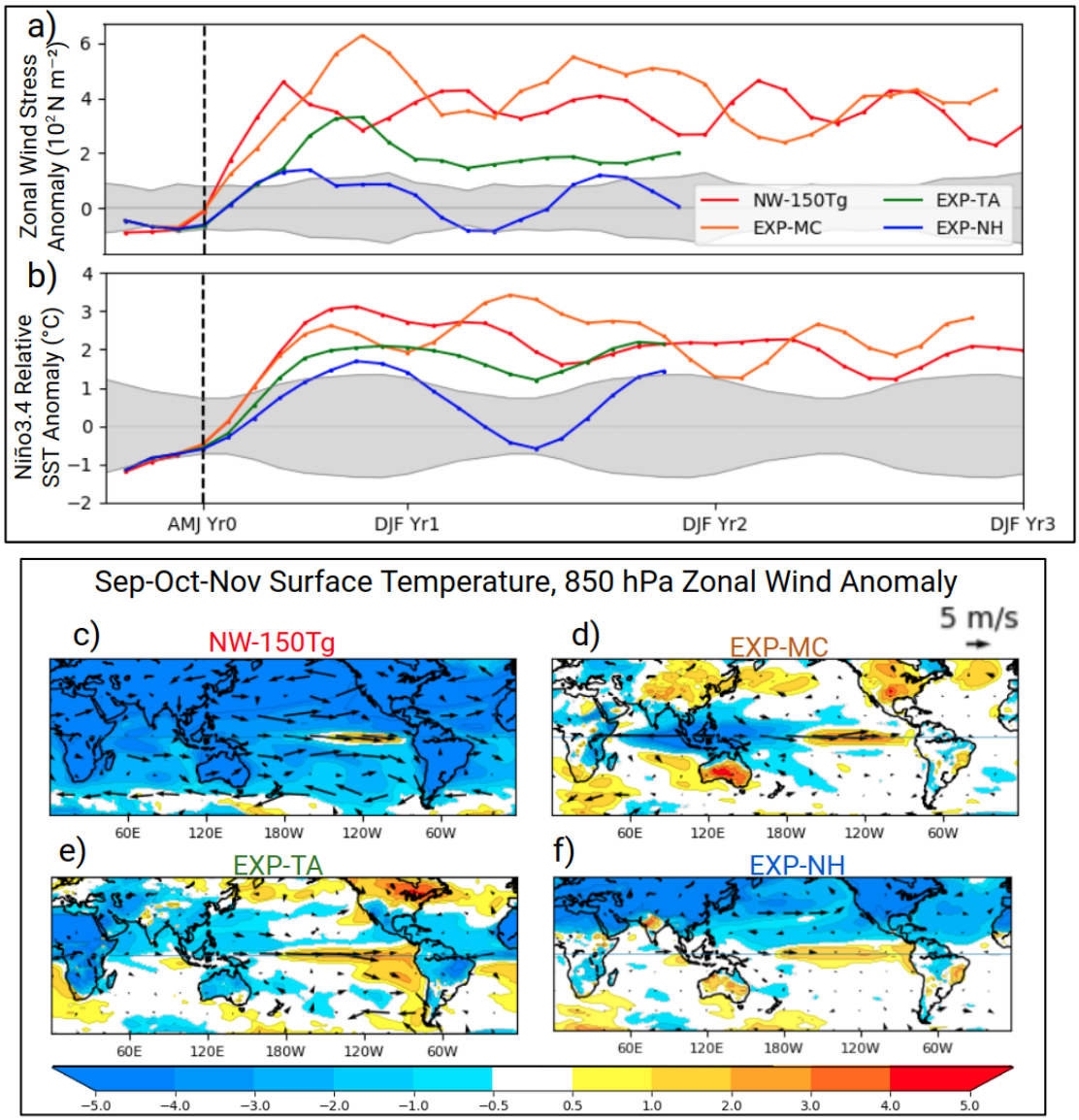

Figure 3.7. 3-month running mean of the (a) equatorial Pacific Ocean zonal surface wind stress anomaly (130°E-120°W, 5°S-5°N) (10^2 Nm^{-2}) and (b) Niño3.4 region relative SST anomalies (5°N-5°S, 170°W-120°W) for three sensitivity tests using CESM-WACCM4. Grey shading indicates ±1 standard deviation from the model climatological mean. (c-f) Surface temperature (°C, color fill) and 850 hPa wind (m/s, arrows) anomalies during September-October-November of the first year for all sensitivity tests. See Table 2 for description of the experiments.

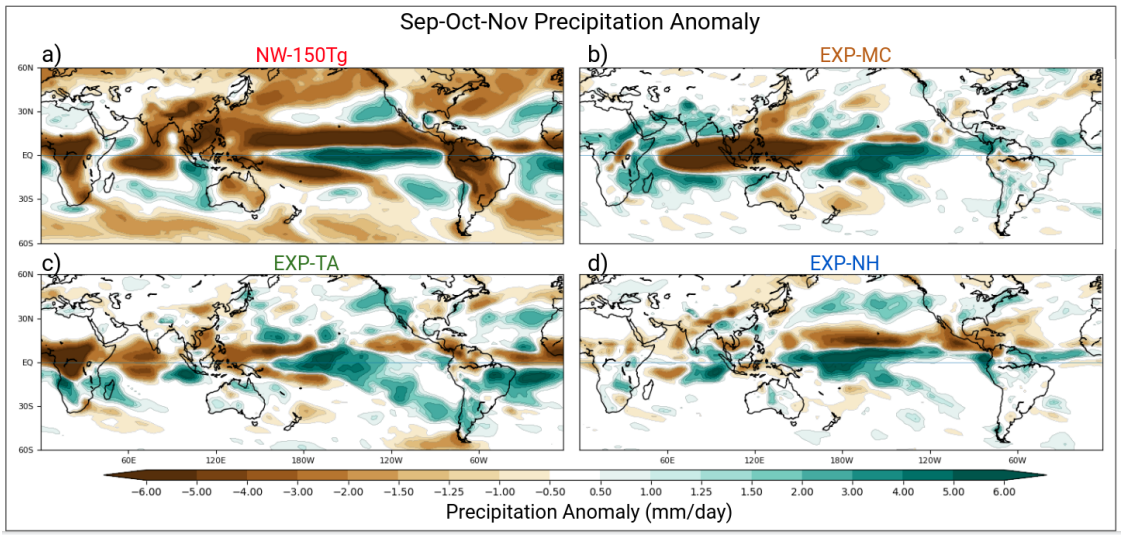

Figure 3.8. Precipitation anomalies (mm/day) in (a) NW-150Tg, (b) EXP-MC, (c) EXP-TA, (d) EXP-NH during September-October-November of the first year of the perturbation.

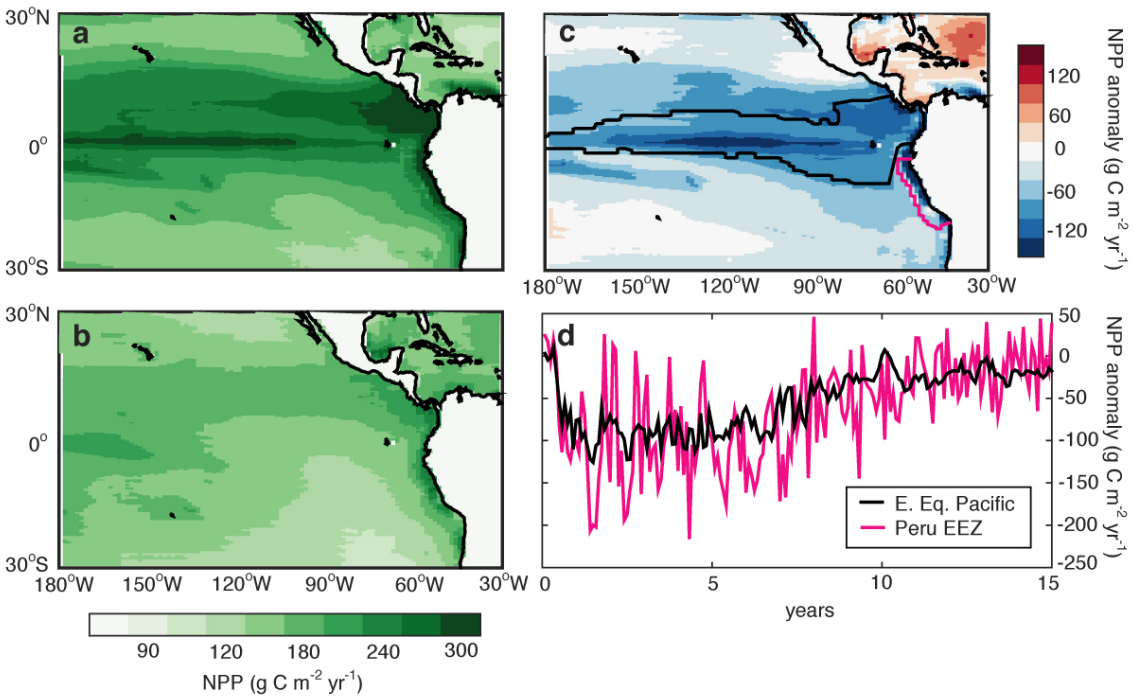

Figure 3.9. Average annual-mean phytoplankton net primary production (NPP, g C m^{-2} yr^{-1}) integrated over the top 150 m of the water column 2-5 years post-conflict for (a) the control ensemble mean and (b) the 150 Tg simulation. (c) Anomaly in NPP, as indicated by the difference between NPP in the 150 Tg simulation and the NPP from the control ensemble mean. (d) Temporal evolution of the NPP anomalies averaged over the Eastern Equatorial Pacific biome and Peru Exclusive Economic Zone (black/purple contours in panel c) post-conflict. Anomalies defined as in panel c. This figure was created by Nicole Lovenduski and will be published as a figure in Coupe et al. [2020].

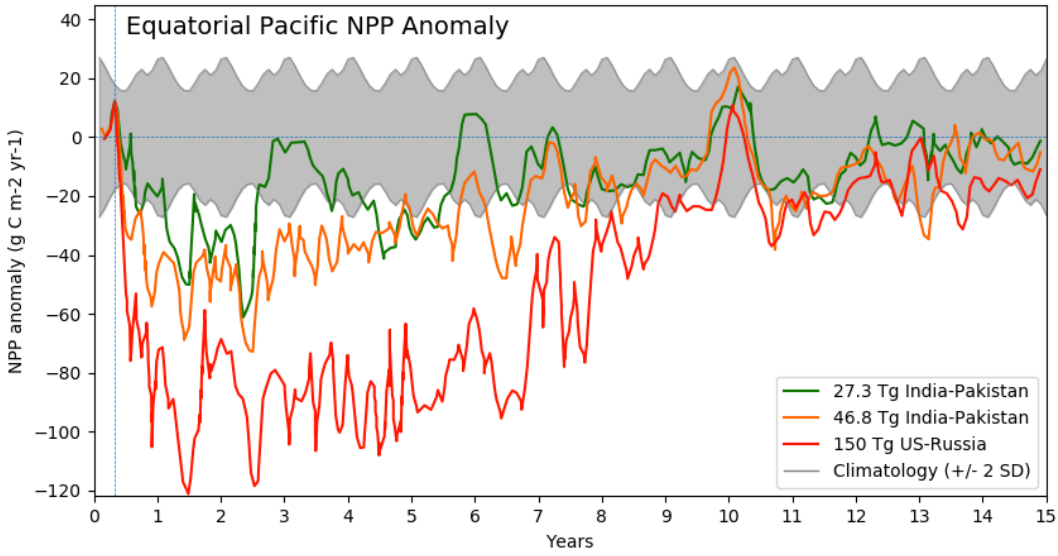

Figure 3.10. Net Primary Production (NPP) changes in the equatorial Pacific for additional nuclear war scenarios. Gray shading represents climatological values ±2 standard deviations.

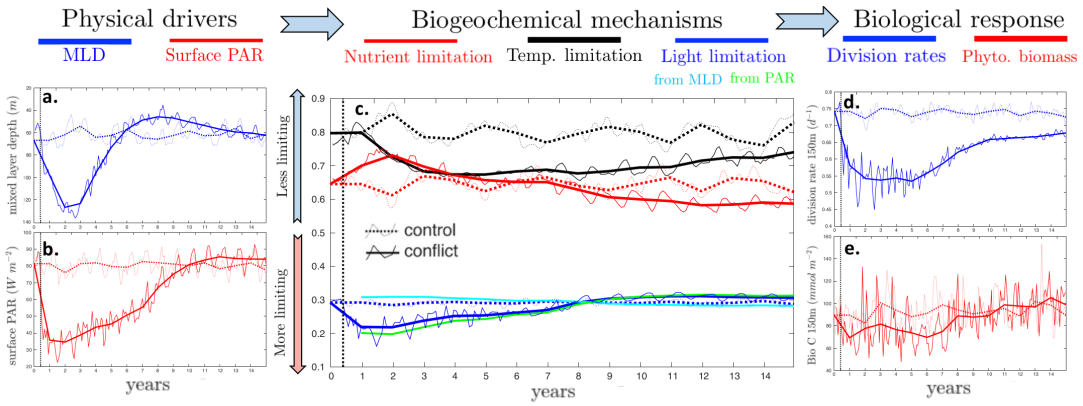

Figure 3.11. Time series for the physical drivers (left; **a**, **b**), biogeochemical mechanisms (middle; **c**), and biological response (right; **d**, **e**) for the control (dashed) and nuclear winter (solid) runs are plotted for the Eastern Equatorial Pacific biome (black contour in Fig. 3c). Nutrient (red), temperature (black), and light limitation (blue) terms represent the biomass-weighted averaged of all phytoplankton in the top 150 m of the water column. Light limitation is partitioned into the approximate effect of deeper mixed layer depths (teal) and reduced PAR (green). The effect of deeper mixing on population averaged light limitation (teal) is approximated by placing the phytoplankton population from the conflict run, which is subjected to deeper mixing, into the light field from the control run. The effect of reduced PAR on population averaged light limitation (green) is approximated by placing the phytoplankton population from the control run into the light field from the conflict run, which is lower due reduced incoming surface radiation. Biomass (blue) and Net Primary Production (red) are integrated over the top 150 m of the water column. The annually averaged time series is overlaid with a thicker line on top of the monthly averaged time series. A vertical dashed line denotes when the bomb was detonated. This figure was created by Tyler Rohr and will be published as part of Coupe et al. [2020].

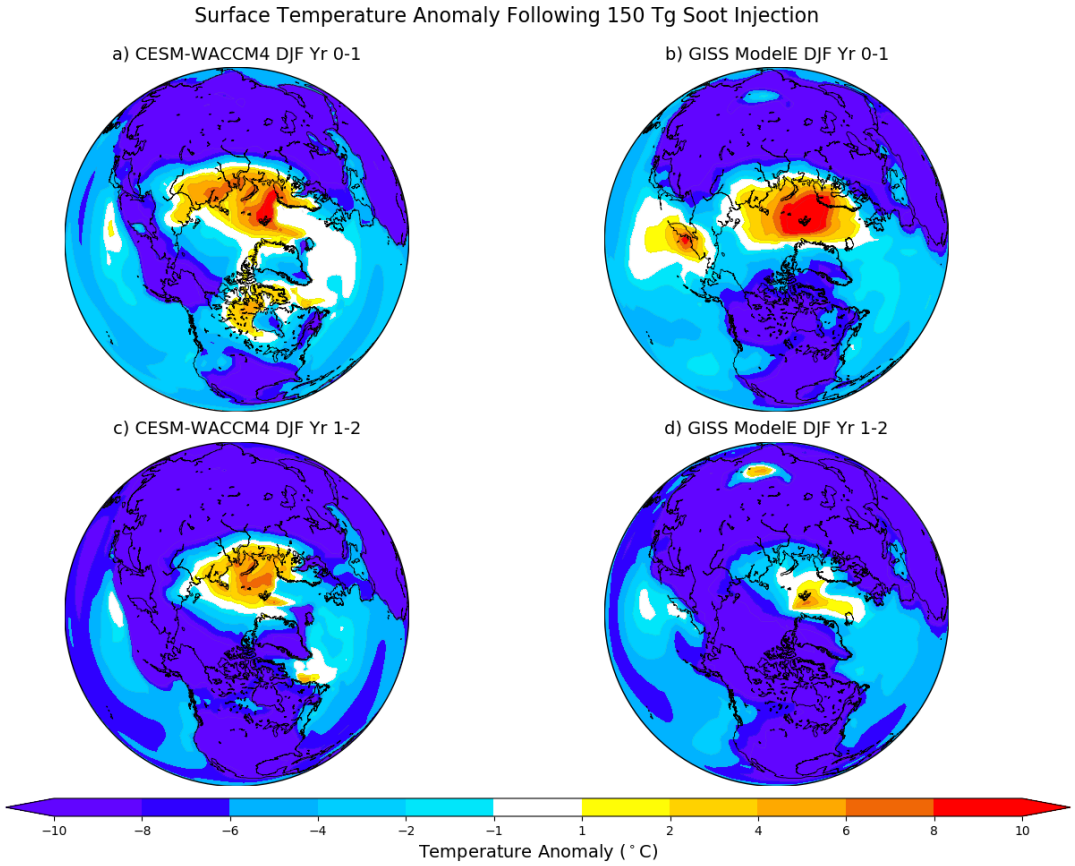

Figure 4.1. Surface temperature anomalies during DJF Year 0-1 in the 150 Tg United States and Russia nuclear war scenario with (a) GISS ModelE and (b) CESM-WACCM4 nuclear war simulations.

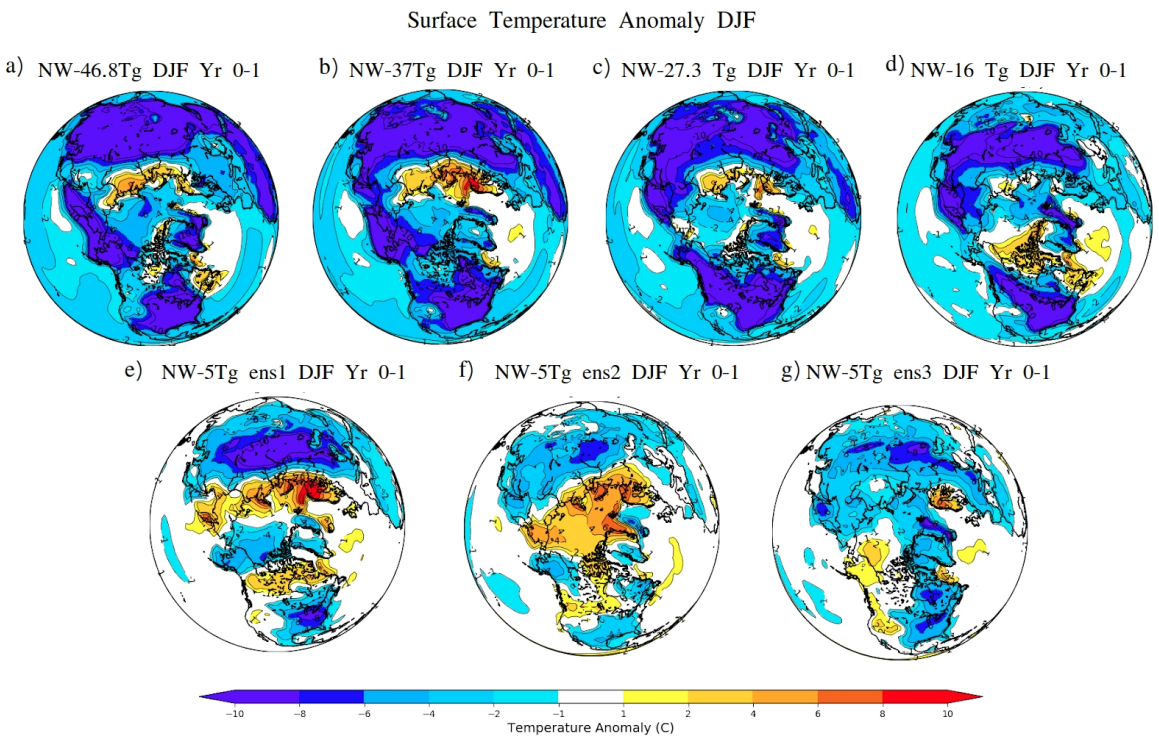

Figure 4.2. Surface temperature anomalies during DJF Year 0-1 in the India and Pakistan nuclear war simulations with (a) 46.8 Tg, (b) 37 Tg, (c) 27.3 Tg, (d) 16 Tg, (e-g) three ensembles with 5 Tg of soot aerosols injected into the upper troposphere and lower stratosphere.

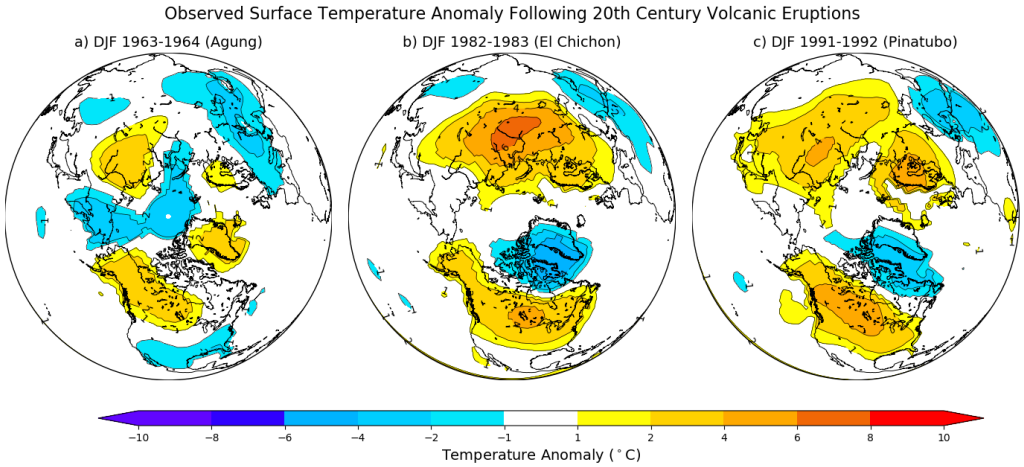

Figure 4.3. GISTEMP version 4 observed surface temperature anomalies during first DJF after the (a) 1963 Agung, (b) 1982 El Chichón, and (c) 1991 Pinatubo volcanic eruptions.

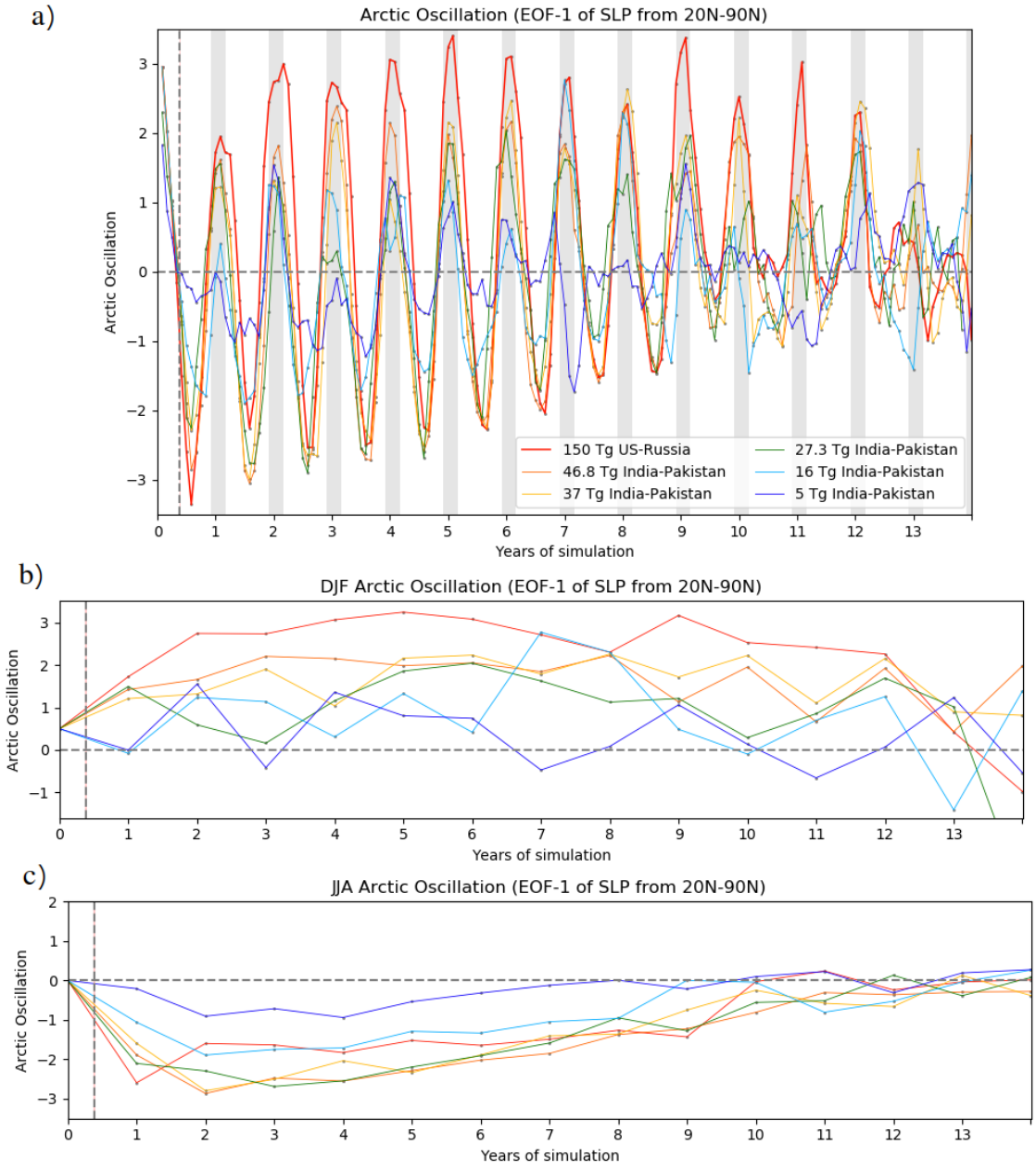

Figure 4.4. Time series of the Arctic Oscillation for all nuclear war simulations for (a) all months, (b) DJF, and (c) JJA.

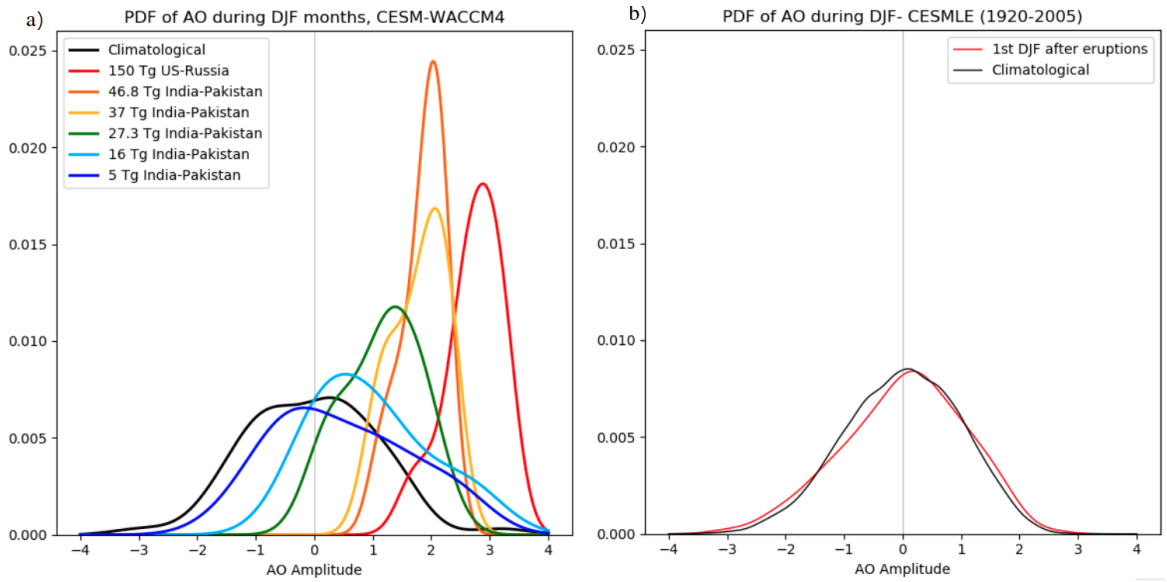

Figure 4.5. Probability density function for the Arctic Oscillation during (a) DJF months for the control run and all nuclear war simulations and (b) the first DJF after the volcanic eruptions of Agung (1963), El Chichón (1982), and Pinatubo (1991) in the CESM Large Ensemble.

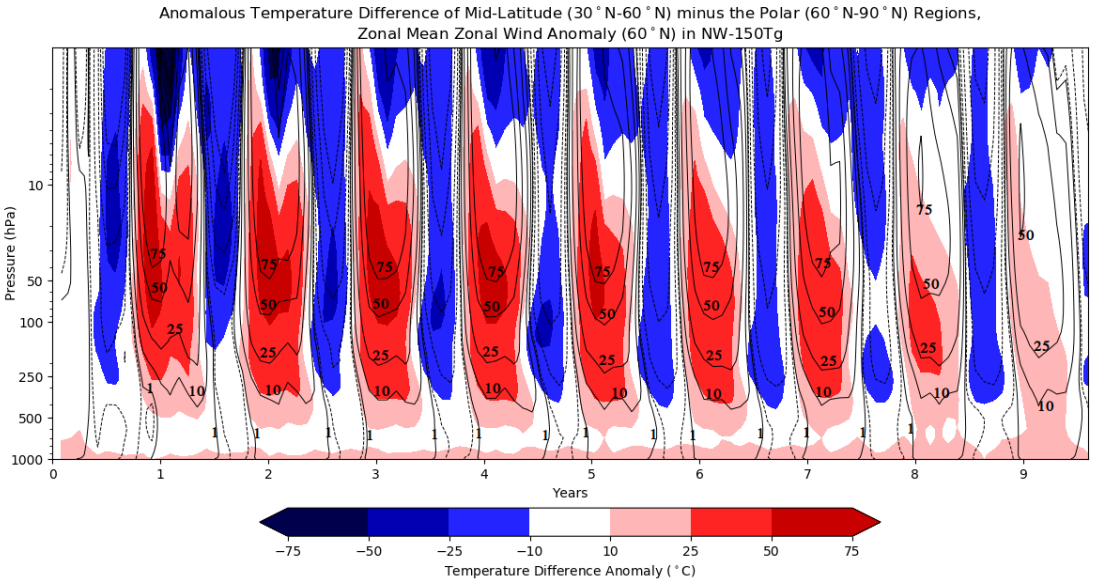

Figure 4.6. Anomaly of temperature difference (°C) of mid-latitude (30°N-60°N) minus the polar regions (60°N-90°N) (°C, color fill); zonal mean zonal wind anomaly at 60°N (m/s, contours) for NW-150Tg.

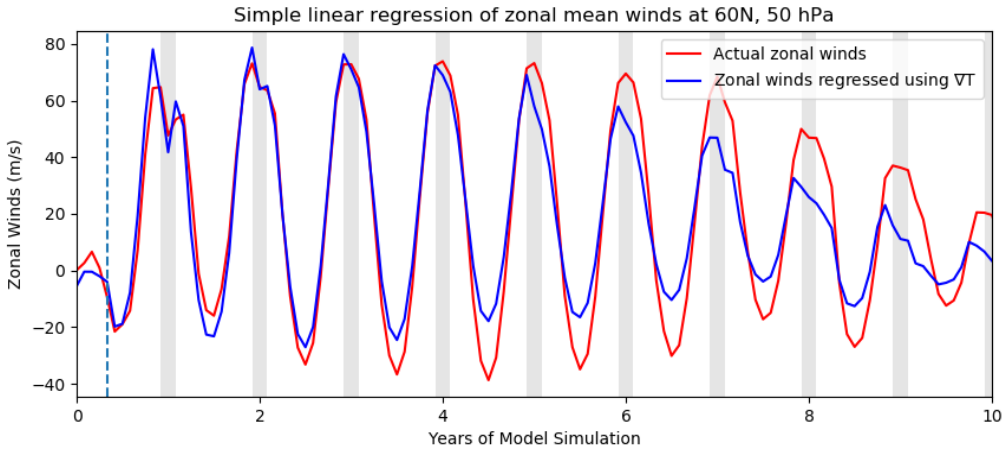

Figure 4.7. Simple linear regression of ∇T_{50hPa} onto zonal mean zonal winds at 60°N and 50 hPa. The ∇T_{50hPa} from NW-150Tg is used to predict the zonal mean zonal winds that are simulated. Grey vertical shading represents DJF of each year following the injection.

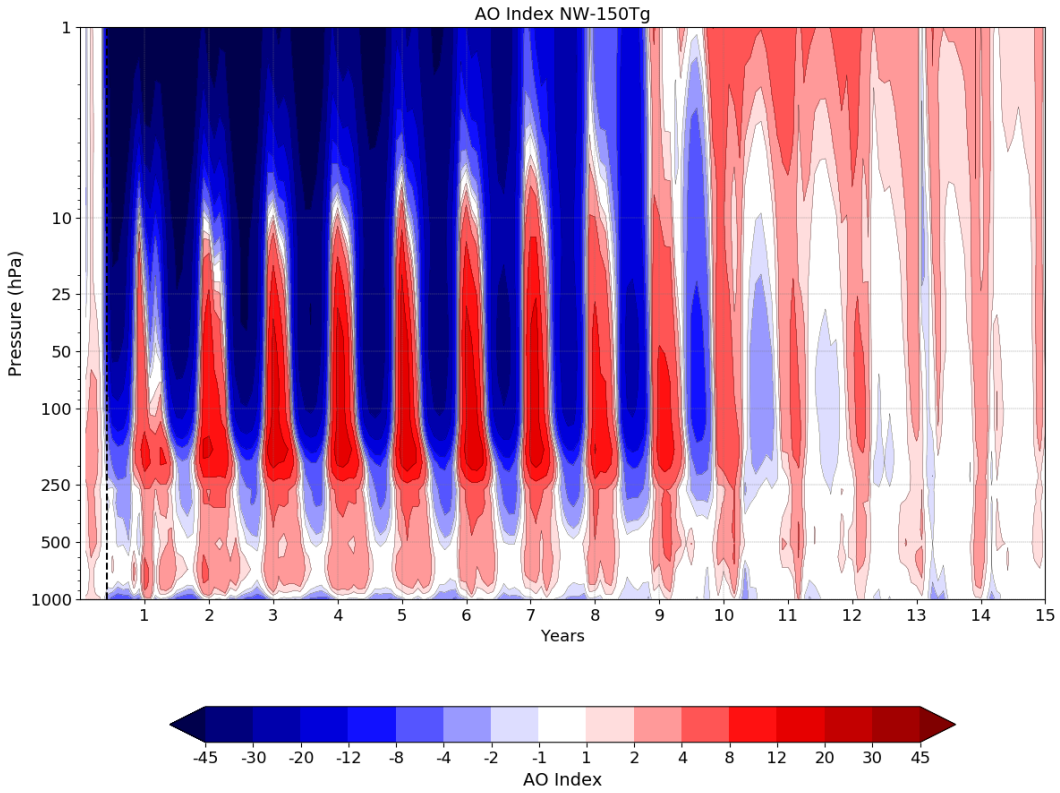

Figure 4.8. Arctic Oscillation as a function of height and time for NW-150Tg.

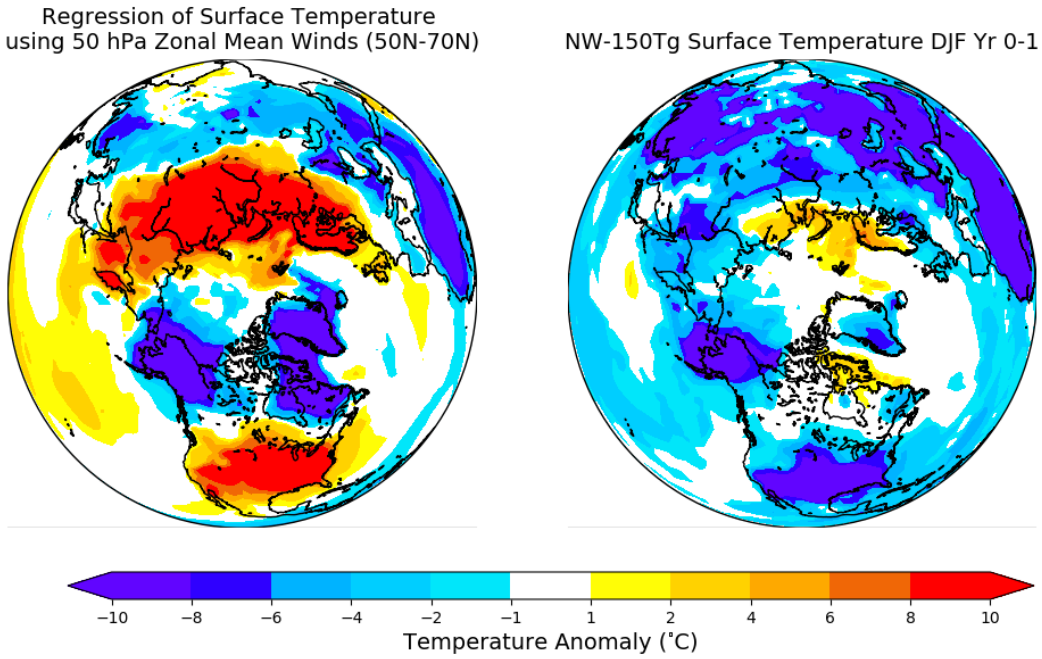

Figure 4.9. (a) Regression of expected DJF Year 0-1 surface temperature anomaly using 50 hPa zonal mean winds (50°N-70°N) in NW-150Tg. (b) Actual surface temperature anomaly during DJF of Year 0-1 in NW-150Tg.

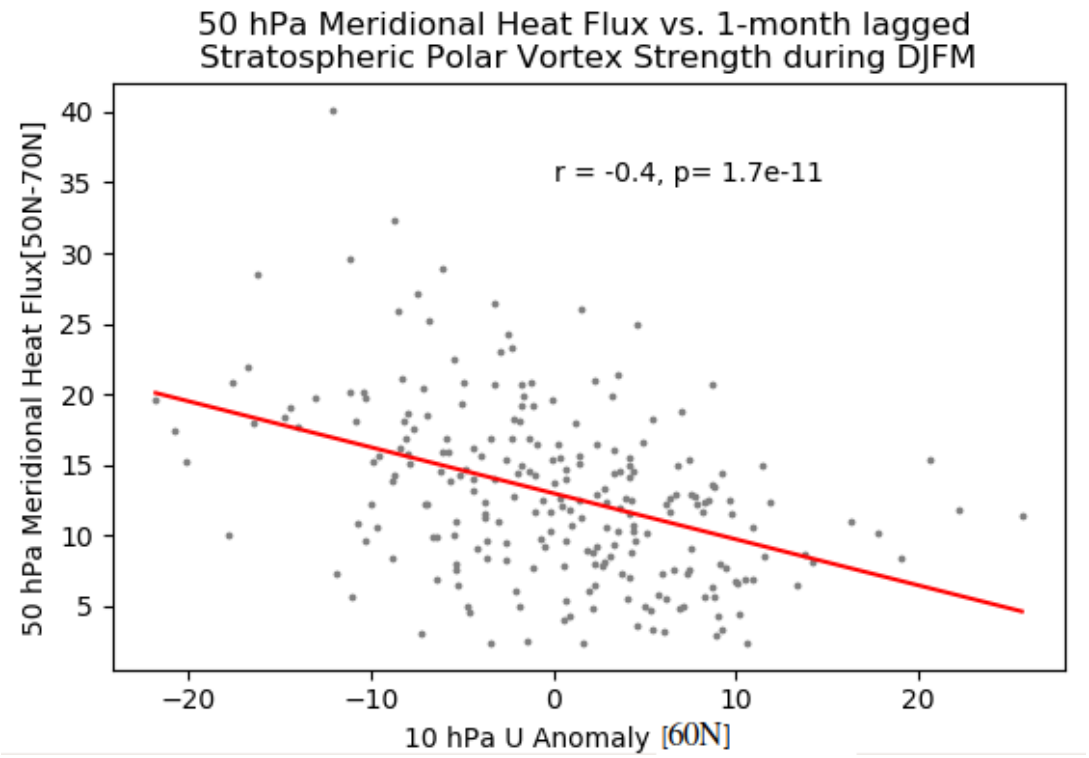

Figure 4.10. Scatterplot of 50 hPa meridional heat flux (50°N-70°N) as a function of 10 hPa zonal mean zonal winds (60°N).

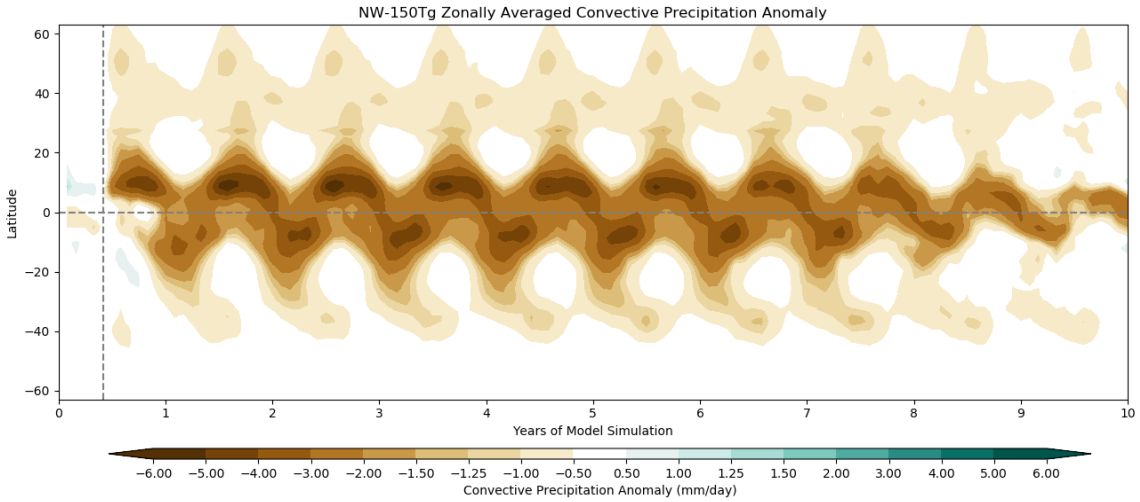

Figure 4.11. Zonally averaged convective precipitation anomaly in NW-150Tg as a function of latitude and time.

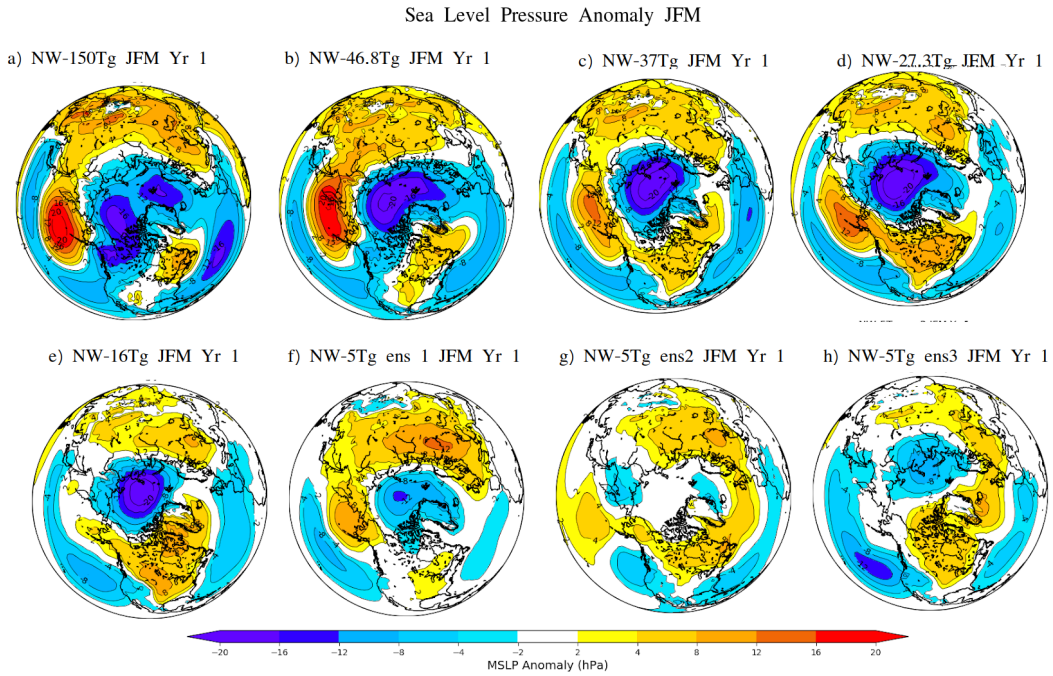

Figure 4.12. Mean sea level pressure anomaly (hPa) during the first JFM of nuclear war simulations with (a) 150 Tg, (b) 46.8 Tg, (c) 37 Tg, (d) 27.3 Tg, (e) 16 Tg, (f-h) three ensembles with 5 Tg of soot.

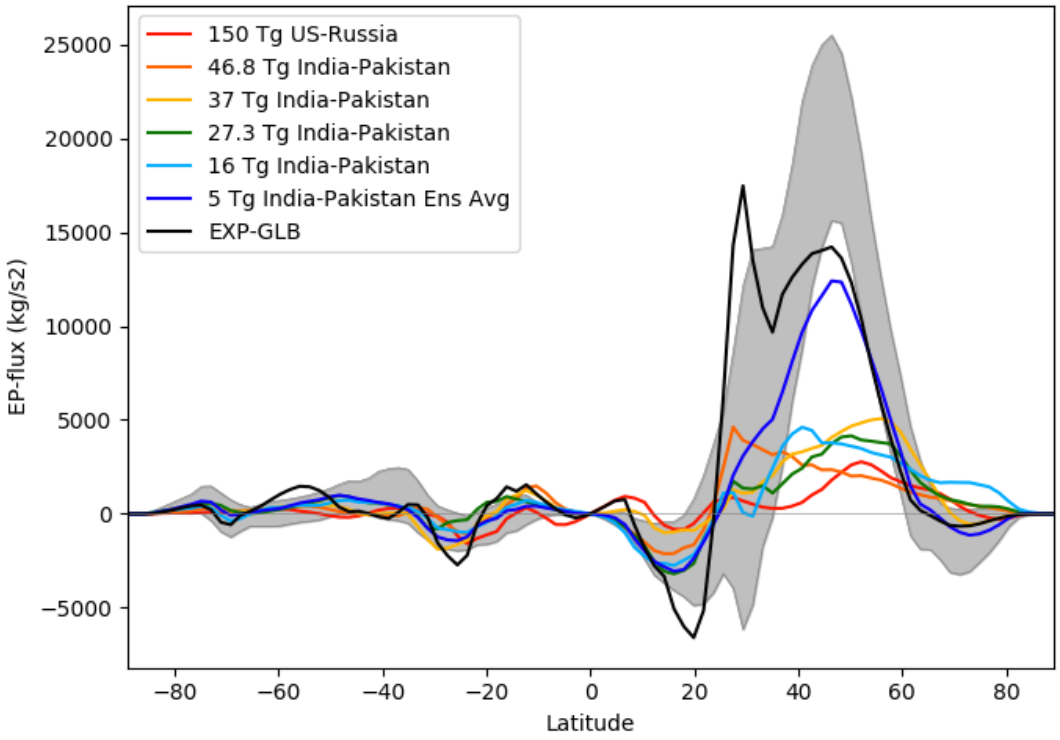

Figure 4.13. Vertical component of the zonally averaged Eliassen-Palm (E-P) flux at 400 hPa for DJF of years 0-1 for all six nuclear war simulations, including the EXP-GLB sensitivity test. The shaded area is ± 2 standard deviations from the control mean E-P flux climatology, so all of these represent a reduction of E-P flux when aerosols are introduced.

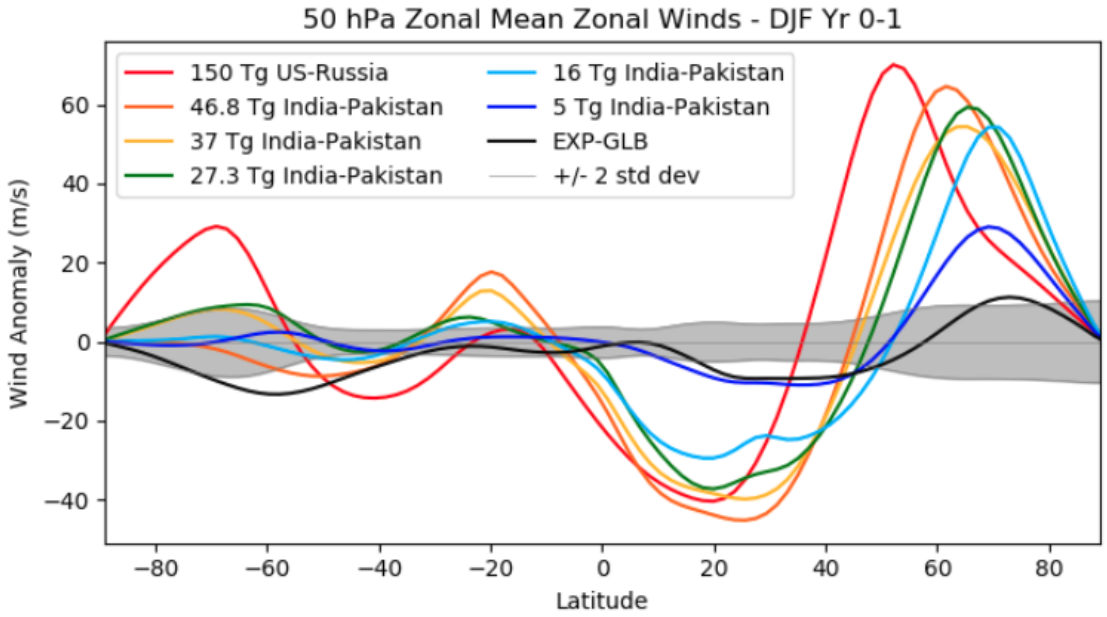

Figure 4.14. First DJF after the injection of soot, 50 hPa zonal mean zonal winds as a function of latitude for all six nuclear war simulations, including the EXP-GLB sensitivity test. Grey shading represents ± 2 standard deviations from the control mean climatology.

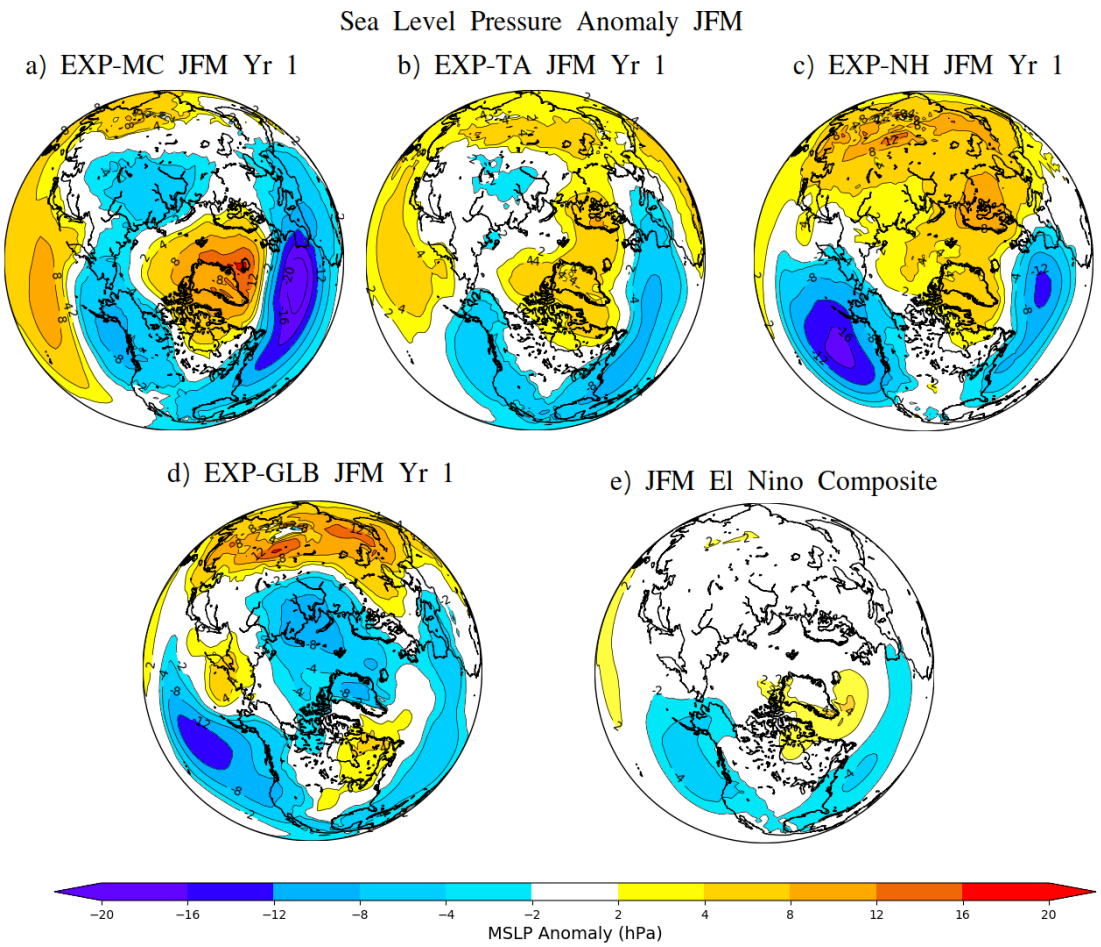

Figure 4.15. Mean sea level pressure anomaly (hPa) during the first JFM after the albedo perturbation for (a) EXP-MC, (b) EXP-TA, (c) EXP-NH, (d) EXP-GLB. (e) Mean sea level pressure composite of all JFM months with El Niño conditions in the control run climatology.